

**Characterization of signaling events following single-cell death in
myocardial cell clusters *in vitro***

Doctoral Thesis

Submitted in partial fulfillment of the requirements for the degree of

Doctor rerum naturalium (Dr. rer. nat.)

to the

Mathematisch-Naturwissenschaftlichen Fakultät

of the

Rheinischen Friedrich-Wilhelms-Universität Bonn

by

Krishna Chander Sridhar

from

Chennai, India

Bonn, January 2021

Angefertigt mit Genehmigung der Mathematisch-Naturwissenschaftlichen Fakultät der
Rheinischen Friedrich-Wilhelms-Universität Bonn

1. Gutachter: Prof. Rudolf Merkel
2. Gutachter: Prof. Ulrich Kubitscheck

Tag der Promotion: 07.05.2021

Erscheinungsjahr: 2021

Dedicated to my family

Summary

Cell death is a characteristic feature of acute and chronic cardiac pathologies such as myocardial infarction, ischemia-reperfusion and heart failure. Cardiomyocytes (CMs) death triggers myocardial remodeling that may lead to myocardial dysfunction over time. Although pathways of CM death in myocardial tissue have been described previously, spontaneous signaling events following CM death and the response of connected cells to these signals are not clearly understood. Elucidating cell death signaling mechanisms in myocardial tissue is essential to develop strategies to mitigate/alleviate myocardial damage. In this work, spontaneous signaling events were characterized in cultured rat embryonic myocardial cells upon single-cell death triggered by laser ablation. The dynamic changes in cells were studied based on spatial and temporal changes in Ca^{2+} concentrations ($[\text{Ca}^{2+}]$) using the Fluo-4 AM Ca^{2+} indicator. Laser-induced death of single CMs resulted in an increased $[\text{Ca}^{2+}]_i$ in CMs and fibroblasts (Fbs) surrounding the ablated cell in coculture clusters. $[\text{Ca}^{2+}]_i$ -increase followed completely different patterns in CMs and Fbs. Whereas in CMs the increase was slow and sustained, it was a single, fast and transient $[\text{Ca}^{2+}]_i$ spike in Fbs. Moreover, the increased $[\text{Ca}^{2+}]_i$ resulted in a briefly interrupted contractility in CMs that recovered with time. The cell-type (CM/Fb) specific effect was confirmed by analyzing ablation-induced cell death in separate cultures of CMs and Fbs obtained from a fusion-based magnetic cell separation method.

The $[\text{Ca}^{2+}]_i$ -increase in CMs following ablation was found to be distance-dependent as CMs that were closely connected to the ablated cell was highly affected by Ca^{2+} inflow compared to the farther located CMs ($>100 \mu\text{m}$), whose contractility remained largely unaffected. Comparing the radial Ca^{2+} propagation speeds along CMs and Fbs showed significantly faster propagation speeds ($\sim 20 \mu\text{m/s}$) in Fbs compared to those in CMs ($5 - 10 \mu\text{m/s}$). Further, $[\text{Ca}^{2+}]_i$ -increase as well as $[\text{Ca}^{2+}]_i$ recovery times post ablation in CMs and Fbs were significantly different and hence argued for a different Ca^{2+} propagation and handling in these cell types. High-resolution analysis of Ca^{2+} propagation in CMs showed a sequential diffusion of Ca^{2+} from ablated cell to connected cells along the cell-cell contacts. Moreover, immunocytochemical analysis showed the presence of gap junction protein connexin43 (Cx43), localized at junctions of adjacent CMs. This suggested a gap junction-mediated flow of Ca^{2+} between CMs upon ablation. However, in Fbs, lack of direct Ca^{2+} flow along the connected cells, absence of gap junction proteins (Cx40, Cx43, and Cx45), faster and almost constant propagation speeds indicated a putative membrane potential-driven propagation of Ca^{2+} upon ablation. Simultaneous analysis of Ca^{2+} and traction force changes in CM clusters

on soft substrates (15 kPa) confirmed the direct link between $[Ca^{2+}]_i$ -increase and disrupted contractility of surrounding CMs following ablation. Analysis of the effects of ablation on patterned growth of CMs and Fbs showed that single CM death in a cluster of CMs resulted in briefly delayed contractile beats in CMs cluster at the other end of a $\sim 500 \mu\text{m}$ wide fibroblast-bridge. Taken together, this research work illustrates the spontaneous Ca^{2+} signaling events following laser-induced single-cell death and the response of both CMs and Fbs to these signals. The study also describes the Ca^{2+} -based functional connectivity between CMs and Fbs in myocardial cell clusters.

Table of contents

Chapter 1	Introduction.....	1
1.1	The heart muscle architecture.....	2
1.1.1	Cellular composition of the heart	4
1.1.2	The myocardial extracellular matrix.....	8
1.2	Functional connectivity in myocardial tissue	10
1.2.1	Cell-cell connections between myocardial cells.....	10
1.2.2	Regulation of cardiac action potential	14
1.2.3	Calcium (Ca ²⁺) signaling in myocardial function.....	15
1.3	Cell death in myocardial tissues	18
1.3.1	Pathways of myocardial cell death – apoptosis, necrosis and autophagy-associated cell death.....	19
1.3.2	Impact of cell death in myocardial tissues.....	20
1.4	Motivation and Aim of the research	23
Chapter 2	Materials and Methods	25
2.1	Materials	25
2.1.1	Consumables.....	25
2.1.2	Chemicals	26
2.1.3	Solutions, Media and Buffers	27
2.1.4	Dyes and antibodies.....	29
2.1.5	Hardwares	30
2.1.6	Softwares	31
2.2	Primary cell culture from embryonic rat hearts	32
2.2.1	Isolation and culture of cardiac cells from rat embryonic hearts	32
2.2.2	Preparation of biotin-conjugated fusogenic liposomes	33
2.2.3	Fusion-based magnetic separation of myocardial cells	34
2.3	Live cell calcium imaging in cultured myocardial cells.....	36
2.4	Targeted killing of single cells by laser ablation	37
2.4.1	Principle of laser ablation	37
2.4.2	Laser ablation experimental setup.....	42
2.5	Preparation of patterned cultures of cardiomyocytes and non-myocytes using cell culture-inserts	43
2.6	Western blot.....	44

2.7	Immunocytochemistry.....	46
2.8	Traction force microscopy	47
2.8.1	Principle of traction force microscopy	47
2.8.2	Preparation of traction force substrates	49
2.8.3	Cell culture	49
2.9	Image processing	50
2.9.1	Determination of fraction of cardiomyocytes and non-myocytes	50
2.9.2	Analysis of intracellular Ca ²⁺ changes in cells	52
2.9.3	Analysis of cell force changes	57
2.10	Statistical analysis.....	60
Chapter 3 Results		61
3.1	Defined primary cell culture systems from embryonic rat hearts	61
3.2	Ca ²⁺ -based analysis of cell activity in cultured myocardial cells	64
3.2.1	Ca ²⁺ waves in myocardial cells	64
3.2.2	Characterization of spontaneous Ca ²⁺ waves in myocardial cells	65
3.3	Effect of ablation of single-cells in cocultures of cardiomyocytes and fibroblasts.....	67
3.3.1	Analysis of ablation-induced Ca ²⁺ propagation speed in cardiomyocytes and fibroblasts	71
3.4	Characterization of cell-type-specific effect of ablation using separate cultures of cardiomyocytes and fibroblasts.....	73
3.4.1	Effects of single-cell death in the cardiomyocytes-enriched culture system	73
3.4.2	Effects of single-cell death in the cardiomyocytes-depleted culture system	74
3.4.3	Comparison of Ca ²⁺ propagation speeds along cardiomyocytes and fibroblasts across different cultures	76
3.5	Recovery of contractility in cardiomyocytes affected by increased [Ca ²⁺] _i	79
3.6	Ca ²⁺ -based connectivity between cardiomyocytes and fibroblasts	80
3.6.1	Patterned growth of cardiomyocytes and fibroblasts	80
3.6.2	Fibroblasts mediated Ca ²⁺ changes in myocyte-clusters separated by long distances	81
3.7	Analysis of the long-term impact of ablation on affected cardiomyocytes.....	84

3.7.1	Long-term analysis of ablation-induced Ca ²⁺ changes	84
3.7.2	Ablation-induced high [Ca ²⁺] _i triggered strong contractility in cardiomyocytes	85
3.7.3	Analysis of contractile forces in cardiomyocytes before and after ablation.....	86
3.8	Mechanisms underlying ablation-induced Ca ²⁺ propagation in myocardial cells	91
3.8.1	Diffusion of Ca ²⁺ between cardiomyocytes upon ablation.....	91
3.8.2	Analysis of gap junction proteins in cardiomyocytes and fibroblasts	92
Chapter 4	Discussion	97
4.1	Mechanisms underlying [Ca ²⁺] _i regulation in CMs	97
4.2	Cell culture systems enabled characterization of cell-specific responses to ablation	101
4.3	Gap junctions mediated Ca ²⁺ propagation in CMs but not in Fbs	103
4.4	Ca ²⁺ propagation and handling in fibroblasts	105
4.5	Functional significance of Ca ²⁺ signals in cardiomyocytes and fibroblasts.....	107
Chapter 5	Conclusion and Outlook.....	111
	Supplementary results	113
	Abbreviations.....	116
	Bibliography.....	121
	Acknowledgements	135
	Publications	136

Chapter 1 Introduction

The heart is the central organ of the circulatory system, whose activity is essential for the circulation of oxygenated blood throughout the body. Blood circulation or perfusion is essential to supply nutrients, including oxygen, for the functioning of various organs of the body. Blood circulation throughout the body is achieved by the heart muscle activity (cardiac pump) that ensures the perfusion of various organs through the blood vessels (Weinhaus & Roberts, 2005). Due to its essential role in blood circulation, failure of the cardiac pump activity can result in nutrient starvation and subsequent dysfunction of organs (Arrigo, Parissis, Akiyama, & Mebazaa, 2016). Failure of the cardiac pump could result from various cardiovascular diseases (CVDs). CVDs are diseases of the heart and blood vessels and are the most common causes of mortality in the world, with about one-third of all deaths globally. Myocardial infarction (MI) and stroke constitute 85% of the deaths due to CVDs (World health organization, 2016). Chronic and acute heart pathologies can result in deterioration of heart function and subsequent cardiac pump failure. For example, in MI, the sudden death of heart muscle tissues can either result in immediate/acute failure of the heart or triggers a heart-remodeling process that could lead to other cardiomyopathies and/or progression to heart failure (HF) over time (N. G. Frangogiannis, 2014; Thygesen et al., 2019).

The synchronous muscle activity of the heart is governed by the electrical and mechanical interconnectivity of cardiac muscle cells (cardiomyocytes) in myocardial tissues. Myocardial injury, as in MI, results in large-scale death of cardiomyocytes, which leads to structural and functional changes in myocardial tissues. The fate of myocardial tissues following an injury is dependent on the adaptation/maladaptation of the surviving tissue and the underlying signaling mechanisms (O'Neal, Griffin, Kent, & Virag, 2013). Moreover, in addition to cardiomyocytes, the presence of other cell types such as fibroblasts in myocardial tissues, makes the events following myocardial injury more complicated (Pellman, Zhang, & Sheikh, 2016). Therefore, understanding the nature of interactions between the cells in myocardial tissues following injury and underlying signaling mechanisms is essential to understand myocardial pathologies in detail. The currently available knowledge and understanding of the heart muscle physiology, cellular composition, intracellular and intercellular signaling and pathophysiology of myocardial cell death are described in the upcoming sections.

1.1 The heart muscle architecture

The heart is one of the earliest functioning mammalian embryonic organs. In mammals, the heart development or cardiogenesis begins by embryonic day 9 in rats and from the third-week post fertilization in humans. Within the next several days, the cardiomyocytes (CMs) proliferate, thereby expanding the myocardial layer and generating the multi-chambered system of the mature heart. A primitive heart tube is formed at the earliest stages, and a complete, mature heart is formed around embryonic day 16 in rats and the seventh-week post fertilization in humans (Marcela et al., 2012). The mature heart consists of four chambers namely, the left atrium, right atrium, left ventricle and right ventricle, whose periodic contractions are the basis of the heart function. The periodic contraction (systole) and relaxation (diastole) of the heart muscle constitutes the cardiac cycle.

The cardiac cycle begins when oxygen-poor blood from various parts of the body enters the right atrium of the heart through superior and inferior vena cava. Due to the atrial contraction, the blood is drained into the right ventricle, which then contracts to pump blood to the lungs through pulmonary arteries. The tricuspid valve prevents the backflow of blood into the right atrium, while the pulmonary valve prevents the backflow of blood into the right ventricle from the pulmonary artery. Upon oxygenation in the lungs, the blood is returned to the heart through pulmonary veins. Oxygenated blood from the lungs enters the left atrium, and due to atrial contraction, it is drained into the left ventricle. Contraction of the left ventricle results in blood flow to other parts of the body through the aorta. The backflow of blood to the left atrium is prevented by the mitral valve, while backflow from the aorta is prevented by the aortic valve. The atria and ventricles are separated by the atrial septum and ventricle septum respectively (Weinhaus & Roberts, 2005). An illustration of the four chambers of the heart is shown in Fig. 1.1 a.

The wall of the heart can be divided into three layers – the endocardium, myocardium and the pericardium, as shown in Fig. 1.1 b. The endocardium is the innermost layer of the heart and can be further divided into layers of endothelial, smooth muscle and connective tissue cells (Berridge, Van Vleet, & Herman, 2013). It lines the blood vessels and plays a critical role in the formation of valves and septa of the heart (I. S. Harris & Black, 2010). The myocardium is the muscle layer of the heart responsible for the contractile function of the heart that is essential for perfusion throughout the body. The myocardium is made up of layers of CMs, which are electrically and mechanically connected to achieve coordinated muscle contraction (Miller & Gal, 2017; Sarantitis, Papanastasopoulos, Manousi, Baikoussis, & Apostolakis, 2012). The

pericardium is the outermost layer and can be further divided into the serous and fibrous pericardium. The fibrous pericardium consists of dense connective tissue whereas the serous pericardium consists of a pericardial cavity filled with lubricating serous fluid, which protects the heart from mechanical damage and infection (Shah, Gnanasegaran, Sundberg-Cohon, & Buscombe, 2009).

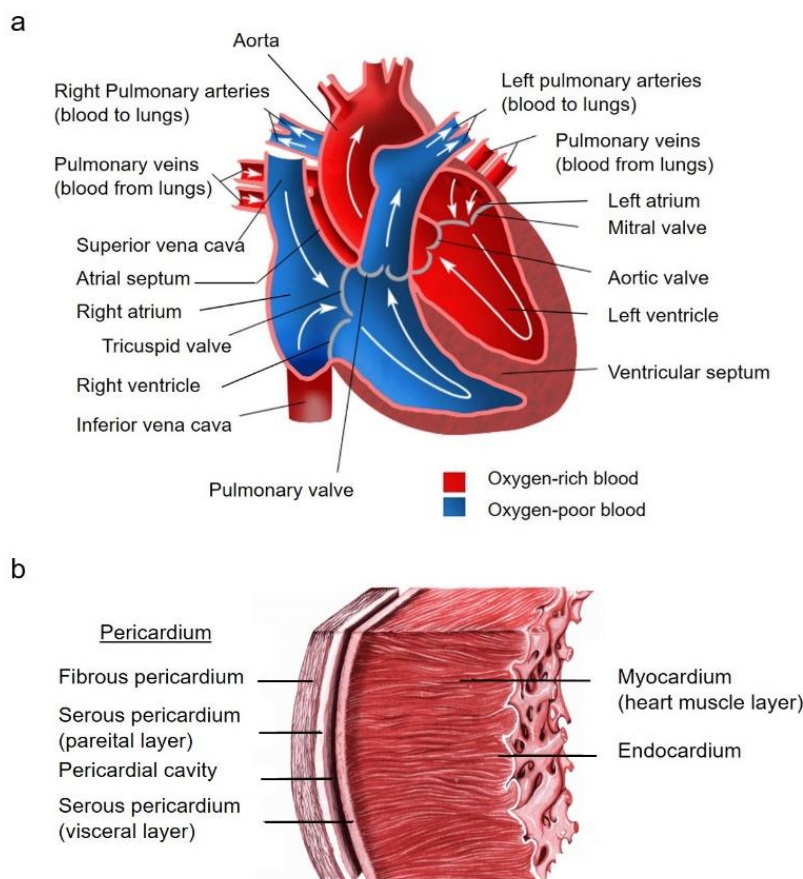


Figure 1.1: The architecture of the heart: **a)** An illustration of the cross-section of a normal physiological heart showing the four chambers and blood vessels. The oxygen-poor blood enters the right atrium and upon atrial contraction, it is drained into the right ventricle. Contraction of the right ventricle pumps blood to the lungs through the pulmonary arteries. Oxygen-rich blood from the lungs enters the left atrium through pulmonary veins and upon contraction of the atrium flows into the left ventricle. The blood is pumped to the various organs upon contraction through the aorta. Arrows indicate the direction of blood flow. **b)** Cross-sectional view of the heart wall showing the different layers – endocardium, myocardium and pericardium. The endocardium forms the innermost layer of the heart and lines the middle myocardial layer. The myocardium or the heart muscle comprises muscle cells or cardiomyocytes which confer the contractile function to the heart. The pericardium is the outermost layer and can be further divided into the serous and fibrous pericardium. (Modified from Fabio da Silva, 2018).

The coordinated activity of the heart muscle cells is governed by two essential features: the sarcomeres, which are the basic contractile units in CMs (Fig. 1.2 a) and the intercalated discs (ICDs), which contain cell adhesions between adjacent CMs (Fig. 1.2 b). The ICDs facilitate the continuity of the myofibrils/muscle fibers that confer mechanical connectivity and allow depolarizing currents called action potentials (APs) to spread quickly throughout the entire heart muscle via the passage of charged ions through intercellular junctions, thereby establishing electrical connectivity (Sheikh, Ross, & Chen, 2009). The physiological microenvironment of myocardial tissue includes its constituent cells - CMs, non-myocytes such as interstitial connective tissue cells (fibroblasts (Fbs)), the cells of the vasculature (smooth muscle cells (SMCs), endothelial cells (ECs)), resident immune cells and the extracellular matrix (ECM) in which these cells reside (Litviňuková et al., 2020; Zhou & Pu, 2016). In addition to a heavy workload pertaining to the continuous muscle activity, the myocardial microenvironment undergoes dynamic changes/adaptations to stress with age and pathological stimuli that shape the complexity of its structure and function over time (Nakou et al., 2016; van Dijk, Hamdani, Stienen, & van der Velden, 2008).

1.1.1 Cellular composition of the heart

a. Cardiomyocytes

CMs are typically rod-shaped cells with lengths in the range of 60 – 140 μm and radii of about 17 - 25 μm (human adult ventricular myocytes) (Tracy & Sander, 2011). CMs contain single nucleus at early developmental stage, however, they may be multinucleated at later stages of development when cell cycle arrests (F. Li, Wang, Capasso, & Gerdes, 1996). CMs contain numerous mitochondria that comprise 30% of cell volume and cater to the cellular energy demand of these cells (Piquereau et al., 2013). CMs proliferate at the early stages of development. However, it had been reported that in post-natal hearts, CMs undergo 1–2 rounds of cell division, become binucleated, and switch to predominantly hypertrophic growth. Moreover, the contractile protein isoforms switch from fetal to adult, metabolism switches from glycolytic to oxidative, cell cycle activators are repressed, cell cycle inhibitors are upregulated, and CMs lose their ability to regenerate. Therefore, well-developed mammalian hearts have limited regenerative potential (Foglia & Poss, 2016; Soonpaa, Kim, Pajak, Franklin, & Field, 1996). Recent evidence showed that the mammalian heart could renew, although with a low yearly CMs turnover rate of 1%, which may be insufficient to regenerate the heart in the event of a large-scale loss of CMs as in MI (Bergmann, 2019; Bergmann et al., 2009; Lázár, Sadek, & Bergmann, 2017)

The fraction of CMs and non-myocytes in the heart varies with species, developmental stage and pathological state of the heart. Moreover, in mice hearts, the non-myocytes constitute a larger fraction of the cell population than the CMs (Zhou & Pu, 2016). However, in normal physiological hearts, CMs occupy about 70-80% of the heart volume due to their large size compared to the non-myocytes. The synchronous contraction of CMs is driven by rhythmic AP propagation regulated by the influx and efflux of ions such as Na^+ , Cl^- , K^+ and Ca^{2+} (described in detail in next sections). Of these, Ca^{2+} is of prime importance in CMs as they form the basis of the excitation-contraction coupling (E-C coupling) mechanism, which governs the heart muscle contraction (Eisner, Caldwell, Kistamas, & Trafford, 2017). A typical myocardial tissue in a healthy mammalian heart is shown (Fig. 1.2 a) along with the intercellular connections at the intercalated disc between the CMs (Fig. 1.2 b).

Besides the working atrial and ventricular CMs specialized CMs are found in sinoatrial node (SAN), known as pacemaker cells or conduction cells, which are capable of spontaneously firing the rhythmic APs (M. Baruscotti, Barbuti, & Bucchi, 2010; Mirko Baruscotti, Bucchi, & DiFrancesco, 2005). The main difference between the pacemaker cells and the rest of the working CMs is the automaticity in AP generation. Pacemaker cells can generate APs that set the rate of contraction for the heart. At resting state (during a diastolic interval), the atrial and ventricular CMs have a stable membrane potential of about -80 mV, whereas, in pacemaker cells, the membrane potential rises slowly from -60 mV to the threshold for igniting a new AP. This phase of membrane potential is sustained by regulating the ionic currents and pumps at variable times and voltages (M. Baruscotti et al., 2010). The pacemaker cells are connected to the CMs via gap junctions (GJs), which allow spontaneous depolarization of the cells and subsequent contraction of the cardiac muscle.

Apart from the pacemaker cells of the SAN, the CMs of the atrioventricular node (AVN) can act as a secondary pacemaker when the SAN fails. However, owing to its higher rate of depolarization compared to other secondary pacemaker regions, the SAN controls the rate of contraction under normal physiological conditions. The AP from the SAN travels along the conduction system of the heart at the pace set by the primary pacemaker cells and assigns the contractile function to the cardiac muscle (M. Baruscotti et al., 2010).

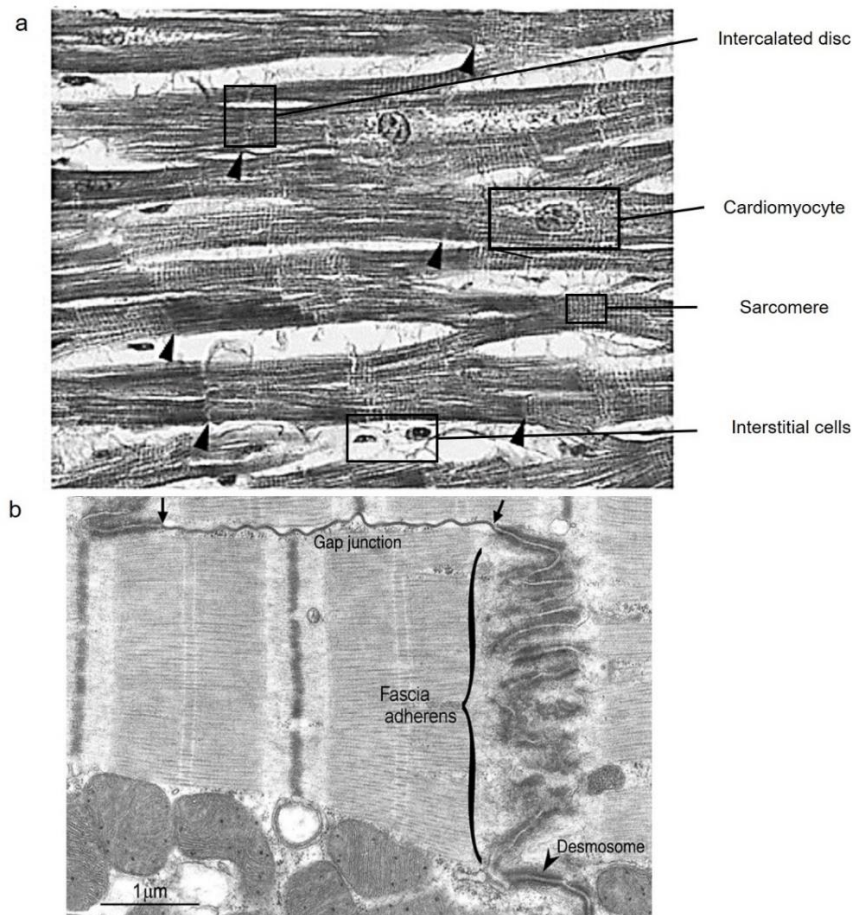


Figure 1.2: Physiological myocardial tissue: a) Magnified image of human left ventricular myocardial tissue stained with Gomori trichrome showing the arrangement of cardiomyocytes in tissues. Cardiomyocytes contain sarcomeres, the repetition of which forms myofibrils/muscle fibers. Cardiomyocytes are connected through intercalated discs (indicated by arrows). Interstitial cells such as fibroblasts (white) are present in the cardiac tissue along with cardiomyocytes. Modified from (Buetow & Laflamme, 2018). Scale not known. **b)** Transmission electron micrograph of the cardiac intercalated disc showing three major junctions – fascia adherens (adherens junction), desmosomal junctions and gap junctions between adjacent cardiomyocytes. Adapted with permission from Severs, N.J. *BioEssays* 2000 (Nicholas J. Severs, 2000).

b. Non-myocytes

The resident non-myocyte population in the heart primarily consists of Fbs, ECs, SMCs, leukocytes/macrophages. The fraction of non-myocytes in the heart may vary with species, age and pathological states (Banerjee, Fuseler, Price, Borg, & Baudino, 2007; Pinto et al., 2016). In addition to the resident non-myocytes, during MI, necrotic death of CMs following ischemia triggers an inflammatory cascade that leads to Fbs infiltration into affected myocardial tissue and differentiation to myofibroblasts (Ma et al., 2014; Weber, Sun, Bhattacharya, Ahokas, & Gerling, 2013). Studies on cardiac cell composition showed a variation in the fraction of each

cell type across different mammalian species, especially rats, mice and humans. In rats, it had been reported, Fbs (64%) were the most predominant non-myocytes compared to ECs (6%), while CMs formed only 30% of cells of the heart (Banerjee et al., 2007). In humans, Fbs formed 43% of the population, while ECs and CMs formed only 24% and 33%, respectively (Bergmann et al., 2015). A study of the non-myocyte population in mouse hearts revealed that ECs were more predominant cells forming 64% of total cells, while Fbs formed only 27% of cells (Pinto et al., 2016).

In physiological myocardial tissues, Fbs provide structural support and interact directly or indirectly with the CMs. During the development of the heart, the Fbs develop from mesenchymal stem cells or multipotent progenitor cells. Fbs lack a basement membrane, are arranged in sheets and strands, and appear as elongated cells, which lie along the CMs within the endomyial collagen network. These cells have been shown to form a network interconnected by long filopodia (Souders, Bowers, & Baudino, 2009). Fbs play an active role in the synthesis and maintenance of ECM, signaling to CMs through mechanical stress and providing response elements for the immune system activated during myocardial injury (Baum & Duffy, 2011). Fbs respond to mechanical and chemical stimuli and interact with CMs directly as well as through paracrine factors (Kakkar & Lee, 2010).

Moreover, electromechanical crosstalk between CMs and Fbs has been previously observed (Rother et al., 2015). The number of Fbs, unlike CMs, continues to expand, and the cells grow and differentiate with increasing heart size (Baum & Duffy, 2011). Following MI, keloid translocation of Fbs into the myocardial tissue can lead to cardiac fibrosis and arrhythmias (Vasquez, Benamer, & Morley, 2011). Thereby, Fbs composition is critical in the pathological progression of the heart (W. Chen & Frangogiannis, 2013; Rother et al., 2015). Further, the interactions between CMs and Fbs is studied extensively in the context of the pathophysiology of the heart.

In mammalian hearts, the ECs represent a significant fraction of the non-myocyte population. Especially in mice hearts, ECs form the largest fraction of non-myocytes (Pinto et al., 2016). Paracrine signaling and physical cell-cell contacts (*in vitro*) between CMs and ECs have been reported. Further, the interactions between CMs and ECs have been investigated in recent years, specifically in the context of cardiac remodeling and regeneration. However, the existence of functional connectivity between these cells in the native heart still is not well understood (Talman & Kivelä, 2018). Besides the cell types mentioned above, in mice hearts, leukocytes constituted about 7-10% of the non-myocyte fraction and were mostly found to be macrophages (Pinto et al., 2016). These cells are essential for phagocytosis and have an

important role in inflammation of myocardial tissue in the event of MI or ischemia/reperfusion (I/R) injury (Bönner, Borg, Burghoff, & Schrader, 2012). The various cell types found in mammalian hearts are shown in Fig. 1.3.

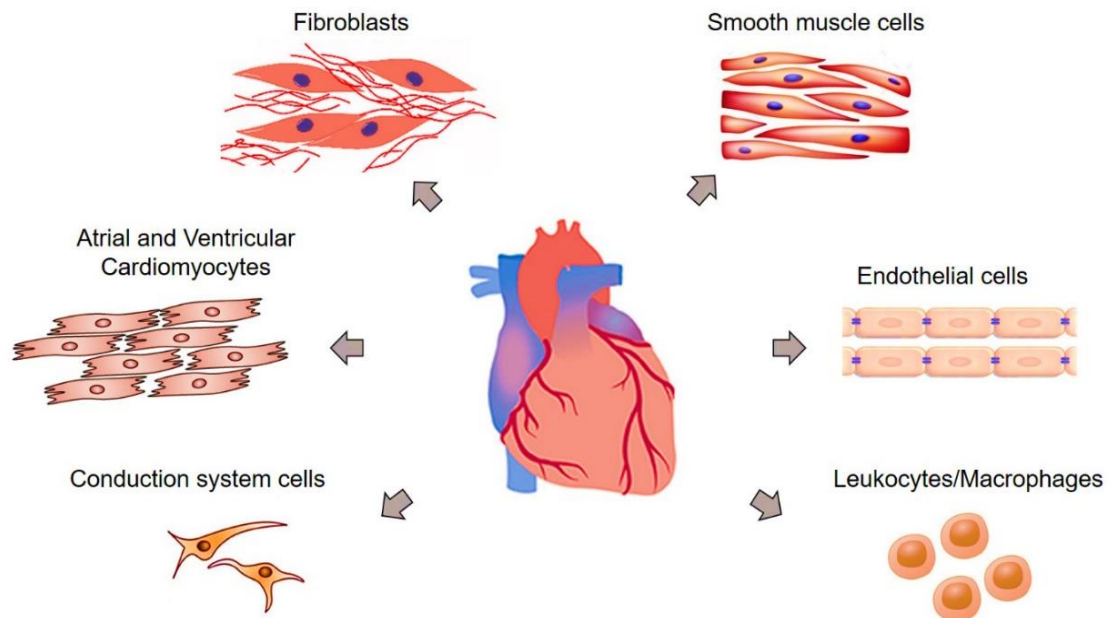


Figure 1.3: Resident cells of the mammalian heart: The cell population of the heart can be broadly classified as cardiomyocytes and non-myocytes. The cardiomyocyte population includes the working atrial and ventricular myocytes, the cells of the cardiac conduction system - the cells of the sinoatrial node, atrioventricular node and Purkinje fibers. The non-myocyte population is composed of fibroblasts, vascular endothelial cells, smooth muscle cells and resident leukocytes. Cardiomyocytes are the primary functional cells of healthy myocardial tissue. Fibroblasts form a significant proportion of the non-myocyte cell population and are essential for the regulation of myocardial tissue ECM and interact with cardiomyocytes via direct cell-cell connections or indirectly via paracrine signals.

1.1.2 The myocardial extracellular matrix

The myocardial ECM is a meshwork of fibers comprised of matrix proteins in which CMs, interstitial cells, leukocytes and cardiac vascular cells reside (Rienks, Papageorgiou, Frangogiannis, & Heymans, 2014). The ECM includes the basement membrane (BM) and the interstitial matrix. Around each CM, the BM forms a dense network of about 80 nm thickness and provides structural support to the CMs (Yang, Borg, Wang, Ma, & Gao, 2014). The interstitial matrix encompasses interstitial cells like Fbs. The ECM facilitates the adhesion of CMs in myocardial tissues. The ECM network provides alignment cues, biochemical signals and mechanical support to the resident cells (Ariyasinghe, Lyra-Leite, & McCain, 2018).

The myocardial ECM proteins can be broadly classified into three categories: structural proteins such as collagen and elastin; cell adhesive or antiadhesive molecules such as fibronectin, vitronectin, laminin, and tenascin; and proteoglycans, which are a complex array of proteins linked to glycosaminoglycan side chains. The major components of the matrix include collagen, fibronectin and elastin proteins. Collagen is the most predominant matrix protein, and five types of collagen are commonly found – collagen type I, III, IV, V and VI. Among these types, collagen types I and III represent more than 90% of collagen proteins in the myocardium. Precise myocardial ECM composition of fibrillar collagens, basement membrane components and proteoglycans is essential for proper cardiac geometry and function (Ju & Dixon, 1995).

CMs are anchored to the ECM mechanically through costameric adhesions. Costameres are protein assemblies that couple sarcomeres to the sarcolemma. Whereas sarcomeres are the force-generating units, costameres function as the primary force-transmitting units in CMs. (Hersch et al., 2013). In addition to facilitating cell attachment to the substrate, the costameres enable the CMs to sense and respond to the external environment, thereby playing an important role in mechanotransduction (Samarel, 2005). The major protein complexes of costameres include the dystrophin-associated glycoprotein complex (DAG complex) and integrin-vinculin-talin complex (Sarantitis et al., 2012). The various proteins involved in cardiomyocyte-ECM interactions are shown in Fig. 1.4.

Besides supporting myocardial cells through structural proteins, the ECM also accommodates multiple proteins with growth-factors and cell-receptor-binding properties (Rienks et al., 2014). Further, the ECM helps distribute mechanical forces throughout the myocardium and convey mechanical signals to individual cells via cell surface ECM receptors (Souders et al., 2009). The ECM composition determines the stiffness of myocardial tissue. The ratio of collagen type I and III are critical in determining myocardial stiffness (Weis Sara et al., 2000). Stiffening of tissue can be an indication of underlying tissue pathology.

During MI, the inflammatory cascade triggers Fbs infiltration and differentiation to myofibroblasts, which secrete ECM proteins, especially collagen. An enhanced collagen secretion and subsequent formation of collagen-based scar tissue results in increased tissue stiffness. While elasticities of healthy myocardial tissues range from 10 to 30 kPa, stiffness in heart stroke affected areas increases to values of up to 150 kPa (Berry et al., 2006; Gupta, Ratcliffe, Fallert, Edmunds, & Bogen, 1994; Jacot, McCulloch, & Omens, 2008). This increased stiffness leads to mechanical stress that requires morphological and functional adaptations from CMs (Hersch et al., 2013). Moreover, increased stiffness has been known to

cause Fb proliferation and differentiation to myofibroblasts, leading to a fibrotic myocardial tissue (Herum, Choppe, Kumar, Engler, & McCulloch, 2017). While CMs interact with the ECM through sarcomeres, cardiac Fbs interact with the ECM through integrins and discoidin domain-containing receptor 2 (DDR2) (Souders et al., 2009).

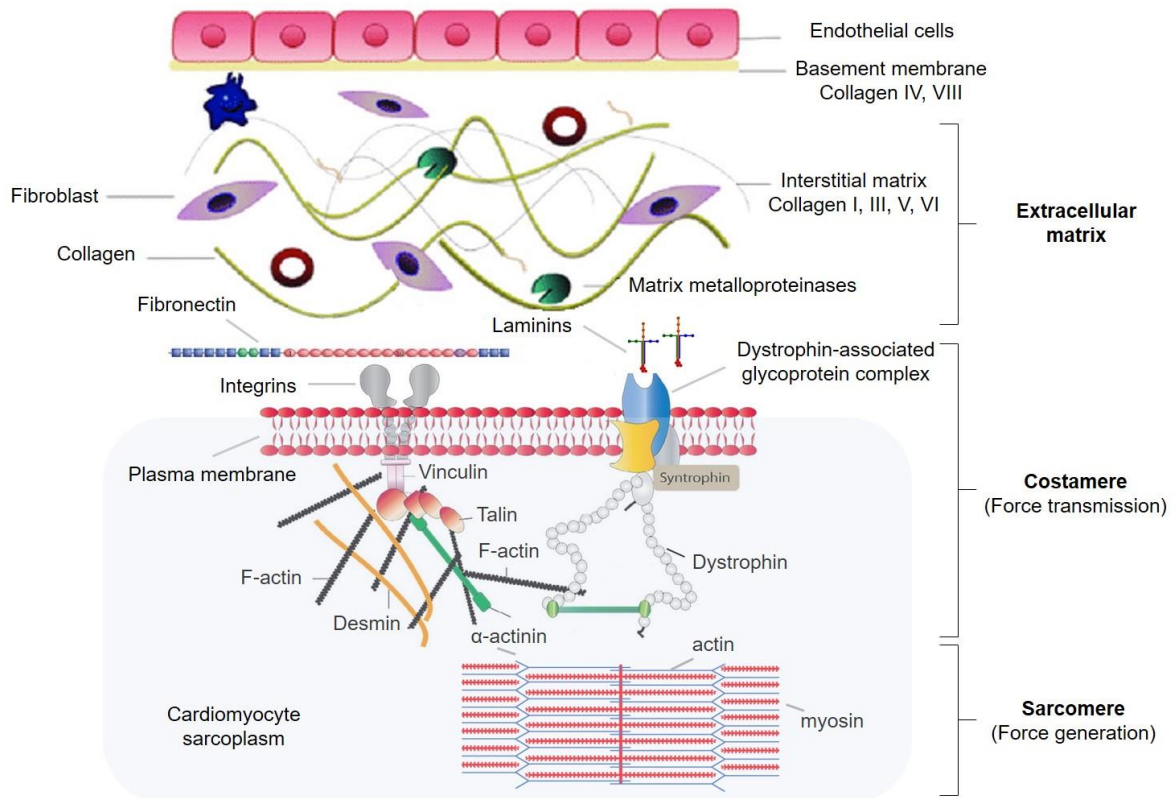


Figure 1.4: The myocardial extracellular matrix and cardiomyocyte adhesion: The extracellular matrix (ECM) in the myocardial tissue is a network of proteins to which cardiomyocytes are adhered. Collagen is the most predominant protein found in the matrix. Interstitial collagens are synthesized and secreted mainly by interstitial fibroblasts and are degraded by matrix metalloproteinases to balance ECM composition in myocardial tissue. Cardiomyocytes are anchored to the ECM through the costamere complex, consisting of the vinculin-talin-integrin complex and the dystrophin-associated glycoprotein complex. While sarcomeres are the force-generating units in cardiomyocytes, costamere and its constituent proteins are essential for cell adhesion to ECM, anchorage and force transmission/distribution. Modified from (Ali, Braga, & Giacca, 2020; S. H. Nielsen et al., 2018).

1.2 Functional connectivity in myocardial tissue

1.2.1 Cell-cell connections between myocardial cells

Cell-cell connection in CMs is facilitated by junctions at the ICD and is essential to maintain structural integrity and synchronized contraction of the myocardial tissue. The ICD comprises three major junctional complexes: desmosomes which function as cell anchor, *fascia adherens*

or adherens junctions (AJs) which provides strength to cells and GJs which couple the cells electrically and metabolically (Fig. 1.5 a). Desmosomes anchor cell membranes to the intermediate filament (IF) network, particularly in tissues undergoing constant physical stress, such as skin and heart. By mediating cell-cell adhesion and cytoskeletal linkages, desmosomes mechanically integrate cells within tissues and function to resist mechanical stress (Kowalczyk & Green, 2013). Desmosomal proteins include: (a) tissue-specific desmosomal cadherins, e.g., desmogleins (DSG) and desmocollins (DSC) - transmembrane proteins that form Ca^{2+} -dependent heterophilic cell-cell adhesive interactions, (b) armadillo proteins, e.g., plakoglobin (PKG) (γ -catenin) and plakophilins (PKP) - cytoplasmic cadherin binding partners that signal and regulate cadherin adhesive activity, and (c) plakins (desmoplakins) that link to intermediate filaments, e.g., desmin (DES) (Sheikh et al., 2009). Defects in proteins involved in cell-cell connections have a detrimental effect on the fate of the myocardium and are associated with heart failure (Sequeira, Nijenkamp, Regan, & van der Velden, 2014).

The *fascia adherens* or adherens junctions in cardiac cells connect actin filaments from adjacent cells and provides anchorage to cells by linking the cell membrane to the actin cytoskeleton. These junctions allow the cell to retain shape upon mechanical stress. Further, it transduces signals concerning the actin cytoskeleton, and it senses mechanical forces on the cell (Vermij, Abriel, & van Veen, 2017). Proteins in these junctions include (a) cadherins, e.g., N-cadherin - transmembrane proteins responsible for Ca^{2+} -dependent homophilic cell-cell adhesion, (b) catenins, e.g., α -, β -, and γ -catenin (plakoglobin - cytoplasmic proteins that bind to cadherins and regulate their adhesive activity, and (c) other catenin-related proteins including vinculin and α -actinin, which link the ICD to the cytoskeleton (Sheikh et al., 2009).

The AJs and desmosomes are collectively called ‘adhesion junctions’ or ‘adhering junctions’ because cadherins make up the intercellular contact proteins of both junctions, and AJs and desmosomes both connect cells to the cytoskeleton of adjacent cells, although through different cytoskeletal proteins. Plakoglobin (PKG) is considered the most important factor in the adhesion junction since it is a structural element of both AJs and desmosomes (Vermij et al., 2017). Knockout studies have revealed devastating consequences to heart development and fetal viability in the absence of AJs and desmosomes, suggesting their importance to normal cardiac development and function (Gutstein, Liu, Meyers, Choo, & Fishman, 2003).

In addition to the mechanical linkages, GJs form dynamic inter-cellular aqueous pores or channels made up of connexin proteins (Kumar & Gilula, 1996; N. J. Severs, Bruce, Dupont,

& Rothery, 2008). GJs are made up of two hemichannels or connexons from adjacent CMs which dock with one another. These channels enable electrical and metabolic coupling between two adjoining cells by enabling small molecules (<1 kDa) to diffuse from the cytoplasm of one cell to another (Sheikh et al., 2009). Structural analyses have shown that each connexon is composed of 6 polypeptidic trans-membrane protein subunits, termed connexins. Thereby, six connexin (Cx) molecules interact with one another to form two hemichannels (connexons) across an intercellular space, as shown in Fig. 1.5 b.

Connexins are encoded by a large family of genes that comprises at least 20 isoforms in humans. All represent structurally conserved non-glycosylated trans-membrane proteins 25 to 62 kDa in size that differ chiefly in the length of their C-terminal domain (Segretain & Falk, 2004). Connexons are synthesized in the endoplasmic reticulum (ER) and occur as oligomers in the Golgi apparatus. Under normal conditions, connexon hemichannels are carried, in a closed configuration, by small vesicles to the plasma membrane from the Golgi with associated interactions with microtubules. Once inserted into the plasma membrane, hemichannels diffuse laterally and dock with counterparts contributed by a neighboring cell to form functional gap junction units that interact to generate plaques. Among the various connexin isoforms, Cx40, Cx43 and Cx45 are prominently found in the mammalian heart (Desplantez, 2017).

In myocardial tissues, CM-Fb and Fb-Fb connections appear to be formed from connexins and cadherins (Souders et al., 2009). There are two types of cadherins expressed in adherens junctions in the heart: OB-cadherin and N-cadherin. OB-cadherin is the dominant cadherin in myofibroblasts associated with wound healing. N-cadherin is found in mechanical junctions between adjoining cardiomyocytes and between adjoining myofibroblasts. Currently, the information on cadherin-based signaling in cardiac myofibroblasts and cardiac myocytes is very limited, except for adhesion or development-based signaling study (Thompson et al., 2014). Cardiac Fbs express several connexin isoforms, with distinct expression patterns in different cardiac regions, disease conditions, and stage of development. The presence of connexins has been detected in cell cultures as well as intact tissues. Several studies have shown that cardiac Fbs establish functional GJ channels with adjacent Fbs and neighboring CMs, both *in vitro* and *in situ* (Johnson & Camelliti, 2018).

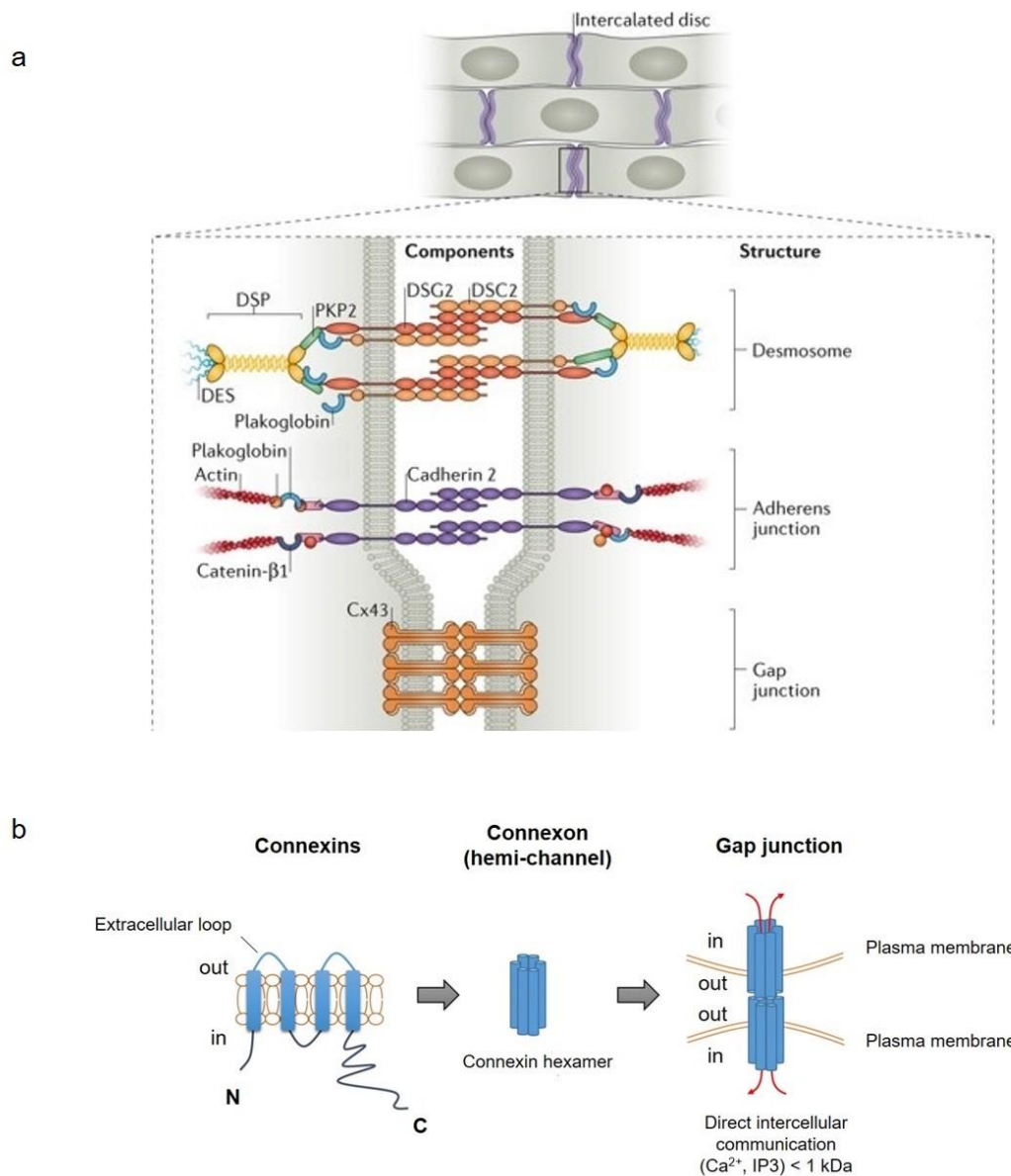


Figure 1.5: Intercellular connections between cardiomyocytes: **a)** Schematic illustration of the various intercellular junctions between cardiomyocytes at the intercalated discs. The three major junctions include - desmosomes that anchor intermediate filaments. The desmosomes consist of extracellular units desmoglein (DSG) and desmocollin (DSC) connected to the intermediate filaments through the cytoplasmic components - plakophilin (PKP), desmoplakin (DSP) and plakoglobin. The adherens junction anchors the actin filaments of adjacent cells through cadherins, catenins and plakoglobin, while the gap junctions are involved in direct cell-cell communication by facilitating the bidirectional flow of molecules between cardiomyocytes and are made of connexin proteins. Modified from (Schlipp et al., 2014) **b)** Gap junctions are made of two hemichannels called connexons, formed from 6 connexin subunits, and dock with the hemichannel of adjacent cardiomyocytes. The resulting connection allows a flow of molecules such as Ca^{2+} between cardiomyocytes to result in rapid action potential propagation in myocardial tissues. Modified from (J.-I. Wu & Wang, 2019).

Besides direct cell-cell contacts, Fbs have been shown to conduct electrical impulses between CMs *in vitro* (Gaudesius, Miragoli, Thomas, & Rohr, 2003). A study by Quinn et al. showed evidence of functional coupling between non-myocytes and CMs in the heart by using

optogenetic tools. By monitoring the electrical activity in mouse hearts, they found that non-myocytes displayed CM-like action potentials at the border zone of cryo-injured hearts, indicating the presence of electrotonic coupling between non-myocytes and CMs in native myocardium (Quinn et al., 2016). Moreover, it was reported that Fbs show cardiac contraction-related fluctuations in membrane potential, probably mediated by stretch-activated ion channels and changes in Ca^{2+} handling (Kohl & Gourdie, 2014).

1.2.2 Regulation of cardiac action potential

The AP currents resulting from the influx and efflux of ions cause changes to the resting membrane potential. The GJs play a crucial role in the spread of APs by facilitating ions between adjacent cells. The flow of ions between cells through this low resistance coupling is the basis of functional connectivity between the CMs (Rohr, 2004). The ion channels involved in the regulation of AP are classified based on two features: selectivity and gating (voltage/ligand-gated) of ions (M. Baruscotti et al., 2010). The AP current in CMs can be classified into four distinct phases – phase 0, 1, 2 and 3, while phase 4 corresponds to the beginning of the next cycle of depolarization and repolarization. The initiation of AP in CMs is regulated by voltage-gated Na^+ channels, which rapidly depolarize the cells. During phase 0, membrane permeability to K^+ decreases and fast Na^+ channels open, producing rapid membrane depolarization from -90 mV to $+10$ mV. The membrane potential at which half of the cardiac Na^+ channels are available for activation is -80 mV (Zimmer, Haufe, & Blechschmidt, 2014).

At phase 1, the Na^+ channels are inactivated, and K^+ channels close, resulting in slightly negative potential. Phase 2 is the plateau phase of the AP. Membrane permeability to Ca^{2+} increases during this phase, maintaining depolarization and prolonging the AP. Membrane permeability to Ca^{2+} decreases to some extent towards the end of phase 2, and the plateau is partially maintained by an inward Na^+ current. Na^+ flows into the cell through the $\text{Na}^+/\text{Ca}^{2+}$ exchanger. The exchanger transfers three Na^+ ions into the cell in exchange for one Ca^{2+} ion flowing out, producing a net inward positive current. As Ca^{2+} channels inactivate towards the end of the plateau phase, an inward K^+ current produces repolarization in phase 3. The membrane potential in phase 4 returns to approximately -90 mV - the initial resting membrane potential state, mediated by the selective permeability of the cell membrane to K^+ and the concentration gradient for K^+ that exists across the cell membrane (M. Baruscotti et al., 2010).

1.2.3 Calcium (Ca^{2+}) signaling in myocardial function

Calcium (Ca^{2+}) is involved in the regulation of a diverse range of functions in CMs that includes regulation of AP and cell-cell communication, E-C coupling and muscle contraction, energy consumption and production, cell death by apoptosis or necrosis,) transcriptional regulation through, e.g., calmodulin (CaM)-dependent activation of calcineurin and the nuclear translocation of factors such as histone deacetylases (Bers, 2008). Most important among these is the regulation of AP current and CM contraction through E-C coupling (described later). Owing to their involvement in a diverse array of functions through intercellular and intracellular signaling, Ca^{2+} is highly regulated in CMs by complex Ca^{2+} regulatory mechanisms. Ca^{2+} signaling is governed by both local and global cytosolic Ca^{2+} concentration ($[\text{Ca}^{2+}]$) –changes by these mechanisms (Fearnley, Roderick, & Bootman, 2011).

The key players in the regulation of Ca^{2+} in CMs are the voltage-gated L-type calcium channels (LTCCs) that are essential for Ca^{2+} current (I_{Ca}) during AP, the ryanodine receptors (RyRs) in SR, the sarcoplasmic/endoplasmic Ca^{2+} ATPase (SERCA) and sodium-calcium exchanger (NCX) (Fearnley et al., 2011). In addition to these key players of Ca^{2+} fluxes, networks of signaling mechanisms and accessory proteins (in the cytosol and sarcoplasmic reticulum (SR)) such as calsequestrin, calmodulin (CaM), CaMKII (Ca^{2+} /calmodulin-dependent kinase II), calpain and troponin C (TnC) confer complex regulation of cardiac Ca^{2+} signals (Dewenter, Lieth, Katus, & Backs, 2017).

The LTCCs are widely distributed in the plasma membrane of CMs, especially in high concentrations in the T-tubules (transverse tubules), which are invaginations of the plasma membrane. Following depolarization of membrane during AP current, LTCCs open, resulting in a local $[\text{Ca}^{2+}]$ rise or “ Ca^{2+} sparklet” within 1 ms in the junctional cleft (space between sarcoplasmic reticulum and plasma membrane) from 0.1 to $> 10 \mu\text{M/L}$. The rise in $[\text{Ca}^{2+}]$ in the cleft activates the ryanodine receptors (RyRs) to release Ca^{2+} from the SR. About 25 LTCCs and ~ 100 RyRs are closely associated within the dyadic cleft to form a “couplon” (Bers & Guo, 2005). A single RyR opening can release Ca^{2+} from SR; however, roughly 6 – 20 channels at each couplon open to ensure effective E-C coupling. This intracellular release of Ca^{2+} from stores is called calcium-induced calcium release (CICR) and typically raises the cytosolic $[\text{Ca}^{2+}]$ to $> 100 \mu\text{M/L}$ (Dewenter et al., 2017), resulting in “ Ca^{2+} spark”.

Diffusion of Ca^{2+} ions and their subsequent spatial and temporal summation produces an average global $[\text{Ca}^{2+}]$ increase of 0.5 to $\sim 1 \mu\text{M/L}$. Ca^{2+} diffuses across the cytosol to activate

sarcomere contraction (Fearnley et al., 2011). Myofilaments in CM sarcomeres comprises thick and thin filaments. The thin filament is composed of actin, tropomyosin, and the hetero-trimer troponin (composed of the troponins Tn-T, Tn-C, and Tn-I), while the thick filament is composed of myosin. The thin filament protein troponin C in the sarcomeres acts as the functionally most important Ca^{2+} buffer. Ca^{2+} binding to Tn-C induces a conformational rearrangement in Tn-C, causing the Tn-C: Tn-I association to strengthen while at the same time weakening the Tn-I: Tn-T association; the movement of tropomyosin exposes a myosin-binding site on actin, allowing cross-bridge formation to take place. This results in force development and shortening of the sarcomere (de Tombe, 2003). The various $[\text{Ca}^{2+}]_i$ regulatory mechanisms in CMs are shown in Fig. 1.6.

Following myofilament contraction, Ca^{2+} release mechanisms are inactivated while Ca^{2+} efflux mechanisms are activated. Inactivation of RyRs depends on the cleft $[\text{Ca}^{2+}]$ and regulation by luminal SR $[\text{Ca}^{2+}]$. As Ca^{2+} release proceeds and SR $[\text{Ca}^{2+}]$ declines, the gating properties of RyRs strongly favor closure. Thereby, the SR is never fully depleted of Ca^{2+} physiologically and consequently, Ca^{2+} sparks and myofilament contraction is regulated (Sham et al., 1998). Ca^{2+} removal in CMs is regulated by the SERCA and sarcolemmal extrusion mainly through NCX and by a minor contribution of plasma membrane calcium ATPase (PMCA). In the steady-state, the amount of Ca^{2+} taken up by the SR during relaxation must equal the amount released. The amount that enters by Ca^{2+} current through voltage-gated Ca^{2+} channels must equal the amount extruded to maintain the Ca^{2+} homeostasis in CMs (Eisner et al., 2017). After the removal of cytosolic Ca^{2+} , Ca^{2+} unbinds from TnC, tropomyosin blocks the actin-binding sites, cross bridges detach, and the tension returns to zero. In the absence of Ca^{2+} , Tn-I exerts an inhibitory effect, preventing actin-myosin interaction. Thereby, the myofilaments return to their relaxed state (de Tombe, 2003). The different steps involved in myofilament contraction is illustrated in Fig. 1.7.

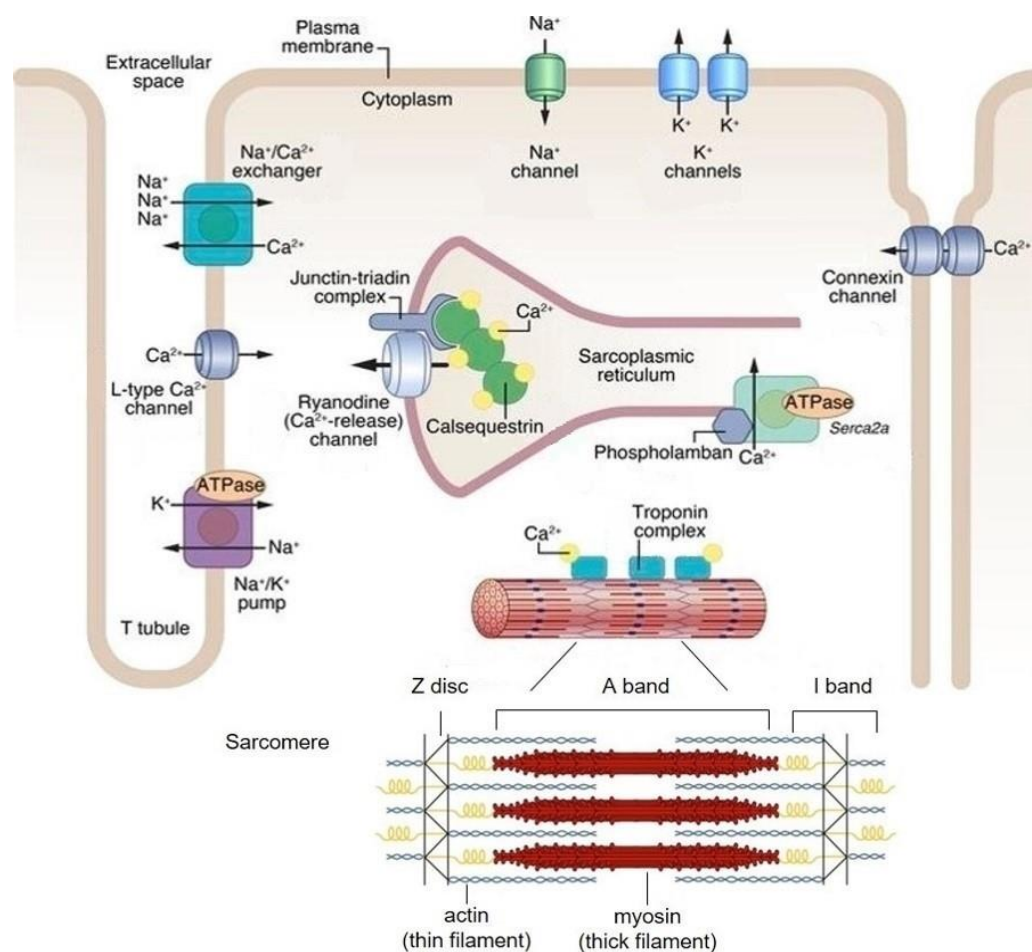


Figure 1.6: Ca²⁺ regulation in cardiomyocytes: Schematic illustration of Ca²⁺ regulation in cardiomyocytes by the different Ca²⁺ influx and efflux mechanisms. Ca²⁺ entry is facilitated by voltage-gated L-type Ca²⁺ channels upon depolarization during the action potential. Local increase of Ca²⁺ at the cleft between sarcoplasmic reticulum and sarcolemma triggers the release of Ca²⁺ from SR through ryanodine receptor channels resulting in a Ca²⁺ spark. Ca²⁺ diffuses to the myofilaments where it binds to troponin C at the troponin complex of the sarcomere. Ca²⁺ binding causes cross-bridge formation by which actin (thin filament) slides along the myosin (thick filament) to cause sarcomere shortening. Coordinated contraction of the sarcomere in connected cardiomyocytes causes cardiac muscle contraction. Cytosolic Ca²⁺ removal results in Ca²⁺ unbinding from troponin C and subsequent muscle relaxation. Ca²⁺ is recycled into SR and extracellular space through sarcoplasmic Ca²⁺ ATPase (SERCA) and plasma membrane Na⁺-Ca²⁺ exchanger respectively. A bidirectional Ca²⁺ transport can occur through the connexin gap junctional channel to enable a rapid spread of action potential across the connected cardiomyocytes. Calsequestrin and phospholamban are essential proteins in Ca²⁺ regulation in SR. The former is a Ca²⁺ binding protein that binds SR Ca²⁺ while the latter regulates SERCA gating in SR. Modified from (Baskin et al., 2017).

Any perturbations in the above described Ca²⁺ mechanisms can lead to the disruption of [Ca²⁺] homeostasis that can have strong effects on CMs ranging from transcriptional regulation to cell death. Dysregulation of Ca²⁺ regulatory mechanisms or altered expression of related proteins

were associated with cardiomyopathies such as arrhythmia, hypertrophy and heart failure (Lebeche & Kang, 2013). Further, it has been previously reported that diseased CMs show alterations in Ca^{2+} -handling and Ca^{2+} -dependent transcriptional patterns (Dewenter et al., 2017).

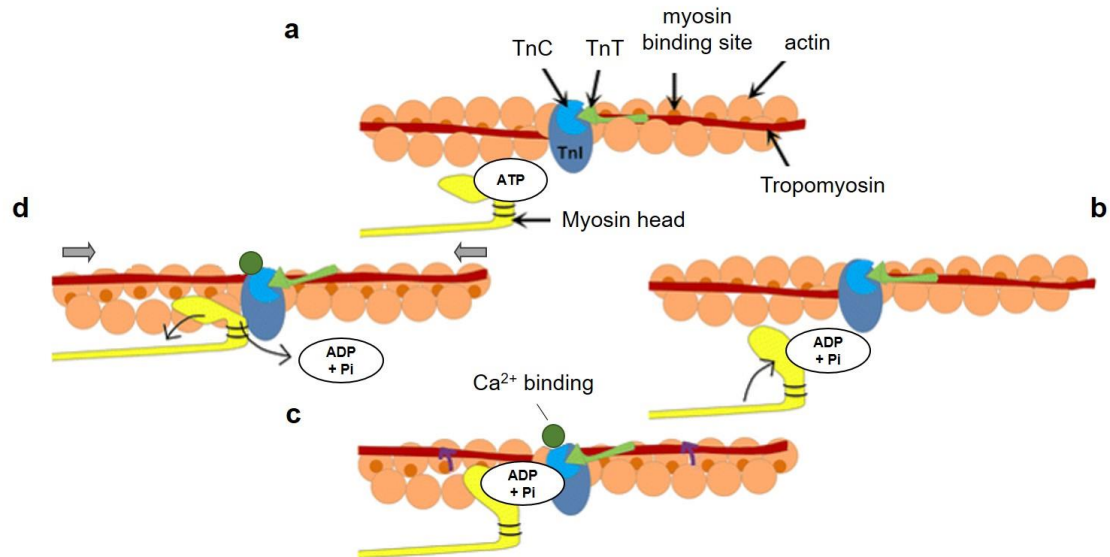


Figure 1.7: Mechanism of myofilament contraction and relaxation: The cardiomyocyte sarcomere comprises thin and thick filaments. **(a)** The thin filament is composed of actin, tropomyosin, and the hetero-trimer troponin (composed of the troponins Tn-T, Tn-C and Tn-I). The thick filament is composed of myosin. ATP binds to the ATP binding domain in the myosin head. **(b)** ATP hydrolysis to ADP and phosphate allows the myosin filaments to move towards the actin filament. **(c)** Ca^{2+} binding to Tn-C induces a conformational rearrangement in Tn-C, causing the Tn-C:Tn-I association to strengthen while at the same time weakening the Tn-I:Tn-T association. The movement of tropomyosin (indicated by arrows) exposes a myosin-binding site on actin, allowing cross-bridge formation to take place. **(d)** Release of the hydrolyzed nucleotides results in the extension of the myosin head, permitting the sliding of the filaments (arrows). ATP quickly rebinds to the ATP-binding site on the myosin head, allowing dissociation of the myosin away from the actin filament, and a new cycle begins. Modified from (England & Loughna, 2013)

1.3 Cell death in myocardial tissues

The heart has a limited regenerative capacity as only a small fraction of CMs turn over during an entire lifetime. Bergmann and colleagues reported CMs renewal in the human heart using Carbon-14 integration into DNA. However, the renewal gradually decreased from 1% annual turnover at the age of 25 to 0.45% at the age of 75 (Bergmann et al., 2009). While the possibility of CMs renewal in the adult mammalian heart has been established, the extent of renewal, homeostatic conditions and source of new CMs are still being investigated (Bergmann, 2019; Bergmann & Jovinge, 2014; Lázár et al., 2017). Large scale loss of CMs occurs during MI,

which is often beyond the capacity of CMs renewal, could lead to a deterioration of myocardial function (N. G. Frangogiannis, 2012). Loss of CMs can also occur gradually with aging. Aging has been associated with loss of CMs, cellular and molecular level changes and myocardial dysfunction (Sheydina, Riordon, & Boheler, 2011). Cell death, either progressive or acute, is a characteristic feature of decreased heart function that could eventually lead to HF. All three types of cell death - apoptosis, necrosis and autophagy-associated cell death - have been observed during the progression of heart diseases. The choice of pathway depends on the stimuli or upstream signaling mechanisms (Chiong et al., 2011).

1.3.1 Pathways of myocardial cell death – apoptosis, necrosis and autophagy-associated cell death

Cells die primarily by apoptosis or necrosis. Apoptosis is characterized by cell shrinkage, fragmentation into membrane-enclosed apoptotic bodies and phagocytosis of these bodies by macrophages or sometimes by neighboring cells. An efficient clearance process in apoptosis results in a targeted deletion of cells from the tissues and avoids inflammation. However, necrosis is characterized by loss of plasma membrane integrity, cellular and organelle swelling and triggering of inflammation (Konstantinidis, Whelan, & Kitsis, 2012). Unlike apoptosis, the ATP levels and energy expenditure are not well regulated in necrosis. Thereby, necrosis involves ATP reduction and mitochondrial damage and is followed by inflammatory cascades (Elmore, 2007). Although apoptosis and necrosis are known to be exclusive mechanisms of cell death, evidence suggests that they are mediated by distinct but highly overlapping central pathways, namely the ‘Extrinsic pathway’ that involves cell surface death receptors and the ‘Intrinsic pathway’ that primarily depends on the mitochondria and endoplasmic reticulum (ER)-mediated signaling cascades (Whelan, Kaplinskiy, & Kitsis, 2010).

The primary event in apoptosis (intrinsic) is permeabilization of the outer membrane of mitochondria (OMM), resulting in the release of apoptogens. In contrast, the defining event in primary necrosis (intrinsic) is the early opening of a channel in the inner mitochondrial membrane (IMM) termed the mitochondrial permeability transition pore (mPTP) (Konstantinidis et al., 2012). Necrotic cell death also occurs following Ca^{2+} overload, hypoxia and oxidative damage, and the mPTP acts as a mediator of this event (Shaheen, Cheema, Shahbaz, Bhattacharya, & Weber, 2011). Previous studies indicated that in aging hearts, apoptotic cell death occurs through the intrinsic pathway (Kwak, 2013). Although both apoptosis and necrosis have been described in pathologies such as ischemia and reperfusion

injury, the necrotic pathway can trigger inflammatory cascades that result in myocardial remodeling (Nikolaos G. Frangogiannis, 2015; Garcia-Dorado & Ruiz-Meana, 2000).

In the heart, autophagy is essential for the turnover of organelles at low basal levels under normal conditions and is upregulated in response to stresses such as ischemia (Chiong et al., 2011). While autophagy may lead to cell death through apoptosis or necrosis, an autophagy-specific mode of killing is not completely understood. The upstream signaling mechanism may determine the function of autophagy to result in cell survival or death (K. Nishida, Kyoi, Yamaguchi, Sadoshima, & Otsu, 2009).

1.3.2 Impact of cell death in myocardial tissues

Necrotic death of CMs is a common feature of MI and HF, which involves rupture of plasma membrane resulting in the release of intracellular contents that initiate an inflammatory reaction in the underlying tissues. Necrotic cells and damaged ECM in the affected myocardial tissue release endogenous alarm signals called Damage associated Molecular Patterns (DAMPs) (Roh & Sohn, 2018). The DAMPs act as “danger signals” and activate innate immune mechanisms, initiating an intense but transient inflammatory response. Toll-Like Receptor (TLR)-mediated pathways, the complement cascade and reactive oxygen generation, results in chemokine and cytokine synthesis. Further, the release of pro-inflammatory mediators induces the recruitment of neutrophils and pro-inflammatory monocytes into the infarcted myocardium (Nikolaos G. Frangogiannis, 2015).

As inflammation progresses, activated leukocytes in myocardial tissues clear the wound by phagocytosing dead cells and matrix debris. As the infarct is cleared of dead cells and matrix fragments, the inflammatory response is suppressed. Neutrophils become apoptotic and are phagocytosed by macrophages; reparative monocytes are recruited, while lymphocytes and macrophages produce inhibitory mediators capable of suppressing pro-inflammatory signals, such as Interleukin (IL)-10 and Transforming Growth Factor (TGF)- β . The suppression of the inflammatory reaction is followed by infiltration of the infarct with Fbs and ECs marking the transition to the proliferative phase. Transdifferentiation of Fbs into myofibroblasts is a prominent characteristic of the proliferative phase. The myofibroblasts in the infarct tissue express α -smooth muscle actin (α -SMA), synthesize and deposit matrix proteins such as collagen and are believed to be important for infarct contraction and structural integrity of the infarcted heart. As the infarct is filled with matrix, cellular proliferation is suppressed, and

transition to the maturation phase follows. As the infarct matures, matrix cross-linking results in the formation of a dense collagen-based scar (W. Chen & Frangogiannis, 2013). An example of post-infarct myocardial tissue is shown in Fig. 1.8, which shows the different regions of the myocardial tissue affected by MI. The infarct zone represents the region in which ischemic death of CMs occurs and the formation of collagen-based scar tissue as described above. The area surrounding this region is called the infarct border zone. In the infarct border zone of rat myocardium, both viable CMs, as well as interstitial cells, could be found while the viable myocardium contains the surviving CMs (Gross et al., 2016).

Between days 3-5 following MI, there is a transition from inflammation to repair, with activation of Fbs and progressive scar deposition. Over time a complex remodeling process is activated in the injured myocardial tissues. While the remodeling process may restore the function of the heart post injury, the remodeling often predisposes the heart to other pathological conditions such as fibrosis, atrial fibrillation, arrhythmias, hypertrophy and subsequent HF (Schirone et al., 2017). The progression to cardiomyopathies or HF following a myocardial injury is governed by the various overlapping pathways of cardiac remodeling. Here, further death of CMs is a crucial event in the development of myocardial dysfunction. The oxidative stress and alteration in energy metabolism trigger the hypertrophic and profibrotic signaling cascades, resulting in a progressive loss of CMs. Cardiac hypertrophy and fibrosis and a progressive impairment of contractility and relaxation orchestrate together the detrimental evolution of cardiac remodeling. (N. G. Frangogiannis, 2012).

Several adaptive/maladaptive cellular and molecular level changes have been known to be a part of the cardiac remodeling process after injury. For example, the surviving CMs undergo reorganization of cell-cell and cell-ECM interactions (Matsushita et al., 1999), respond to stress signals – including mechanical signals, paracrine signals and metabolic changes (Dostal et al., 2014). In an animal model of microinfarct, dedifferentiated and apoptotic CMs were found in the infarct border zone. Here, CMs dedifferentiation was not an early stage of a degenerative pathway and was considered as an adaptation enabling the survival of the CMs (Valen, 2003). Further, alterations of proteins involved in Ca^{2+} transport are also responsible for cardiac remodeling, contributing to decreasing systolic and increasing diastolic calcium release and reduced contractility (Lehnart, Maier, & Hasenfuss, 2009). Additionally, neurohormonal activation, such as the renin-angiotensin aldosterone system, enhances the synthesis of proteins involved in inflammation, cell death, and Fb proliferation. These adaptive/maladaptive changes

are a part of compensatory mechanisms in myocardial remodeling that could decide the fate of the surviving tissues following a myocardial injury (Schirone et al., 2017).

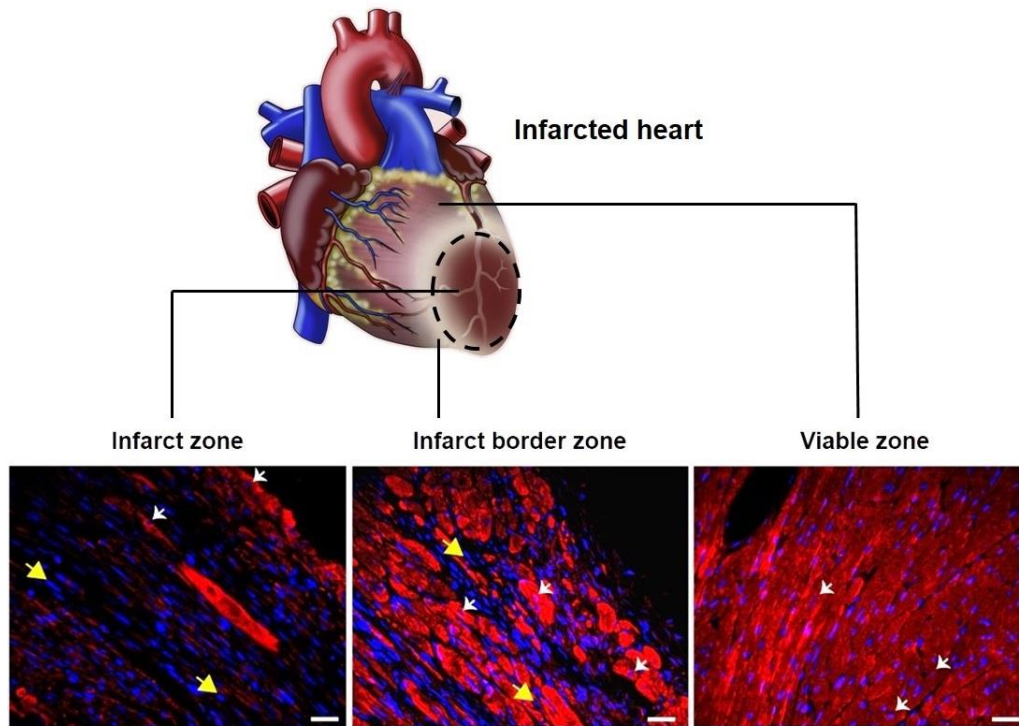


Figure 1.8: Myocardial tissue post infarction: Mouse left ventricle tissue post myocardial infarction, showing cells stained for sarcomere protein α -actinin (red) and nuclei (blue). Cardiomyocytes contained sarcomeres and were positive for α -actinin (indicated by white arrows), while non-myocytes lacked sarcomeres and were only positive for nuclear stain (yellow arrows). The infarct area represents the site of ischemic injury that is characterized by CMs loss and formation of a scar tissue. The infarct zone shows loss of CMs as seen from lack of sarcomeres. Nuclei of interstitial cells can be seen in the infarct zone, indicating the formation of scar tissue post infarction. The infarct border zone represents the transition from the injury site to surviving CMs. the viable zone represents the tissue that is distant from the ischemic injury and contains morphologically normal CMs. Modified from (Gross et al., 2016).

1.4 Motivation and Aim of the research

Cell death is a characteristic feature of acute and chronic heart pathologies such as myocardial infarction (MI) and heart failure (HF). Myocardial injury owing to MI results in large-scale loss of cardiomyocytes that could result in acute failure of the heart or could lead to a remodeling of the myocardium over time that could lead to the progression to cardiomyopathies and/or HF. The different pathways of cell death owing to injury and the process of myocardial remodeling have been well described so far. However, the impact of cell death on myocardial tissues following an injury and the spontaneous response of connected cells to the loss of cardiomyocytes are not well characterized but are essential to understand the extent of myocardial damage and associated signaling mechanisms in detail. This is particularly intriguing because, in myocardial tissues, cardiomyocytes are electrically and mechanically well connected to each other to effect muscle contraction. Thereby, loss of cardiomyocytes can have a direct effect on the functionality of the connected cardiomyocytes.

This research work was aimed at understanding the impact of cell death in myocardial tissues by analyzing the response of cells in myocardial cell clusters to a single cell-death. The technique of laser ablation was chosen to kill single cells as it provided an advantage of precise manipulation/disruption of cells *in vitro*. With a combination of confocal microscopy and laser ablation, the dynamic changes in cells following single-cell death could be observed at a high spatiotemporal resolution.

In addition to cardiomyocytes, the native myocardial tissues also consist of non-myocyte populations. Previously it had been reported that the non-myocytes, especially fibroblasts, interact electrotonically with cardiomyocytes and are known to electrically couple cardiomyocytes separated by long-distances. Based on these studies, it has been established that fibroblasts possess a functional significance in myocardial tissues. Therefore, characterization of the impact of cell death on surrounding myocardial cell clusters that include both cardiomyocytes and fibroblasts could provide valuable knowledge on the interaction and the nature of connectivity between cardiomyocytes and fibroblasts.

Ca^{2+} forms the basis of cardiomyocyte functionality (excitation-contraction coupling) and is involved in intracellular and intercellular signaling mechanisms. Therefore, cardiomyocytes' functionality and intercellular connectivity can be analyzed based on the dynamic changes in intracellular calcium concentration $[\text{Ca}^{2+}]_i$ in cells before and after single-cell death using a Ca^{2+} indicator. Moreover, as $[\text{Ca}^{2+}]_i$ -changes are more prominent in muscle cells compared to

non-muscle cells, the myocytes and non-myocytes in myocardial cell clusters can be distinguished based on $[Ca^{2+}]_i$.

The key research goals of this thesis work were:

- To analyze the effects of single cardiomyocyte death in myocardial cell clusters induced by laser ablation and the spontaneous response of connected cardiomyocytes in cluster based on the dynamic changes in intracellular Ca^{2+} concentrations ($[Ca^{2+}]_i$) reported by a fluorescent Ca^{2+} indicator.
- To characterize and compare the effects of single myocardial cell (cardiomyocyte or non-myocyte) death on surrounding cardiomyocytes and non-myocytes in the cluster.
- To identify the possible mechanisms underlying the functional connectivity between the myocardial cells in the event of single-cell death.

The analysis of events following cell death in myocardial cells can thus be useful to characterize the spontaneous response of connected cells, associated signals and the nature of intercellular connectivity between the cells.

Chapter 2 Materials and Methods

2.1 Materials

2.1.1 Consumables

Consumable	Manufacturer
Sterile surgical scalpels	Braun, Kronberg, Germany
Dumont forceps	Fine Science Tools, Heidelberg, Germany
Glass coverslips (1.5#, high-precision, 170 ± 5 µm thickness)	Paul Marienfeld, Lauda-Königshofen, Germany
Petri dishes with 18 mm hole	Cell E&G, San Diego, CA
Falcon® 70 µm cell strainer	Corning, Tewksbury, MA
Falcon® cell scraper	Corning
MiniMacs magnetic column	Miltenyi Biotec, Bergisch Gladbach, Germany
Culture-insert 3-well	IBIDI, Martinsried, Germany
Vacuum filter (VacuCap 60)	Pall Life Sciences, Port Washington, NY
Pipettes 5 ml, 10 ml, 50 ml	VWR, Radnor, PA
Pipette tips 10 µl, 200 µl, 1250 µl	Starlab, Hamburg
Petri dishes	Greiner Bio-One, Kremsmünster, Austria
Reaction tubes 0.2 ml, 1.5 ml, 2 ml	Eppendorf, Hamburg, Germany
Falcon® conical centrifuge tubes	Corning
Falcon® cell culture flasks 25 ml	Corning
Latex gloves (Gentle skin)	Meditrade, Kiefersfelden, Germany
Nitrile gloves (Kimtech pure G3)	Kimberly-Clark, Irving, TX
Immersion oil 518 F	Carl Zeiss, Jena, Germany
4–20% Mini-PROTEAN® TGX™ Precast Protein Gels, 15-well, 30 µl	Bio-Rad, Hercules, CA

2.1.2 Chemicals

Chemical	Manufacturer
Deoxyribonuclease (DNase II from bovine spleen)	Sigma-Aldrich, St. Louis, MO
1,2-dioleoyl-sn-glycero-3-phosphoethanolamine (DOPE)	Avanti Polar Lipids, Inc., Alabaster, AL
1,2-dioleoyl-3-trimethylammonium-propane (chloride salt, DOTAP)	Avanti Polar Lipids, Inc.,
1,2-dioleoyl-sn-glycero-3-phosphoethanolamine-N-(cap biotinyl) (sodium salt, biotin-DOPE)	Avanti Polar Lipids, Inc.,
1,10-dioctadecyl-3,3,30,30-tetramethylindotricarbocyanine iodide (DiR)	Life technologies, Eugene, OR
Sodium bicarbonate	Sigma-Aldrich
Sodium dodecyl sulfate	Sigma-Aldrich
Human fibronectin	Corning
(3-aminopropyl)triethoxysilane	Sigma-Aldrich
2-(4-morpholino)ethanesulfonic acid	Sigma-Aldrich
Glycine	Sigma-Aldrich
Sylgard 184 Silicone elastomer kit	Dow Inc., Midland, MI
Anti-biotin magnetic microbeads (130-090-485)	Miltenyi Biotech, Bergisch Gladbach, Germany
Dry milk powder	Carl Roth, Karlsruhe, Germany
Triton-X-100	Sigma-Aldrich
1-ethyl-3-(3-dimethylaminopropyl)carbodiimide	Sigma-Aldrich
N-hydroxysulfosuccinimide	BioVision, Milpitas, CA
Formaldehyde solution (37%)	Sigma-Aldrich
2-(4-(2-hydroxyethyl)-1-piperazinyl)ethanesulfonic acid (HEPES)	VWR, Radnor, PA
Sodium hydroxide	Merck, Darmstadt, Germany

Tris(hydroxymethyl)aminomethane (Tris Base)	Sigma-Aldrich
--	---------------

2.1.3 Solutions, Media and Buffers

a. Solutions		
Hank's balanced salt solution	H6648	Sigma-Aldrich
0.05% trypsin-EDTA solution (1x)	25300062	Gibco, Waltham, MA
Phosphate buffered saline (1x)	20012027	Gibco
5-Bromo-4-chloro-3-indolyl phosphate - nitro blue tetrazolium (BCIP-NBT) liquid substrate	B1911	Sigma-Aldrich
Tween-20	P9416	Sigma-Aldrich
FluoSpheres carboxylated (0.2 µm, crimson)	F8806	Invitrogen, Carlsbad, CA
RIPA buffer	R0278	Sigma-Aldrich
Protease inhibitor cocktail	P8340	Sigma-Aldrich
4x Laemmli sample buffer	1610747	Bio-Rad
Precision Plus Protein™ Kaleidoscope™ Prestained Protein Standards (10 – 250 kDa)	1610375	Bio-Rad
Amersham™ Protran™ 0.2 µm Nitrocellulose membrane	10600004	General Electric, Schenectady, NY

b. Buffers			
<i>Cytoskeletal buffer (CB)</i>			
Sodium chloride (NaCl)	150 mM	S7653	Sigma-Aldrich
Magnesium chloride (MgCl ₂)	5 mM	M2670	Sigma-Aldrich
ethylene glycol-bis(2-aminoethylether)- N,N,N',N'-tetraacetic acid (EGTA)	5 mM	E3889	Sigma-Aldrich
D-(+)-Glucose	5 mM	G7528	Sigma-Aldrich
2-(4-morpholino)ethanesulfonic acid (MES)	10 mM	M2933	Sigma-Aldrich

added to distilled water; pH adjusted to 6.1	
<i>Silane buffer</i>	
Ethanol	95 %
Distilled water (Milli-Q)	5 %
pH adjusted to 4.5 – 5.5 with acetic acid	
<i>Coupling buffer</i>	
2-(4-morpholino)ethanesulfonic acid,	50 mM in distilled water
pH adjusted to 6.0 with NaOH	
<i>Running buffer (10x)</i>	
Tris-base	30.3 g
Glycine	144 g
Sodium dodecyl sulfate	10 g
Dissolved in 1 L distilled water; pH adjusted to 8.3	
<i>Transfer buffer (10x)</i>	
Tris-base	30.3 g
NaCl	144 g
Ethanol	200 ml
Dissolved in 1 L distilled water; pH adjusted to 8.3;	
<i>Tris-buffered saline (TBS) (10x)</i>	
Tris-base	24 g
NaCl	88 g
Dissolved in 1 L distilled water; pH adjusted to 7.6	

c. Media			
Dulbecco's modified eagle medium	1x	11960-044	Gibco
<i>Culture medium</i>			
Nutrient mixture F-10 Ham	N6335	9.8 g/L	Sigma-Aldrich
Sodium bicarbonate	S6014	5 ml of 7.5% solution in 1 L medium	Sigma-Aldrich
added to distilled water; pH adjusted to 7.2, vacuum filtered and supplemented with:			
Fetal bovine serum	S0615	1/10	Sigma-Aldrich

PenStrep antibiotic solution	P4333	1/100	Sigma-Aldrich
ITS liquid media supplement (100x)	I3146	1/200	Sigma-Aldrich

2.1.4 Dyes and antibodies

a. Primary antibodies		
Dye/Antibody	Identifier	Manufacturer
Mouse sarcomeric anti- α -actinin, clone EA-53 monoclonal antibody	A7811	Sigma-Aldrich
Rabbit polyclonal anti-connexin43	AB1728	Merck
Rabbit polyclonal anti-connexin40	364900	Thermofisher, Waltham, MA
Rabbit polyclonal anti-connexin45	AB1745	Merck
Connexin43 monoclonal antibody	CX-1B1	Invitrogen
Anti-actin antibody, clone C4	MAB1501R	Merck
b. Secondary antibodies		
Cy3-conjugated goat anti-mouse	115-165-006	Jackson Immunoresearch, Baltimore Pike, PA
Alexa fluor 546 Goat anti-rabbit	A11010	Invitrogen
Cy3-goat anti-rabbit	111-166-046	Jackson Immunoresearch
Alexa fluor 488 Goat anti-mouse	A11001,	Invitrogen
Anti-mouse IgG alkaline phosphatase antibody from goat	A3562	Sigma-Aldrich
c. Dyes		
CytoPainter Phalloidin-iFluor488	AB176753	Abcam, Cambridge, UK
Phalloidin-iFluor633	AB176758	Abcam
NucBlue	R37605	Molecular Probes, Eugene, OR
Fluo-4 AM	F14217	Molecular Probes

2.1.5 Hardwares

Objective	Company
40x C-Apochromat Corr M-27 water immersion objective (NA 1.1)	Carl Zeiss
EC Plan-Neofluar 40x oil objective (NA 1.3)	Carl Zeiss
20x Plan-Apochromat objective (NA 0.8)	Carl Zeiss
Laser scanning microscope - LSM880	Carl Zeiss
Pulsed UV laser (diode pumped solid state laser)	RAPP optoelectronics GmbH, Wedel, Germany
UGA-Firefly point scanning device	RAPP optoelectronics
Spin-coater	Süss MicroTec Lithography GmbH, Garching, Germany
Milli-Q water purification system	Merck
MACS MultiStand	Miltenyi Biotec
Centrifuge (Sigma 3-16 K)	Sigma Laborzentrifugen GmbH, Osterode am Harz, Germany
Centrifuge (5415 R)	Eppendorf, Hamburg, Germany
Stereomicroscope	Carl Zeiss
Light source (KL1500 LCD)	Carl Zeiss
Hemocytometer	Hecht Glaswarenfabrik GmbH, Sondheim vor der Rhön, Germany
Vacuum desiccator	Duran, Wertheim, Germany
Gel Doc system	Bio-Rad

2.1.6 Softwares

Software	Version	Developer
ImageJ	v1.52n for Windows	National Institute of Health (NIH), Bethesda, MD
Matlab	R2017	MathWorks, Natick, MA
Python	v3.8.3 for Windows	Python Software Foundation, Wilmington, DE
ZEN	V2.3 SP1 FP3 (Black) 64 bit	Carl Zeiss
ROE-SysCon	v1.2.0.3 (build: 4.20.0.6)	Rapp Optoelectronics
GraphPad Prism	v8.4.3 for Windows	GraphPad Software, San Diego, CA

2.2 Primary cell culture from embryonic rat hearts

2.2.1 Isolation and culture of cardiac cells from rat embryonic hearts

Primary cardiac cell culture was obtained from embryonic rat (18 - 19 days post fertilization) hearts (Animal testing license: 81-02.04.2018.A90, LANUV NRW, Germany) as described in (Hersch et al., 2016). Pregnant rats were anesthetized with excess CO₂ and decapitated with a guillotine. The skin was disinfected with ethanol and cut open to remove embryos. Embryos were carefully transferred to cold Hank's balanced salt solution (HBSS) and decapitated immediately. The embryos were then dissected, and hearts were carefully isolated with the help of a stereomicroscope and light source. Isolated heart tissues were cut into smaller fragments (~ 1 mm) using sterile scalpels. Tissue fragments were enzymatically digested by treatment with prewarmed 0.05% trypsin-EDTA solution for 8 min at 37 °C in a water bath with gentle mixing at regular intervals of 2 – 3 mins. The supernatant containing cell debris was discarded. Tissue fragments were treated with 100 µl DNase (10,000 units/ml) for 3 min at room temperature (RT) with gentle shaking to digest free-floating DNA that can cause tissue aggregation and interfere with enzymatic digestion. The supernatant was discarded, and the remaining tissue was treated again with 8 ml trypsin-EDTA for 8 min at 37 °C with gentle shaking at regular intervals. The supernatant was collected and resuspended in 6 ml blocking solution containing cell culture medium and fetal bovine serum (FBS) in a 2:1 ratio to stop enzymatic digestion.

The cell culture medium was prepared by dissolving 9.8 g of F10 Ham's powder in 1 L of distilled water and adding 5 ml of 7.5% sodium bicarbonate solution. The pH was adjusted to 7.2 using NaOH. The medium was sterile filtered and supplemented with 10% fetal bovine serum, a 1/100 dilution of an antibiotic solution (10,000 units penicillin and 10 mg/ml streptomycin in 0.9% NaCl) and a 1/200 dilution of ITS liquid media supplement containing insulin (1 mg/ml), transferrin (0.55 mg/ml), and sodium selenite (0.5 mg/ml) in Earle's balanced salt solution (EBSS) to obtain the final culture medium.

To digest the remaining tissue, DNase and trypsin-EDTA treatment steps were repeated once. The supernatant was collected and added to 6 ml blocking solution to stop enzymatic digestion. Collected supernatants containing the cells were centrifuged at 200×g for 10 min at 4 °C. The supernatant was discarded, and the cell pellet was resuspended in the culture medium. Cells were counted using a hemocytometer, and the desired concentration of cell suspension was prepared according to the experimental setup. Cells were cultured as described in

(Sridhar et al., 2020). To culture cells on glass substrates, Petri dishes with holes (diameter = 18 mm) were fitted with glass coverslips (coverslips with a thickness of $170 \pm 5 \mu\text{m}$) at the bottom. Prior to the seeding of cells, substrates were coated with $10 \mu\text{g/ml}$ human fibronectin in phosphate buffered saline (PBS) and incubated at $37 \text{ }^\circ\text{C}$ for 20 min. About 100,000 cells were seeded and cultured on the fibronectin-coated glass substrates in a humidified atmosphere with 5% CO_2 at $37 \text{ }^\circ\text{C}$. The cells were incubated overnight to attach under culture conditions. Cells were washed with prewarmed PBS the next day, and 2 ml of medium was added. The medium was replaced every second day in culture.

2.2.2 Preparation of biotin-conjugated fusogenic liposomes

Cell culture obtained from embryonic rat hearts primarily consisted of two distinct cell populations – the cardiomyocytes (CMs) and the non-myocytes (described in detail in section 1.1.1). The cardiomyocyte population was comprised of pacemaker cells and working cardiomyocytes, while the non-myocyte cell population was predominantly comprised of fibroblasts (Fbs). CMs were separated from remaining myocardial cells using fusion-based biotin-labeling of cells for subsequent magnetic cell-separation procedure as described in (Hersch et al., 2016). For biotin-labeling of cell membranes, fusogenic liposomes (FLs), composed of positive, neutral, and biotinylated lipids along with a lipid tracer, were prepared. The specific lipid composition of FLs enables membrane fusion. Fusogenic liposomes containing lipids 1,2-dioleoyl-sn-glycero-3-phosphoethanolamine (DOPE), 1,2-dioleoyl-3-trimethylammonium-propane (chloride salt, DOTAP), 1,2-dioleoyl-sn-glycero-3-phosphoethanolamine-N-(cap biotinyl) (sodium salt, biotin-DOPE) and 1,10-dioctadecyl-3,3,30,30-tetramethylindotricarbocyanine iodide (DiR) were prepared in the molar ratio 1/1/0.1/0.05. Fig. 2.1 shows the lipids used in the preparation of FLs. After gentle homogenization of lipids, the organic solvent (chloroform) was evaporated under vacuum for 30 min at RT. The lipid film was hydrated in 20 mM 2-(4-(2-hydroxyethyl)-1-piperazinyl)-ethansulfonic acid (HEPES) buffer (pH 7.4) to obtain a total lipid concentration of 2 mg/ml. The solution was mixed by carefully pipetting up and down and homogenized for 20 minutes in an ultrasonic bath at $5 \text{ }^\circ\text{C}$. FLs were stored at $-20 \text{ }^\circ\text{C}$ and thawed each time before use.

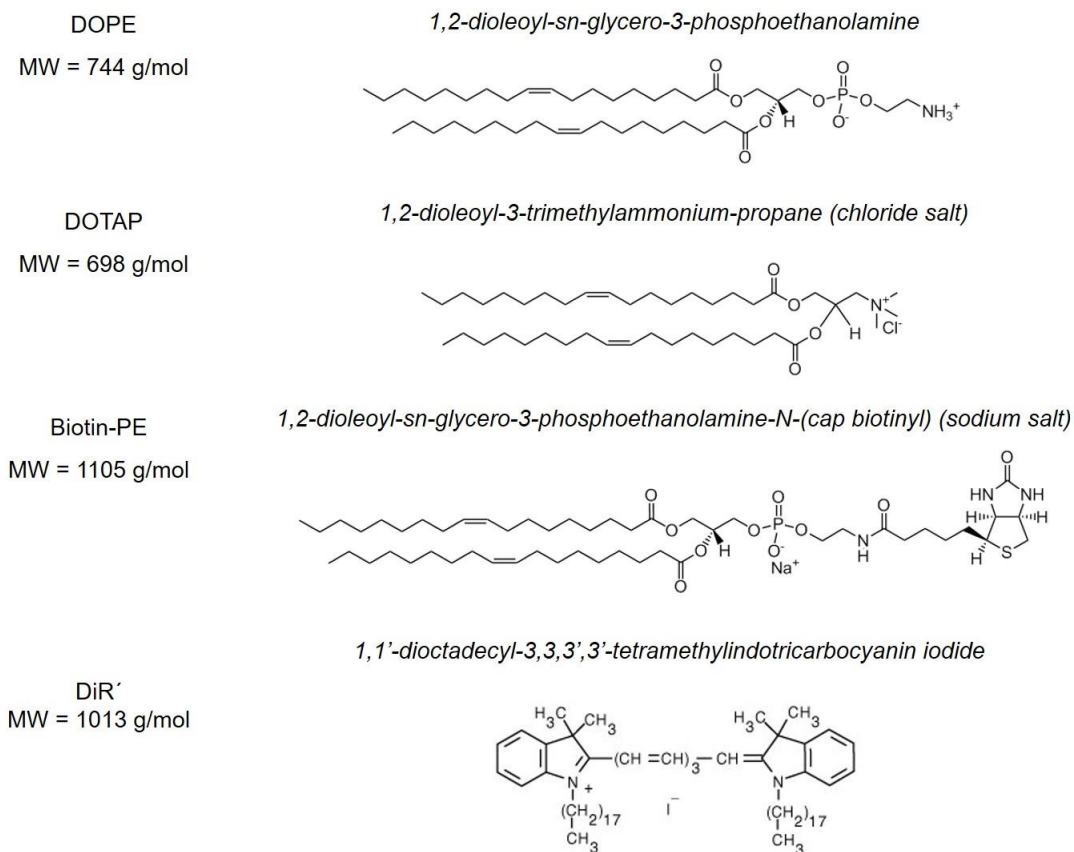


Figure 2.1: Lipid constituents of fusogenic liposome mixture: DOPE and DOTAP lipids are mixed in an equal molar ratio to obtain positively charged liposomes in addition of 2.5 mol% DiR. Liposomes prepared in this composition can fuse with cell membranes. For biotin functionalization of membranes, Biotin-PE was added to the mixture. Lipophilic tracer DiR was used to trace liposome activity upon binding to membranes.

2.2.3 Fusion-based magnetic separation of myocardial cells

Following primary cell isolation, a fraction of cells from the cell mixture was used for coculture preparations and the remaining cells ($1-2 \times 10^6$) were used for magnetic cell separation. As a first step, the cells were filtered through a nylon cell strainer to remove any remaining cell debris/tissue fragments that could hinder the cell separation process. FLs (refer section 2.2.2) were thawed, mixed well and homogenized in an ultra-sonication bath for 5 min at a temperature below RT. The FLs were added at a dilution of 1:50 to 1 ml Dulbecco's modified eagle medium (DMEM), and the solution was sonicated again for 3 min below RT. Freshly isolated myocardial cells were centrifuged at $200 \times g$ for 3 min at 4 °C. The supernatant was discarded, and cell pellet was resuspended in 1 ml FL-solution for 2 min at RT. Fusion was stopped by adding 2 ml culture medium to the cell suspension.

After biotinylation, cells were centrifuged at $800\times g$ for 3 min. The cell pellet was resuspended in a mixture of 20 μl anti-biotin magnetic microbeads and culture medium at 1:5 dilution and incubated at $4\text{ }^{\circ}\text{C}$ for 20 min. The cell suspension was diluted in 2 ml culture medium and subsequently centrifuged for 3 min at $800\times g$ at $4\text{ }^{\circ}\text{C}$. The cell pellet was resuspended in 1 ml culture medium and introduced into the MiniMacs magnetic column attached to a movable stand. The cells labeled by anti-biotin magnetic microbeads were retained in the column due to the strong magnetic field. Due to high fusion efficiency for non-myocytes and low efficiency for CMs, the flow-through was enriched with CMs while the magnetically labeled non-myocytes were retained in the magnetic field. Removing the magnetic field freed the attached cells and enabled cell collection. A schematic illustration of steps involved in magnetic separation of cells is shown in Fig. 2.2 a-c. The cells from the eluate and retentate were counted and cultured separately on fibronectin-coated ($10\text{ }\mu\text{g/ml}$) cell culture dishes at a concentration of 100,000 cells/dish.

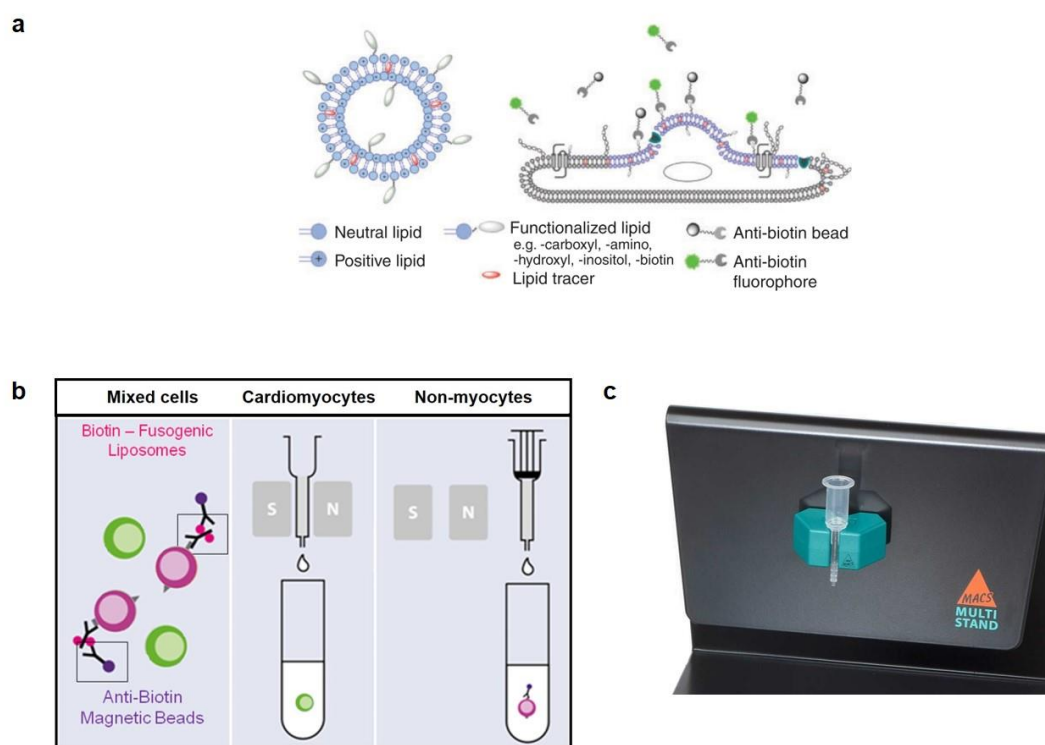


Figure 2.2: Schematic illustration of magnetic labeling and separation of myocardial cells: **a)** Schematic showing biotin-functionalized fusogenic liposome (left) and fusion of liposomes with cell membrane. Adopted from (Hersch et al., 2016). **b)** Illustration of fusion-based magnetic separation of myocytes and non-myocytes from the cell mixture. Magnetic labeling with anti-biotin magnetic microbeads enabled retention of non-myocytes in the column due to a high magnetic field. Cardiomyocytes were eluted through the column and collected in the flow-through. Non-myocytes were collected following the removal of the magnetic field. **c)** Magnetic column attached to the mobile magnetic stand used for the separation of cardiomyocytes from non-myocytes. (Modified from www.miltenyibiotec.com).

2.3 Live cell calcium imaging in cultured myocardial cells

To study the dynamic spatial and temporal changes in intracellular calcium concentration ($[Ca^{2+}]_i$) in cultured myocardial cells, calcium imaging was performed by fluorescent labeling of intracellular Ca^{2+} ions using the calcium indicator Fluo-4 AM (Fig. 2.3 a). The dye is cell-permeant, and hydrolysis of the acetoxymethyl (AM) esters from the dye by non-specific intracellular esterases sets the Fluo-4 dye free. The dye can then bind to Ca^{2+} ions in cells. Binding of Ca^{2+} ions to the dye results in increased fluorescence. The maximum absorbance was found at 494 nm, and the maximum emission occurred at 516 nm (Fig. 2.3 b). Fluorescence emission occurred upon Ca^{2+} binding to the dye. The typical fluorescence intensity increase on Ca^{2+} binding (F_{max}/F_{min}) was shown to be greater than 100-fold (Gee et al., 2000). The indicator was, therefore, suitable for qualitative analysis of variation in $[Ca^{2+}]_i$ based on spatial and temporal changes in fluorescence intensity relative to an applied physiological stimulus.

Calcium imaging was performed as described previously in (Sridhar et al., 2020). For calcium imaging, cultured cells were washed with a pre-warmed culture medium prior to Fluo-4 labeling. Fluo-4 AM was added to cells at a final concentration of 5 μ M in culture medium and incubated for 20 min at 37 °C. Cells were washed twice with a culture medium to remove unbound extracellular fluorophore. Cells were further incubated at 37 °C for 10 min in the dark prior to imaging to allow the intracellular esterases to denature the AM esters so that a stable Ca^{2+} -fluorescence imaging could be achieved. For Ca^{2+} imaging under a confocal microscope (LSM880) the fluorophore was excited by an argon laser (488 nm) and detected with a 490-550 nm bandpass filter. Ca^{2+} changes in cells were recorded by continuous imaging at a frame capture time of 160 ms per frame with a confocal microscope using 20x Plan-Apochromat objective with a numerical aperture (NA) of 0.8 and a pixel size of 1.66 μ m. For Ca^{2+} imaging experiments that required a larger field-of-view, continuous imaging was performed at a frame capture time of 235 ms per frame and a pixel size of 2.77 μ m. In cultured myocardial cells labeled with Fluo-4, $[Ca^{2+}]_i$ changes at various time-points can be seen from time-series images in Fig. 2.3 c. Here, a high fluorescence intensity represents the contracted state of CMs (high $[Ca^{2+}]_i$) while a low intensity represents the relaxed state (low $[Ca^{2+}]_i$) (refer section 1.2.3). For non-myocytes in cocultures, the $[Ca^{2+}]_i$ oscillations were minimal compared to the CMs (described later).

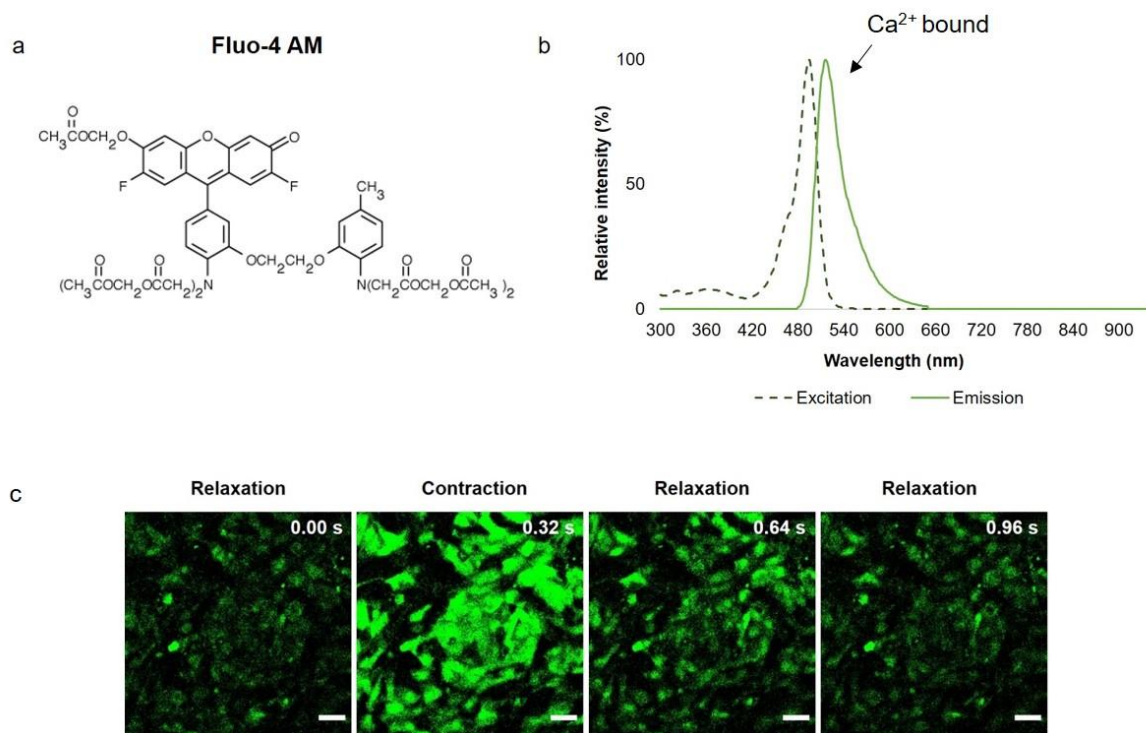


Figure 2.3: Imaging dynamic calcium (Ca^{2+}) changes in cultured cardiomyocytes: a) Chemical structure of Fluo-4 AM Ca^{2+} indicator. (Source: www.thermofisher.com). **b)** Fluorescence spectrum of Fluo-4 indicator showing the maximum absorption wavelength (494 nm) and maximum emission wavelength upon Ca^{2+} binding (516 nm) (Gee et al., 2000). **c)** Ca^{2+} -induced fluorescence intensity in Fluo-4 labeled coculture cells depicting the intracellular Ca^{2+} concentrations in cells for the indicated time-points. The change in intracellular Ca^{2+} concentrations shows the contracted (high Ca^{2+} concentration) and relaxed states (low Ca^{2+} concentration) of cardiomyocytes. Modified from (Sridhar et al., 2020). Scale bars: 50 μm .

2.4 Targeted killing of single cells by laser ablation

2.4.1 Principle of laser ablation

Single cell-death in myocardial cell clusters was induced by the technique of laser ablation. In general, light manipulation techniques of cells or tissues can be classified into non-invasive and invasive methods. The non-invasive approach concerns the exploitation of optical forces, as in optical tweezers, to manipulate cells as well as molecules within the living cells. The latter involves exploiting the energy of high photon flux to overcome the break-down threshold of the sample and induce local ablation (Oddershede, 2012; Soloperto et al., 2016). Laser ablation technique has been successfully employed to study the dynamic response of cells/tissues to mechanical injury (Morsch et al., 2017; Narciso et al., 2015; Smutny, Behrndt, Campinho, Ruprecht, & Heisenberg, 2015). As a primary advantage, laser-based ablation is a very flexible method that can be performed at any cellular site, in any size or pattern and at any time in

development within living tissues and cells. It allows severing of biological tissues with a precision in the range of nanometers and moreover enables local perturbation of molecular structures within a single cell or even a subcellular compartment. With an accurate choice of parameters such as laser wavelength, pulse repetition rate, pulse duration and pulse energy, the interaction of light with biological matter can be tuned to perform analyses ranging from reversible manipulations to irreversible hard cuts in cells (Soloperto et al., 2016). For selective manipulation, a laser beam is focused on the cells through a microscope objective. The interaction of the laser with the cells is dependent on the parameters mentioned above. The various events following laser irradiation of living cells *in vitro* are described in detail below.

a. Light-matter interaction and plasma formation

Selective killing or removal of cells from a tissue/cell cluster in a biological medium can be described based on the principle of laser ablation in the liquid phase (Kanitz et al., 2019). When a laser beam is focused on a solid target in a liquid phase, it causes fast phase-transition at target-liquid interphase. In a time scale of nanoseconds (ns), melting of the target material and phase explosion (or explosive boiling) leads to a dense plasma formation (described in detail later) that results in material rupture and cavitation.

Laser pulses can be classified into ultrashort (femtosecond and picosecond range) and short pulses (nanosecond range). The similarities and differences in the mode of ablation of these pulses are well described in (Kanitz et al., 2019; A. Vogel, Noack, Hüttman, & Paltauf, 2005). Here, the process of ablation using a short pulse laser is focused on in detail. The short laser pulses are focused on the target cell in the biological medium through an objective lens. At the target surface, the light is partially absorbed and reflected. The degree of absorption and reflection depends on the dielectric function of the target material (Kanitz et al., 2019).

Plasma is a state of matter when electrons and ions are not bound together and behave separately. The conditions an ionized gas must satisfy to be called plasma are detailed in (Kanitz et al., 2019). The growth of the plasma occurs as a two-step process. In the first step, bound electrons are freed from their molecular orbitals by interaction with the electric field of the laser pulse. In the second step, the free electrons seed an impact ionization cascade that involves the acceleration of the electrons by inverse-Bremsstrahlung absorption, in which an electron absorbs photons while colliding with molecules. After several absorption events, the free electrons achieve sufficiently high kinetic energy to ionize another molecule by impact

ionization. This cascade, along with the continued generation of photoelectrons, leads to the exponential growth of a micrometer-sized plasma bubble. The plasma density can only grow up to the limit of the critical electron density, above which the laser beam cannot penetrate the plasma anymore. Due to absorption and reflection as well as high plasma densities, laser beam shielding can lead to a decrease in ablation efficiency, especially for long ns laser pulses. Hence, for ns laser pulses, the laser-matter interaction is strongly associated with laser-plasma interaction (Kanitz et al., 2019).

For nanosecond pulses, no free electrons are formed for irradiance values below the optical breakdown threshold because the irradiance is too low to provide seed electrons by means of multiphoton ionization. Once the irradiance is high enough to provide a seed electron, the ionization cascade can start. It proceeds very rapidly owing to the high irradiance. The electron density shoots up by nine orders of magnitude within a small fraction of the laser pulse duration until its rise is stopped by recombination. The breakdown threshold is, hence, extremely sharp – either a highly ionized plasma is produced or no plasma at all (A. Vogel et al., 2005).

Laser ablation in the liquid phase results in a transient plasma formation. The transient plasma evolution induced by laser ablation can be divided into three different stages: Plasma ignition – during the energy transfer from the laser beam onto the target material; Plasma expansion – when the energy deposited by a pulsed laser beam is very high and deposited into a confined volume at the target surface. This volume expands into the surrounding, exciting the adjacent medium. During this phase, energy is transferred partially from the plasma into the surroundings, but a plasma state remains. This temporal phase depends on the laser pulse duration and can range from some ns to several hundred ns; Plasma cooling and quenching – when the plasma strongly interacts with the surrounding environment and as a consequence dissipates energy. The quenching mechanisms begin to dominate over plasma sustaining processes, and the plasma cools down. This phase can range up to several microseconds. The presence of liquid as a confining environment has a profound impact on the ablation process – a) the liquid prevents a free expansion of the ablated target material through mechanical confinement and b) through the direct contact of the target material and liquid, the liquid provides an additional channel of energy dissipation (thermal confinement) and chemical reaction dynamics (Kanitz et al., 2019).

Ablative material-removal from the cell requires the fracture of chemical bonds. The breakage of bonds leads either to the removal of molecular fragments or to the formation of voids within the bulk of the material. Void (i.e., bubble or crack)-formation results in the ejection of non-decomposed material fragments upon mechanical failure of the material. Vaporization, molecular fragmentation, and void formation are all phase transitions and can be accomplished via photothermal, photomechanical, or photochemical mechanisms (Alfred Vogel & Venugopalan, 2003).

b. Cavitation bubble

As the plasma cools down, its energy is transferred to the liquid through different energy dissipation channels resulting in the phase transition of the liquid. The phase transition of the liquid is accompanied by the formation of a thin vapor film around the plasma boundary with a strong shape correlation to the plasma itself. This thin vapor film is considered as the birth of the cavitation bubble (Dell'Aglio, Gaudiuso, De Pascale, & De Giacomo, 2015). The interaction of the cavitation bubble with plasma is dependent on pulse duration. For short pulses, the plasma emission exceeds the boundary of the cavitation bubble, indicating a strong interaction of the plasma with the bulk liquid and maybe even an injection of excited species into the bulk liquid. For long pulses, the plasma remains within the boundary (Kanitz et al., 2019). Using water or a biological medium, cavitation can be generated by the formation of bubbles or the explosion of cell membranes due to high internal pressure caused by shockwave propagation (Colombelli, Grill, & Stelzer, 2004). The ns-laser-induced bubble generation was associated with cell death. Further, nuclear staining of non-viable cells with ethidium bromide had revealed that cell death following ablation was found to be associated with membrane damage (A. Vogel et al., 2005).

The development of the cavitation bubble can be subdivided into three different stages described by the cavitation bubble expansion, shrinking and collapse (Tomko et al., 2015). In the early growth phase, the shape of the cavitation bubble follows the development of the plasma immediately after the arrival of the laser pulse for a tenth of nanoseconds, indicating that the plasma and the cavitation bubble coexist (Kanitz et al., 2019). With lifetimes up to several hundred microseconds, the cavitation bubble exceeds the lifetime of the plasma by far. The cavitation bubble expands, and after reaching a stationary point with a maximum size, it begins to shrink. The collapse of the cavitation bubble results in the propagation of a shockwave. Further, a rebound of the cavitation bubble induces the formation of one or more

following cavitation bubbles. For each collapse, a part of the mechanical energy of the cavitation bubble is released through the emission of a new shockwave (Tsuji, Tsuboi, Kitamura, & Tsuji, 2004). The different processes involved in laser ablation is illustrated in Fig. 2.4.

In addition to the choice of laser pulse parameters for ablation of cells *in vitro*, the choice of laser wavelengths is also important. Laser wavelengths in the range of UV-A (315-400 nm) are highly suited for ablation of cells/cellular target, whereas UV-B (280-315 nm) is highly absorbed by DNA, which may hinder the experimental inference and UV-C (100-280 nm) absorption is too high by turbid media and requires special optical elements. Using a pulsed UV laser with ns range pulse width and a high NA lens, low energy ablation (due to the short pulse) in a highly confined volume (due to the short wavelength of 355 nm) is possible (Colombelli et al., 2004).

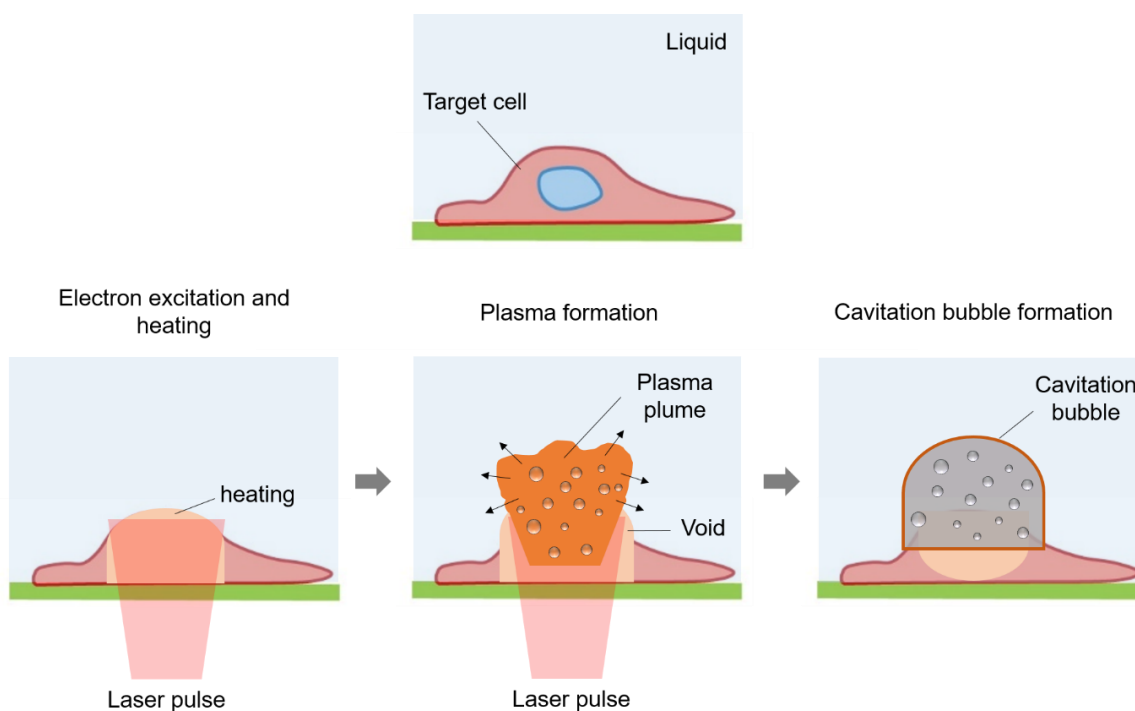


Figure 2.4: Processes involved in laser ablation: Schematic illustration of the various processes involved in laser ablation of a cell in a liquid medium based on (Kanitz et al., 2019). Following laser irradiation of the target, the bound electrons are freed from their molecular orbitals by interaction with the electric field of the laser pulse. The free electrons seed an impact ionization cascade that involves the acceleration of the electrons by inverse-Bremsstrahlung absorption. After several absorption events, the free electrons achieve sufficiently high kinetic energy to ionize another molecule by impact ionization. This cascade, along with the continued generation of photoelectrons, leads to the growth of a plasma plume. An increase in pressure within the excitation volume can produce a rupture of the material and form a cavitation bubble. The bubble constitutes the region of ablation. The expansion of the cavitation bubble is associated with a shockwave that also propagates into the surroundings.

2.4.2 Laser ablation experimental setup

Laser-induced targeted killing of cultured myocardial cells was performed using a pulsed UV laser coupled to a confocal imaging setup by the procedure described in (Sridhar et al., 2020). The interaction of the laser beam with the cells and the mode of cell death is described in detail in section 1.4.2. The pulsed UV laser (diode-pumped solid-state (DPSS) laser; safety class 3B) emitted radiation of wavelength (λ) 355 nm with a repetition rate of 1.2 kHz, a peak power of 42 μ J and a pulse duration of 1.4 ns. Fig. 2.5 a shows a simplified schematic illustration of the laser beam path along with the confocal beam path used in laser ablation experiments. A point scanning device (UGA-firefly) equipped with the pulsed UV laser source was coupled to the microscope through dichroic mirrors. The device allowed parallel coupling of fluorescence light source simultaneous imaging and ablation.

The ablation system was integrated into the microscope's hardware and software and controlled using the ROE-SysCon software. As a first step, confocal images were replicated real-time in the software for simultaneous image acquisition and laser ablation. The laser beam was calibrated in x, y, and z directions to cut cells precisely. Calibration in x and y axes was performed using the in-built interactive calibration routine (manual calibration mode) in the software to ensure that the laser cut at the defined boundary/shape. For calibration in x and y, a petri dish fitted with a glass coverslip (refer section 2.2.1) without cells was marked with a fluorescent marker. The laser cut on the marked (green) glass coverslip before and after calibration can be seen in Fig. 2.5 b. Calibration in z-direction was performed to focus the laser beam on to the desired focal plane, i.e., the cell surface. Calibration was performed for every objective type (20x / 40x) and substrate material (Glass / polydimethylsiloxane (PDMS)) used. Focus position was selected from one of the specific prefixed positions based on the magnification, NA of the objective and the substrate on which cells were cultured. The effective laser power and number of iterations were chosen depending on the experimental setup.

Single cells cultured on glass substrates were selectively irradiated with a laser intensity of 2 – 5% of total laser output for a duration of 1 – 2 s to achieve 1000-2000 short pulses. Immediate effects of single-cell ablation were recorded using continuous imaging in the time-series experiment mode for a duration of ~ 5 min for short-term experiments. For long-term experiments, continuous imaging was performed for ~ 25 min post ablation. Laser-induced cell death was confirmed by the rupture/damage of cells seen from phase-contrast images and/or from changes in Ca^{2+} -induced fluorescence intensity in Fluo-4 labeled cells.

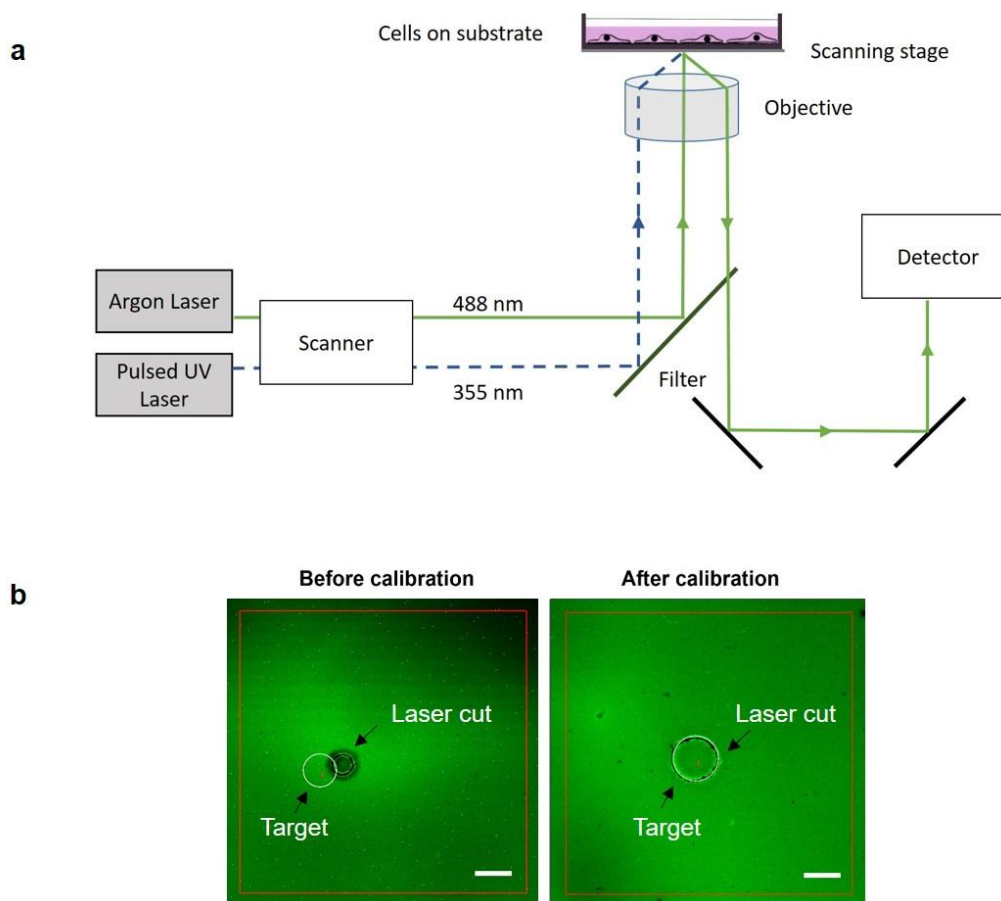


Figure 2.5: Schematic illustration of laser ablation setup: a) A simplified scheme of laser ablation of cells, showing the confocal setup coupled with a pulsed UV laser for selective killing of single myocardial cells in culture. An argon laser was used to excite the Fluo-4 fluorophore with a 488 nm laser line, while the UV laser was used to produce a laser pulse of 355 nm wavelength for irradiation and subsequent killing of the target cell. Fluorescent signals from the irradiated sample were detected and amplified by the photomultiplier (PMT). b) Images depicting the laser cut at defined target (circle) on a glass substrate marked with a fluorescent marker (green), before (left) and after (right) calibration of the UV laser beam prior to laser ablation experiments. Calibration in x, y and z directions enabled precise cut on the target region. Scale bars: 50 μm .

2.5 Preparation of patterned cultures of cardiomyocytes and non-myocytes using cell culture-inserts

In order to study the interaction of CMs and non-myocytes in detail, defined clusters of cells were prepared using culture inserts. The inserts consisted of three wells/chambers that allowed co-cultivation of cell clusters. These inserts, made of silicone, were non-reactive and non-toxic to the cells. Each well in the insert was separated by a distance of $500 \pm 100 \mu\text{m}$ and was bound by walls on all sides that prevented leakage of cells/medium, as shown in Fig. 2.6. To culture cells, the culture-inserts were firmly fixed by pressing the insert's sticky underside onto the fibronectin (10 $\mu\text{g/ml}$) coated glass substrates. Freshly isolated cells were counted and seeded

onto each well at a concentration of 30,000 – 40,000 cells in 100 μ l of medium per well. Coculture cells were seeded onto the central well while the other two wells were seeded with CMs obtained from the fusion-based magnetic cell separation process (refer section 2.2.3). The cells were allowed to attach to the substrates overnight in a humidified atmosphere at 37 $^{\circ}$ C and with 5% CO₂. The inserts were carefully removed the next day, and the cells were washed with prewarmed PBS. Fresh culture medium was added to cells and was replaced every second day. Upon removal of insert, non-myocytes in clusters proliferated over time. Cells were fixed and immunolabelled to distinguish CMs from non-myocytes in the culture on day five after removal of the insert using the procedure described later. Calcium imaging and laser ablation experiments were performed on cells (refer sections 2.3 and 2.4) cultured in the above-described pattern to analyze functional connectivity between CMs and fibroblasts.

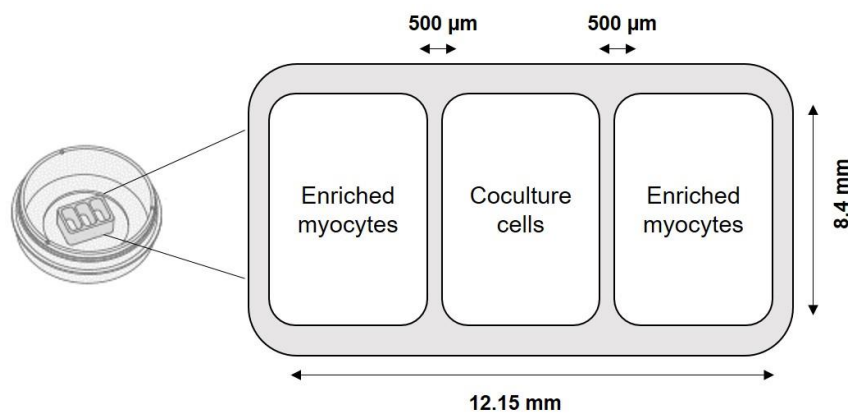


Figure 2.6: Culture of myocardial cells in wound-healing inserts: Schematic illustration of myocardial cell clusters in three-chambered silicone culture inserts. In these inserts, cells were co-cultivated in each chamber separated by a distance of about 500 μ m from each other. The coculture cells were cultured onto the central well, while cardiomyocytes obtained after the fusion-based magnetic separation procedure were cultured onto the remaining wells. The wall separating the wells prevented leakage of cells/medium across the wells. Following cell attachment overnight, the insert was removed to culture cells freely.

2.6 Western blot

Western blot was performed to detect the presence of specific proteins in the total protein-isolate from heart tissues and cultured myocardial cells. To isolate proteins from the heart tissue, 5-6 embryonic hearts from decapitated embryos (refer section 2.2.1) were immediately treated with liquid nitrogen to snap freeze the tissue. The tissue was then transferred into a homogenizer and treated with a lysis buffer solution containing radioimmunoprecipitation

assay (RIPA) lysis buffer (made up of 150 mM NaCl, 1 % IGEPAL CA-630, 0.5 % sodium deoxycholate, 0.1 % sodium dodecyl sulfate (SDS), 50 mM Tris, pH 8.0) and protease inhibitor cocktail in the ratio 50:1. A volume of 300 μ l of the lysis buffer solution was used for the lysis of ~ 5 mg of tissue. The sample was incubated on ice for 30 min.

For protein isolation from cultured cells, cells cultured on 6-well plates were washed once with cold PBS. The cells were mechanically detached from the surface using a cell scraper. The solution containing lysis buffer and protease inhibitor was added to the cells, collected after 2 min and incubated at 4 °C for 20 min. The protein isolates from tissue and cells were centrifuged at 16000 rpm for 20 min at 4 °C. The supernatants were collected and mixed with a loading dye (4x Laemmli buffer containing 62.5 mM Tris-HCl, pH 6.8; 10% glycerol, 1% lithium dodecyl sulfate and 0.005% Bromophenol Blue) in the ratio 5:1. The mixture was heated to 95 °C in a heating block for 5 min to denature the proteins. The samples were stored at -80 °C until protein analysis. Prior to western blot analysis, the protein samples were thawed, and the required volume was transferred to a new reaction tube.

For gel electrophoresis of the protein samples, a ready-to-use polyacrylamide gel (4-20% gradient gel) with a maximum capacity of 30 μ l for each well was used. The gel was gently fixed on to the gel electrophoresis tank that was connected to a power source. The tank was filled with running buffer such that the wells were covered with the buffer. A sample volume of 24 μ l was added to the wells. The protein ladder (10-250 kDa) was added at a volume of 6 μ l to the first and last wells for reference. The power source set to constant current and the voltage was set to 90 V. After 30 min, the voltage was raised to 120 V and electrophoresis was carried out for 90 min to separate proteins based on their molecular weight.

Following electrophoresis, the gel containing proteins were carefully removed from the electrophoretic tank. To transfer proteins from the gel to a blot, a tight assembly of the gel and a nitrocellulose membrane in the presence of transfer buffer was used to avoid air bubbles that may affect an efficient transfer. The gel was carefully placed on top of a filter paper soaked in the transfer buffer. The gel and filter paper was then placed on top of a sponge. A similar setup was used for the membrane. The gel and the membrane were packed gently, facing one another into a cassette along with the sponge and filter paper at either end of the cassette. The cassette was gently transferred into an electrophoresis tank containing transfer buffer and connected to a power source. The power was switched on and set to a constant voltage of 50 V. The transfer was performed overnight at 4 °C.

After overnight transfer of proteins, the membrane was washed within the transfer buffer. The membrane was treated with a 5% solution of dry milk in 1x tris-buffered saline (TBS) for 2 hours at RT with gentle shaking in a shaker. Monoclonal antibodies - Mouse anti-actin clone C4 and Mouse anti-connexin43 were added at a dilution of 1:500 to 1% solution of milk powder in TBS to the membrane. The membrane was incubated with primary antibodies overnight at 4 °C with gentle shaking. The membrane was then washed thrice with a washing solution containing 0.1% Tween-20 surfactant in TBS. Goat anti-mouse secondary antibody conjugated to alkaline phosphatase was added to the membranes at a dilution of 1:1000 in 1% milk solution in TBS and incubated at RT for 3 hours with gentle shaking. The antibody was washed thrice with the washing solution and once with distilled water. The substrate (5-Bromo-4-chloro-3-indolyl phosphate - nitro blue tetrazolium liquid substrate) solution was added to the membranes at a volume of 0.5 – 1 ml. Upon catalysis by alkaline phosphatase enzyme conjugated to the antibody, 5-Bromo-4-chloro-3-indolyl phosphate reacts with nitro blue tetrazolium to yield a dark blue to purple colored insoluble precipitate. Upon color development (blue/purple), the membrane was washed twice with distilled water. The blot was dried and was then imaged using the GelDoc documentation system to analyse the presence of the target proteins based on their molecular weight.

2.7 Immunocytochemistry

Cultured cells were fixed in formaldehyde solution (3.7%) in cytoskeletal buffer (CB) – 150 mM NaCl; 5 mM MgCl₂; 5 mM ethylene glycol-bis(2-aminoethylether)-N,N,N',N'-tetraacetic acid (EGTA); 5 mM glucose; 10 mM 2-(4-morpholino)ethanesulfonic acid (MES); pH 6.1 (Hersch et al., 2016). After fixation, the cells were treated in 100 mM glycine solution in CB for 20 min at RT to quench the remaining formaldehyde in the sample. Membrane permeabilization was performed using 0.5 % Triton-X-100 solution in CB for 10 min. Unspecific labeling was reduced by incubating cells with a blocking solution (5% solution of dry milk in CB) for 90 min. Cells were then incubated with a 1:100 dilution (in 1% solution of dry milk in CB) of primary antibodies - Mouse sarcomeric anti- α -actinin, clone EA-53 monoclonal antibody, Mouse monoclonal anti-connexin43 antibody, Rabbit polyclonal anti-connexin43, Rabbit polyclonal anti-connexin40 and Rabbit polyclonal anti-connexin45 overnight at 4 °C. Cy3-conjugated goat anti-mouse and Alexa fluor 546 Goat anti-rabbit secondary antibodies were used at 1:200 dilution (in 1% solution of dry milk in CB). For F-actin labeling, CytoPainter Phalloidin-iFluor488 / Phalloidin-iFluor633 was added to the cells at 1:300 dilution in parallel to the secondary antibodies and incubated at RT for 2 hours. For

nuclear staining, NucBlue was added to the cells after secondary antibody incubation as per the manufacturer's guidelines. The samples were stored in CB for confocal microscopy.

The fluorophores were simultaneously excited with 405 nm, 488 nm, 561 nm and 633 nm laser lines, and the emission was detected with 415-475 nm, 490-550 nm, 550-600 nm and 635-675 nm bandpass filters. Tile-scanning was performed using a motorized scanning stage (centered grid scanning) to obtain overview images of samples around the existing stage position (Sridhar et al., 2020). An EC Plan-Neofluar 40x oil objective (NA 1.3) was used to image an area of 1.55 mm × 1.55 mm, divided into 64 (8 × 8) tiles with 10% overlap of the tiles (rectangular grid tiling mode). The LSM based built-in autofocus (ZEN software) was used to compensate for the z-drift and was set for every four tiles. The autofocus was set to fluorescence mode, which is ideally suited for imaging monolayers with stained nuclei where the nuclei provided an ideal reference plane for imaging. The tile images were stitched together using the built-in online stitching tool (ZEN, Carl Zeiss; threshold value of 0.7; overlap of 10%) during acquisition to obtain a single overview image of the culture.

2.8 Traction force microscopy

2.8.1 Principle of traction force microscopy

Cells exert force on the substrates to which they have adhered. These forces are generated by contractile filaments in the cells and are essential for physiological processes such as cell migration, contraction, growth and differentiation (Geiger, Bershadsky, Pankov, & Yamada, 2001). The generated forces are transmitted to the adjacent cells via cell-cell contacts while they are transmitted to the extracellular matrix (ECM) via focal adhesions as described in sections 1.1.2 and 1.2.1. Focal adhesions are integrin-based multi-protein complexes that link the cell's cytoskeleton to the ECM, thereby facilitating the transmission of forces exerted by the cells to its environment (Geiger, Spatz, & Bershadsky, 2009).

Methods to measure the forces exerted by cells on to substrates were developed after Harris and colleagues described wrinkles on thin sheets of silicone rubber caused by traction forces exerted by the cells (A. K. Harris, Wild, & Stopak, 1980). Traction forces are tangential forces exerted by the cells through which they can sense mechanical and geometrical features of their environment. The presence of contractile (actomyosin) apparatus in cells results in continuous exertion of these forces on to the substrates (J. H. C. Wang & Lin, 2007). A method to measure traction forces exerted by cells on to substrate was described by (Cesa et al., 2007; Merkel, Kirchgessner, Cesa, & Hoffmann, 2007). In this method, the cells were cultured on soft

elastomeric substrates of finite thickness. In this approach, the wrinkling effect was suppressed by using soft elastic layers coated on glass coverslips. Cell forces act on the top surface of these elastic layers, which were able to move. Fluorescent microbeads were covalently coupled to the substrates and the displacement of beads due to the forces exerted by the cells were traced. From the deformation field resulting from bead displacement, the force exerted by the cells on the substrate could be measured.

A schematic illustration of cell traction forces acting on bead-coupled soft cross-linked silicone elastomer of finite thickness is shown in Fig. 2.7. The fluorescent bead-coupled substrates with cells and without cells are imaged under the confocal microscope. Comparison of bead positions in the presence of cells on the substrate and after enzymatic removal of cells can indicate the contractile forces exerted by the cells (Plotnikov, Sabass, Schwarz, & Waterman, 2014). Moreover, measurement of traction force-changes with time can provide an understanding of cellular dynamics, especially upon the introduction of a stimulus that perturbs the force balance in cells (J. Wu, Dickinson, & Lele, 2012). In this work, cross-linked PDMS elastomers of finite thickness were used to analyze cell traction forces. PDMS elastomers were used as they are biocompatible and do not take up water. Therefore, cross-linked PDMS elastomers can be stored and characterized in ambient air. Moreover, surface functionalization can be performed on these elastomers as proteins attach to the hydrophobic surface by physisorption. No flow of solvent occurs within the material upon force application (Cesa et al., 2007).

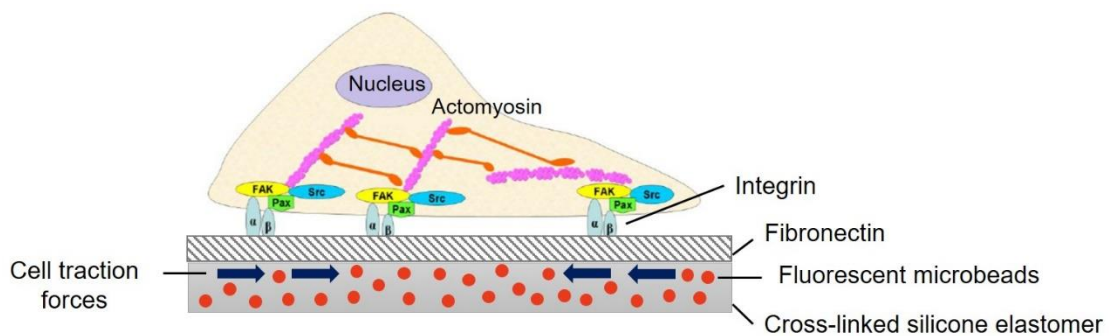


Figure 2.7: Traction forces exerted by a cell on soft elastomeric substrates: Schematic illustration of traction stress exerted by a cell on an elastomer substrate to which fluorescent microbeads are covalently coupled. The substrates are coated with extracellular matrix protein fibronectin to facilitate cell adhesion to the substrate. Cells adhere to the substrate via focal adhesions. While contractile filaments are essential for force generation, focal adhesions are essential for the transmission of forces to the substrate. Modified from (J. H. C. Wang & Lin, 2007).

2.8.2 Preparation of traction force substrates

To analyze the traction force-changes over time, clusters of CMs were cultured on soft elastomeric substrates with covalently-coupled fluorescent microbeads. Soft elastomeric material was prepared by mixing PDMS base (vinyl terminated polydimethylsiloxane) and cross-linker (methylhydrosiloxane–dimethylsiloxane copolymer) in the ratio of 50:1 thoroughly to obtain substrates of 15 kPa stiffness as described in (Cesa et al., 2007). The elastomer mixture was degassed by a vacuum pump for 30 min to remove air bubbles formed during mixing of the base and curing agent. To prepare substrates with uniformly distributed elastomer, elastomeric material was spin-coated on to glass coverslips (1.5# high-precision coverslips with a thickness of 170 +/- 5 μm) in a spin-coater at 1700 rpm for 15 s to obtain elastomer thickness of 70 μm . Spin-coated substrates were incubated at 60 °C for exactly 16 hours to enable crosslinking of the elastomer.

Fluorescent microbeads were coupled to the elastomers based on (Merkel et al., 2007). In order to couple fluorescent beads, the elastomeric substrates were first silanized with 400 μl trichloro(1H,1H,2H,2H-perfluorooctyl)silane prepared from (9.5 ml silane buffer (containing 5 % distilled water and 95 % ethanol; pH adjusted to 4.5-5.5 with acetic acid) and 0.5 ml 3-aminopropyltriethoxysilane and incubated for 3-4 min at RT. The substrates were washed thrice with ethanol and dried in vacuum for 30 min at RT. Activated microbeads solution was prepared by addition of coupling buffer (50 mM MES, pH 6.0 with NaOH (4.88 g MES in 500 ml distilled water), preheated SDS (10%), microbeads (FluoSpheres carboxylated 0.2 μm , crimson), 1-ethyl-3-(3-dimethylaminopropyl)carbodiimide and N-hydroxysulfosuccinimide and incubation for 15 min at RT. Beads were coupled to the prepared elastomer by adding 200 μl activated bead solution to silanized surfaces and incubated at RT for 10 min. The substrates were washed thrice with distilled water and were subsequently stored in PBS at 4 °C.

2.8.3 Cell culture

For traction force analysis of CM clusters, cardiomyocytes-enriched cultures were used. Following the fusion-based magnetic cell separation procedure (refer section 2.2.3), about 80,000 cells were seeded on to the bead-coupled elastomeric substrates. For simultaneous analysis of calcium and traction force changes in cell clusters, 3-day old cultures were treated with Fluo-4 AM as described previously in section 2.3. Imaging was performed with LSM880 using a 40x C-Apochromat Corr M-27 water immersion objective (NA 1.1). For calcium imaging, the 488 nm Argon laser line was used while a 561 nm DPSS laser line was used for

bead imaging for traction force analysis. A bandpass filter of 490-535 nm and 561-650 nm was used for calcium and bead imaging respectively. Clusters of contracting cardiomyocytes were chosen. Prior to ablation experiments, the UV laser beam was calibrated to cut cells on soft elastomeric substrates (15 kPa stiffness). After calibration, time-series imaging was set up with image frame size set to 512 x 512 pixels to image an area of 212.55 x 212.55 μm (pixel size of 0.42 μm) frame capture time set to 320 ms per frame. Fig. 2.8 a-c shows an enriched cardiomyocytes cluster on a bead-coupled substrate. To analyze cell force-changes before and after ablation, the selected cardiomyocyte cluster was imaged to record at least five contractions prior to ablation.

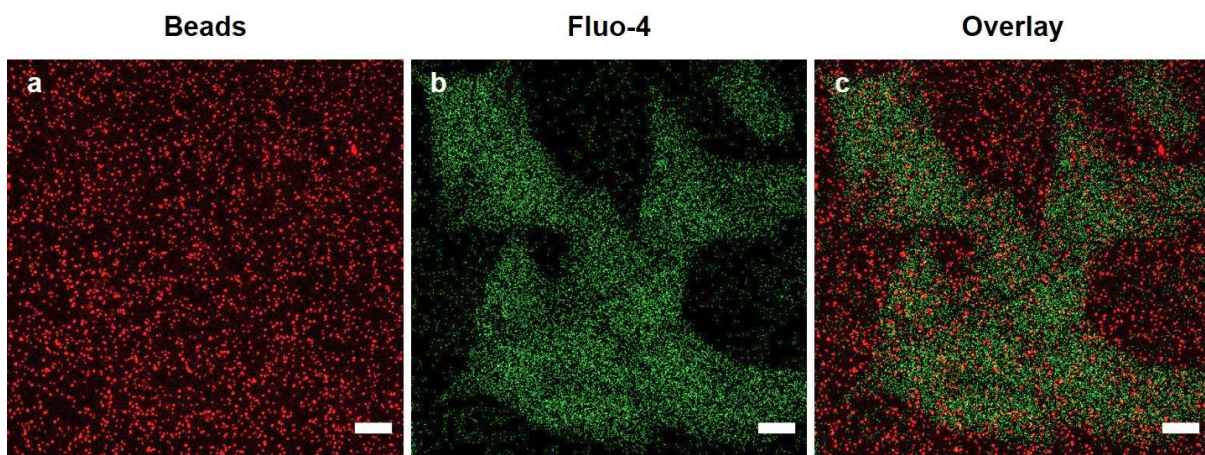


Figure 2.8: Cluster of cardiomyocytes cultured on bead-coupled elastomeric substrates: **a)** Image showing fluorescent beads (red) covalently coupled to elastomeric (PDMS) substrates on which cardiomyocytes were cultured. **b)** Image showing Fluo-4 labeled cardiomyocytes cluster (green) in a contracted state. **c)** Overlay image of fluorescent beads (red) and Fluo-4 labeled (green) cardiomyocytes cluster. Scale bars: 20 μm .

2.9 Image processing

2.9.1 Determination of fraction of cardiomyocytes and non-myocytes:

In order to determine the fraction of cardiomyocytes and non-myocytes in culture, cells were fixed on day 3 of culture and stained for the nucleus, myocyte-specific sarcomeric α -actinin and actin as described previously in section 2.7. To determine the fraction of myocyte and non-myocyte population in the culture, an image processing routine was established using ImageJ (v1.52n) (Schindelin et al., 2012). The channels for nucleus, sarcomere and actin filaments were separated in the first step. Following interactive intensity thresholding (default threshold algorithm of ImageJ; black and white; dark background) and background subtraction (settings: rolling ball radius of 20 px (pixel size 0.1 μm); light background; create background),

a binary mask was generated to obtain nucleus surface coverage. To separate nuclei of multiple cells that appear adjoined, watershed segmentation was used. Nuclei were counted using an interactive count in which only particles larger than $75 \mu\text{m}^2$ were counted (Fig. 2.9 a – b). Particles below this size were considered debris and therefore excluded.

CMs in the culture were identified by the selective marker sarcomeric α -actinin. To determine the count of CMs in the culture, nucleus and sarcomeric channels were merged. Following background subtraction (settings: rolling ball radius of 20 px (pixel size $0.1 \mu\text{m}$); light background; create background), binary masks of cells and nuclei were generated. A composite image of nuclei and sarcomeres was obtained. The image was converted to RGB color format and further to 8-bit format, followed by interactive intensity thresholding (default threshold algorithm of ImageJ; black and white; dark background) where the nuclei of cells lacking sarcomeres were manually excluded. Thereby only myocyte nuclei remained as seen in Fig. 2.9 c - d. A binary mask was generated to obtain nucleus surface coverage, and adjoined nuclei were separated using watershed segmentation. Nuclei were subsequently counted with an interactive count in which only particles larger than $75 \mu\text{m}^2$ were included. The non-myocyte nuclei count was determined by subtracting the number of myocyte nuclei from the total number of nuclei. For statistical analysis, the fraction of myocyte and non-myocyte cells was determined from the overview images of all cultures (individual isolates and replicates), and the mean fraction of each cell type was calculated.

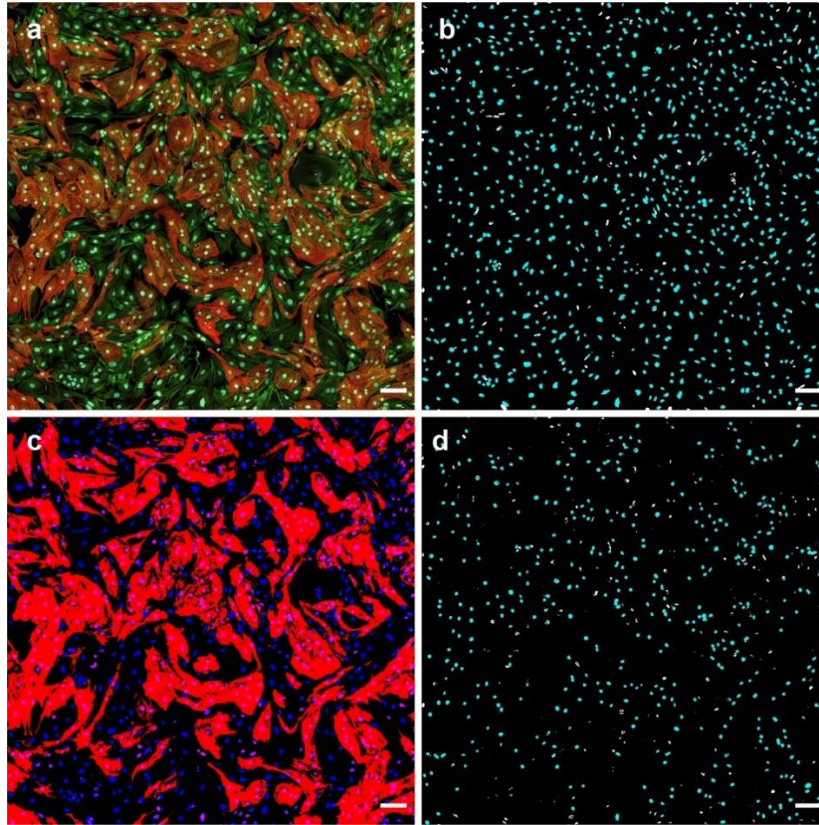


Figure 2.9: Determination of fraction of cardiomyocytes in cultures: **(a)** Tile-scan images of day 3 coculture showing cells stained for myocyte-specific α -actinin (red), Actin (green) and nuclei (blue). Cardiomyocytes containing α -actinin in sarcomeres while non-myocytes lacked sarcomeres and contained only actin filaments. Cardiomyocytes were spread across entire cultures both as single cells as well as clusters. **(b)** Nuclei mask (light blue) of all cells in the tile-scan image (a) obtained from the image processing routine described above in text. **(c)** Overlay of cardiomyocytes and nuclei masks obtained after separation of cardiomyocytes and nuclei channels from the F-actin channel. The composite image of nuclei (blue) and cardiomyocytes (red) area masks show resulting cardiomyocytes nuclei in magenta while nuclei of remaining cells are in blue. The difference in color intensities of cardiomyocyte and remaining cell nuclei enabled the determination of the number of cardiomyocytes. **(d)** Image showing the mask of cardiomyocytes nuclei (light blue) obtained from the image processing routine described above in text. Scale bars: 100 μ m.

2.9.2 Analysis of intracellular Ca^{2+} changes in cells

Ablation of cells induced specific Ca^{2+} signals in their neighborhood. These consist of a propagating Ca^{2+} wave and, for cardiomyocytes, a temporary interruption of regular beating. To quantify these changes, algorithms were implemented in Matlab (R2017; developed by Georg Dreissen (Institute of Biological Information processing, IBI-2: Mechanobiology, Forschungszentrum Jülich) as described in (Sridhar et al., 2020), to determine the position-dependent fluorescence intensity of the Ca^{2+} indicator Fluo-4 AM. Based on these curves, the

propagation speed of the slow Ca^{2+} wave induced by ablation and, for cardiomyocytes, how long it took until these cells resumed beating was determined.

- a) **Determination of intensities from Ca^{2+} imaging movies:** In the first step, the ablation time-point and ablated spot were marked manually. Ablation of the target cell was confirmed from the instant loss of Ca^{2+} indicator intensity following laser irradiation. Around the ablation point, concentric rings of 20 μm width were generated as shown in Fig. 2.10 a. At each time-point average intensities of all rings were calculated. For movies in which Ca^{2+} changes over a manually defined area had to be measured instead of concentric rings, another in-house built Matlab routine was used. Here, Ca^{2+} intensity (grey value)-changes over time were determined for the marked area. In case of multiple areas marked in a single movie, uniquely labeled/numbered intensity masks for each area were provided by the program.

- b) **Determination of Ca^{2+} propagation speed along myocardial cells:** For each analysis ring, the time point of maximum intensity was determined by a routine described below, and the speed was calculated as a ratio of the distance of the ring from the ablated cell to the time-delay between ablation and maximum fluorescence intensity in the ring. While this could be done directly on the measured curves for non-myocytes, the rapid transients of beating cardiomyocytes necessitated a further processing step to extract the much slower signal of the calcium wave (Fig. 2.10 b). To this end, an algorithm proposed by Eilers and Boelens (P. H. Eilers & Boelens, 2005) was used. It consists of a Whittaker smoother of second-order (with penalty factor λ set to 10) (P. H. C. Eilers, 2003) combined with asymmetric least square fitting (with asymmetry parameter Φ set to 0.015) (Boelens, Eilers, & Hankemeier, 2005). This algorithm produced a faithful representation of the slowly varying signal while short calcium spikes were effectively suppressed. The ablation-induced $[\text{Ca}^{2+}]_i$ -increase could be found in analysis rings at various distances from the ablated cells. However, only CMs in closely connected rings exhibited interrupted contractility while farther located CMs continued to contract. Therefore, the rings with high $[\text{Ca}^{2+}]_i$ -increase were chosen based on a threshold value. Only rings with at least two-fold $[\text{Ca}^{2+}]_i$ -increase were selected. In most experiments, CMs within five analysis rings from the ablated cells satisfied this criterion. Therefore, propagation speed along CMs was determined for a distance of 100 μm from the ablated

cell. Moreover, in some cases, signals from rings influenced by clearly unconnected cells, not a part of the ablation cluster had to be discarded.

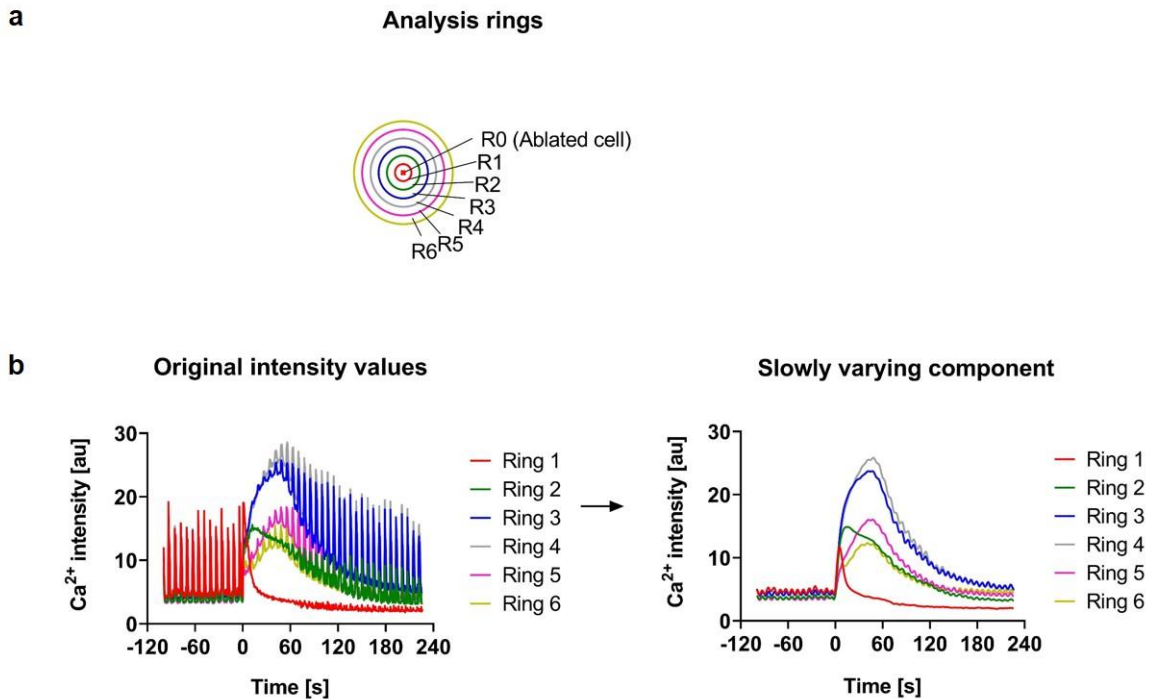


Figure 2.10: Analysis of fluorescence-intensity changes in cells over time: a) Illustration of analysis rings (R1 – R6) drawn around ablated cell as the center (R0) to study the changes in Ca^{2+} fluorescence intensity in cells of the cluster before and after ablation using the algorithm described above. Ca^{2+} intensities are represented as grey values averaged from all cells in each analysis ring for each time point. The numbering of rings starts from the central ring containing the ablated cell (shown as R1, *left*) and then successively until the last selected ring (R6). Modified from (Sridhar et al., 2020). **b)** Plot of Ca^{2+} induced fluorescence-intensity changes over the time course of ablation in a coculture of cardiomyocytes and fibroblasts (*left*, grey values) in each of the analysis rings. Rhythmic contraction of cardiomyocytes in the cluster can be seen from the periodic Ca^{2+} peaks. The corresponding slowly-varying signal component of fluorescence intensity (*right*, grey values) represents the local minima value for every intensity peak in the original intensity plots, plotted against time. The time point of ablation is set to $t = 0$ s. Modified from (Sridhar et al., 2020).

In the above-mentioned program, the values of ring width, pixel size, time-point of ablation, frame capture time and the ablation-spot are entered manually. From the time-point of ablation, the program identified the maximum fluorescence intensity (slowly varying signal intensity) after the ablation for each analysis ring and the corresponding time point at which the maximum intensity was detected. The time points of maximum intensity (red boxes) for each ring for slowly varying signal intensity plot in Fig. 2.10 b is shown as an exemplary in Fig. 2.11. Rings of uniform width are drawn around the ablated cell. The radial Ca^{2+} propagation speed was

determined as the ratio of the distance of the ring from the ablated cell (Δx) to the time delay between ablation and maximum intensity (Δt). Thereby, the radial Ca^{2+} propagation speeds ($\Delta x / \Delta t$) across all analysis rings could be determined to analyze the nature of Ca^{2+} propagation along cells surrounding the ablated cell.

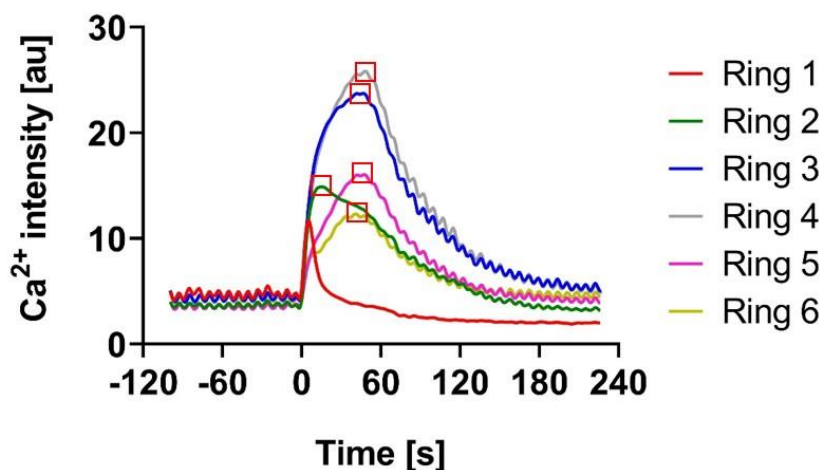


Figure 2.11: Time-point of maximum fluorescence intensity in cells: a) Plot of Ca^{2+} intensity (slowly varying signal component) in cells before and after ablation. Ring 1 contained the ablated cell, and the time-point of ablation was set to $t = 0$ s. The Time-point of maximum fluorescence intensity after ablation (red boxes) is marked for each analysis ring (red square, R2 – R6) using the image processing routine described above. Modified from (Sridhar et al., 2020).

- c) **Determination of the quiescent period for the calculation of contractile-recovery in cardiomyocytes:** Ablation-induced $[\text{Ca}^{2+}]$ -increase in surrounding CMs affected contractility and thereby, distinct Ca^{2+} peaks could no longer be found. Since CMs resumed beating gradually over time after ablation, an algorithm was developed to determine the period during which the residual beat intensities remained below 50% of the pre-ablation period. Although contractility recovered with time, the newly established contractile peaks varied in amplitude. Thereby the amplitudes before and after ablation were compared to determine the recovery of contractility in CMs after ablation. In this algorithm, the measured intensity traces were first high-pass filtered in Fourier space (hard cut-off at 0.5 Hz). Instantaneous amplitudes were determined as the difference between the highest and the lowest signal intensity in a 10 s interval centered on any given time point (Fig. 2.12 a). The resulting discontinuous signal was smoothed three times with a moving average in a centered window of width 10 s (Matlab routine movmean). In this smoothed trace, the intensity was averaged over the full pre-ablation

period, and the time interval between ablation and first signal increase above 50% of this value was taken as the quiescent period. An example of the different time periods of Ca^{2+} imaging experiments (pre-ablation, quiescent and post-half-recovery) provided by the algorithm is shown in Fig. 2.12 b for one of the analysis rings (Ring 2) selected from the original intensity plot in Fig. 2.10.

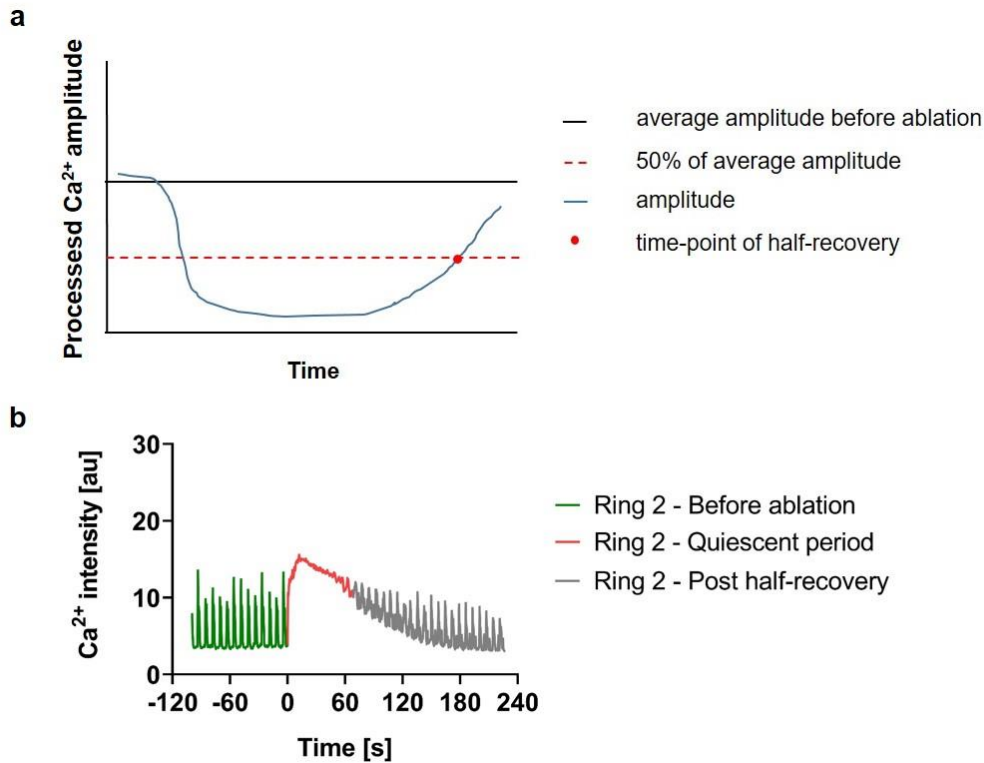


Figure 2.12: Determination of time-point of half-recovery in cardiomyocytes: **a)** Figure depicting the algorithm used to determine half-recovery in cardiomyocytes. The algorithm compares the average amplitude before ablation and amplitudes after ablation. The time-point after ablation at which the amplitude recovered to 50% of the average initial amplitude was determined as the time-point of half-recovery. **b)** Ca^{2+} changes in cells in the second analysis ring (R2) from the plots illustrated above during pre-ablation, the quiescent period following ablation, and post-half-recovery periods, indicated in different color coding, based on the half-recovery time is shown as an example of the algorithm described above. Adopted from (Sridhar et al., 2020).

d) Determination of fold-change in Ca^{2+} intensity after ablation: Fold-change in Ca^{2+} intensity in myocytes and non-myocytes following ablation was determined by comparing slowly varying Ca^{2+} signal intensities from each analysis ring before and after ablation as described in (Sridhar et al., 2020). The average Ca^{2+} intensity before ablation was calculated for each ring as a first step. Fold-change in Ca^{2+} intensity was

determined from the ratio of maximum Ca^{2+} intensity after ablation to the average intensity before ablation for each analysis ring.

- e) **Determination of $[\text{Ca}^{2+}]$ recovery times in myocytes and non-myocytes after ablation:** The recovery time or time-point at which $[\text{Ca}^{2+}]$ recovered to the initial levels before ablation was determined from the Ca^{2+} signal intensity-changes using an in-house built Python program as described in (Sridhar et al., 2020). As described in previous sections, the Ca^{2+} signal intensity increased after ablation and, upon reaching a peak value, decreased to values comparable to initial values. To detect the first time point where the signal reached the initial value again after ablation, a Python script was used. First, for each ring, the signal intensity before ablation was averaged and defined as the reference value. Then, the signal after ablation was averaged using a sliding window with a block size of 20 time points. The first time point where a block of the sliding window was below the reference value was defined as the time point of recovery.

2.9.3 Analysis of cell force changes

Analysis of traction force-changes after ablation of a single cardiomyocyte in cardiomyocyte clusters was performed using an in-house built Matlab program (Institute of Biological Information processing, IBI-2: Mechanobiology, Forschungszentrum Jülich GmbH) based on (Houben, Kirchgeßner, & Merkel, 2010; Merkel et al., 2007). As a first step, the bead image channel (Fig. 2.13 a) was separated from the remaining image channels (phase-contrast and calcium-fluorescence channels) in the time-series stack using ImageJ. Contracted and relaxed states of cardiomyocyte cluster were identified from the Ca^{2+} changes in Fluo-4 labelled cells over time (refer section 2.3). Bead displacements were determined as described in (Merkel et al., 2007). From the bead displacements, deformation field and cell forces were subsequently calculated. These calculations were based on the well understood behavior of elastic materials in response to external forces (Merkel et al., 2007). In particular, the soft crosslinked PDMS elastomer used fulfilled the prerequisites for such calculations as described in (Cesa et al., 2007; Gutierrez & Groisman, 2011). The bead image corresponding to the relaxed state of cells before ablation was taken as the reference image. A single bead was selected as the reference for bead tracking by normalized cross-correlation (cross-correlation coefficient 0.8; template size 71×71 pixel (30×30 μm); search length 2 pixel (0.8 μm) in every direction; vector displacement field (VDF) scaling of 30 (zoom factor for visualization of vectors). From the

position of beads in the reference image, bead displacements were calculated for all time points in the time-series stack to a fixed reference time-point/image. As time-series imaging of beads resulted possibly in drift, drift correction was performed by the program by following beads within manually defined areas (Fig. 2.13 b) at the corners of bead images, where the contraction had no influence and hence no deformation. Drift correction nullified imaging shift that could affect accurate determination of bead displacements.

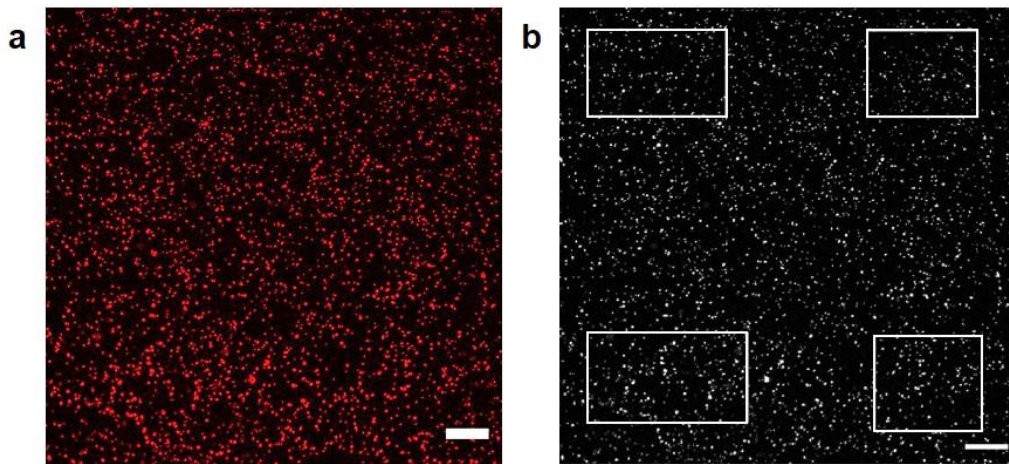


Figure 2.13: Drift correction in bead images: **a)** Image showing fluorescent beads (red) covalently coupled to elastomeric (PDMS) substrates. **b)** Image showing regions marked (rectangles) for correction of drift in bead position over time across the time-series bead images. The program described above tracks the beads in these rectangles and calculates the drift in the images. Following drift correction, the displacement of beads due to cell traction could be reliably calculated. Scale bars: 20 μm .

Force retrieval from bead displacements required an understanding of the elastic properties of the elastomers used to culture the cells. The method of estimation of the elasticity parameters - Young's modulus and the Poisson's ratio of the cross-linked PDMS elastomers were previously described in (Cesa et al., 2007). In that approach, calibration experiments were performed by applying small constant strains on PDMS elastomer cylinders and measuring the stress relaxation curve at constant strain. The axial symmetry of the cylindrical samples facilitated strain measurement. The Young's modulus of the prepared crosslinked elastomer material was determined from the viscoelastic response of the material in the calibration experiments. The Poisson's ratio (ν) - the ratio of relative transversal shrinkage to the relative longitudinal extension upon uniaxial loading, was found to be close to 0.5 for all mixing ratio (PDMS base to cross-linker) in (Cesa et al., 2007). Thereby, elastomers of stiffness 15 kPa were prepared for traction force analyses as they were nearly comparable to the stiffness of

native myocardial (Hersch et al., 2013). Following the calculation of displacement vectors for beads at each time point, the program calculated force from the input values of Young's modulus (15 kPa) and Poisson's ratio (0.5).

Force retrieval from displacement was complicated because the displacement vector field originates from the force field by a convolution of Green's tensor of an elastic half-space that decays only like the inverse of the distance (Merkel et al., 2007). The expressions for the Green's tensor of a point force acting on an elastic layer of finite thickness that is bonded to a rigid substrate was described in (Merkel et al., 2007). In this work, the Matlab program used the force field algorithm described by (Houben et al., 2010) to retrieve force distributions. In this algorithm, the whole micrograph was covered by a mesh containing almost the same number of vertices as beads were tracked, and forces were subsequently calculated at each vertex. The geometrical center of cells was determined and within the area bound by each cell, the contractile parts of all forces were added.

As multiple cells were present in cell clusters, cell outlines were drawn manually (using the corresponding calcium image as a reference) for each cell whose traction forces had to be measured. The program provided the traction forces acting on each cell area separately. Thereby, traction forces acting on each cell area were calculated for every time point in the experiment. An example of the displacement vector field (30-fold magnified) for contracted and relaxed states of a cluster of CMs can be seen in Fig. 2.14 a - b. The traction stress ($\text{nN}/\mu\text{m}^2$) exerted by the cell on to the substrate was calculated by the summation of forces acting on the marked cell area and plotted for contracted and relaxed states using a pseudo-color-coded image as shown in Fig. 2.14 c - d.

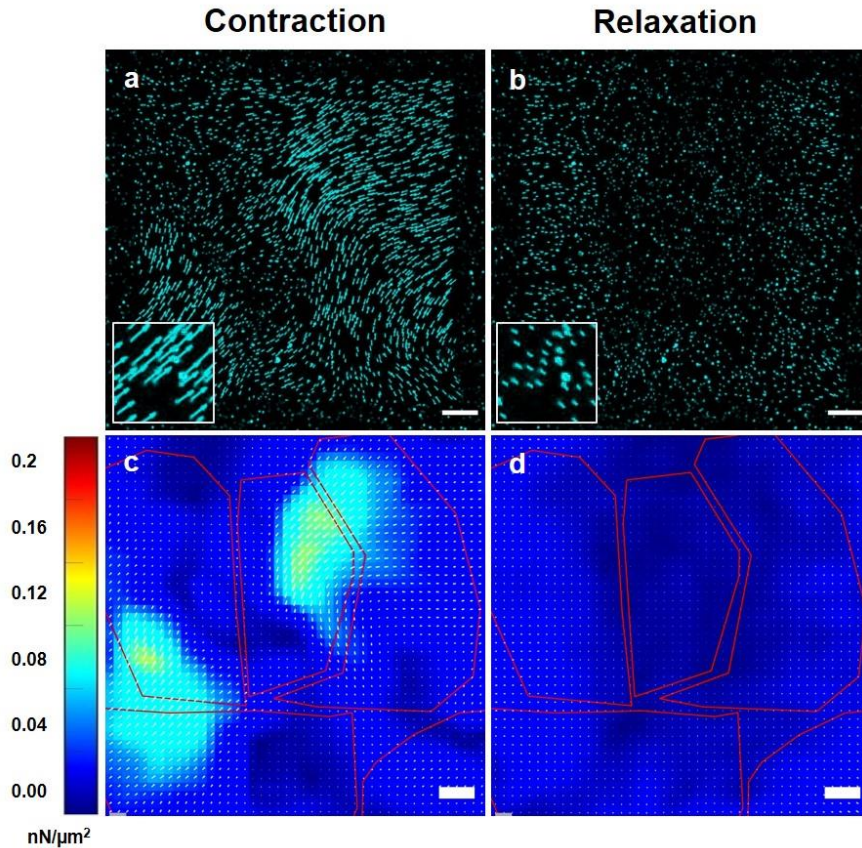


Figure 2.14: Traction stress exerted by cardiomyocytes on to the substrate: a) Vector field image showing force vectors (blue) calculated from the displacement of beads at that time point from the reference position over the cell cluster in the contracted state. **b)** Vector field image calculated over the cell cluster during the relaxed state. **c)** Overlay image of (a) with outlines (red) of cells in the cluster and is pseudo-color-coded for traction stresses at that time-point. The total sum of traction stresses was calculated as one vector per cell for each time-point. **d)** Overlay image of (b) with outlines (red) of cells in the cluster and is pseudo-color-coded for traction stresses at that time-point. The total sum of traction stresses was calculated as one vector per cell for each time-point. Reference values ($\text{nN}/\mu\text{m}^2$) corresponding to the traction stress images are shown in color coding (left). Scale bars: $20 \mu\text{m}$.

2.10 Statistical analysis

Statistical analyses were performed using GraphPad Prism version 8.4.3 for Windows (GraphPad Software, La Jolla California USA, www.graphpad.com). Multiple t-tests by Holm-Šídák method were performed to compare datasets and estimate the significance in difference between datasets. The significance levels were set to 5% ($\alpha = 0.05$) for all the analyses. P-value of < 0.05 was considered significant. The significance levels were indicated by * for $p\text{-value} \leq 0.05$, ** for ≤ 0.01 , *** for ≤ 0.001 and **** for ≤ 0.0001 .

Chapter 3 Results

3.1 Defined primary cell culture systems from embryonic rat hearts

To investigate the effects of cell death in myocardial clusters, primary cell culture was established from embryonic rat hearts. In cocultures of cardiomyocytes (CMs) and non-myocytes, CMs could be identified by the presence of sarcomeres that formed the basic contractile units of the heart muscle (Sarantitis et al., 2012) while non-myocytes lacked sarcomeres. A typical three days-old coculture of CMs and non-myocytes is shown in Fig. 3.1, with cells labeled for F-actin to visualize actin filaments (green) and CM marker α -actinin (red) to visualize sarcomeres. α -actinin was found in sarcomeres marking the z-line/z-disk (refer section 1.2.3) and co-localized with actin to bundle these filaments. Non-myocytes, on the other hand, consisted of a bundle of actin filaments called stress fibers, which are contractile filaments typically found in non-muscle cells (Pellegrin & Mellor, 2007). Once adhered to the substrate, CMs contracted rhythmically, both as single cells as well as in small clusters from day 2 in culture. From day 3, CMs contracted rhythmically and synchronously in larger clusters. Non-myocytes in culture proliferated and filled the space between CM clusters.

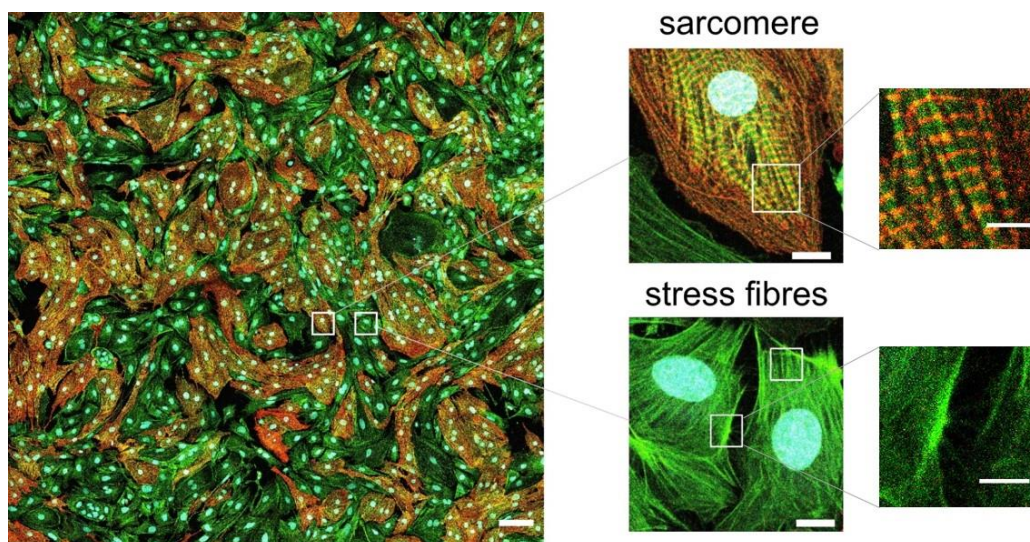


Figure 3.1: Coculture of cardiomyocytes and non-myocytes: Day three cardiac coculture cells stained for sarcomeric α -actinin (red), F-actin (green) and nucleus (light blue). Cardiomyocytes can be identified by the presence of sarcomeres (red), while non-myocytes lacked sarcomeres and contained only actin filaments. Scale bar: 100 μm . Enlarged images of cells from coculture (right) show sarcomere arrangement in cardiomyocytes with actin filaments and bands of α -actinin (top, square) and prominent stress fibers in non-myocytes (bottom, square). Scale bars: 10 μm . Further enlarged images clearly show α -actinin at z-disk co-localized with actin in cardiomyocyte and densely packed actin filaments forming stress fiber of a non-myocyte. Scale bars: 5 μm .

Due to the proliferation of non-myocytes, the non-myocyte composition increased with time and dominated at later stages of the culture (Fig. 3.2 a). Previous studies on cardiac cell composition had clearly shown that, in early neonatal rats, fibroblasts (Fbs) were the most dominant non-myocyte cell population in the heart, followed by endothelial cells (ECs) (refer section 1.1.1). ECs were also present in these cultures in addition to CMs and Fbs. However, clusters of ECs were mostly found in cultures older than one week and could be identified by their morphology (M. Nishida et al., 1993), as seen in Fig. 3.2 b. As non-myocytes such as Fbs and ECs proliferate over time in cultures, they could outgrow CMs and hinder experimental analysis of CMs. Moreover, the presence of ECs was undesirable for further analysis and had to be restricted to an as minimal fraction as possible. Therefore, cultures that were not older than seven days were used for functional analyses in subsequent experiments. For the reasons mentioned above, non-myocytes were referred to as Fbs in this work.

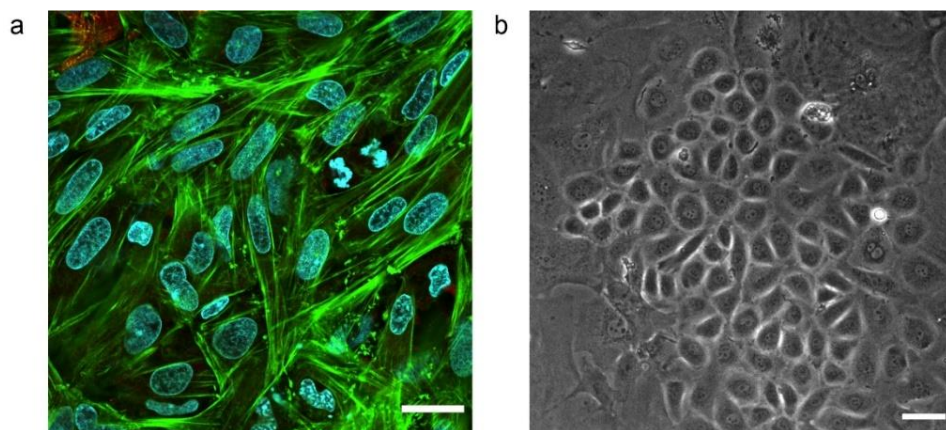


Figure 3.2: Non-myocytes in older myocardial cultures: **a)** Immunocytochemical labeling of a cell cluster from cardiac culture overgrown by fibroblasts after one week in culture. Cells were labeled F-actin (green), nucleus (light green) and sarcomeric α -actinin (red). Fibroblasts lacked sarcomeric α -actinin and contained only actin filaments. Scale bar: 10 μm . **b)** Phase-contrast image showing endothelial cells in myocardial cell cultures older than seven days. Scale bar: 50 μm .

To characterize the effects of cell death on clusters of myocardial cells with a defined composition of CMs and non-myocytes (quantification described later), isolated cells were separated by a fusion-based magnetic separation procedure as described in section 2.2.3. Following fusion-based cell separation, CMs and non-myocytes were cultured separately. Thereby, three different cell culture systems were obtained, namely the coculture, myocytes-enriched culture and myocytes-depleted culture system (Sridhar et al., 2020). To determine the

cell composition of each culture quantitatively, cells were fixed on day three and immunolabelled for α -actinin and F-actin. The difference in cell composition in each culture system can be seen from stitched tile images of immunolabelled cultures shown in Fig. 3.3. The dark stripes found in the stitched tile images could be artifacts from the stitching of tile images. In coculture systems, the fraction of non-myocytes in the total cell population was higher than the fraction of CMs. CMs were found as single cells as well as in clusters in these cultures and were surrounded by Fbs. Myocytes-enriched cultures consisted of a high proportion of CMs that formed monolayers and contracted synchronously. A small fraction of non-myocytes was still found between CM clusters in these cultures. However, the CM fraction in enriched cultures was still higher than that found in cocultures. Myocytes-depleted cultures consisted of a high proportion of Fbs and formed monolayers as they proliferated over time. Clusters of spontaneously contracting CMs were often found in smaller fractions in these cultures.

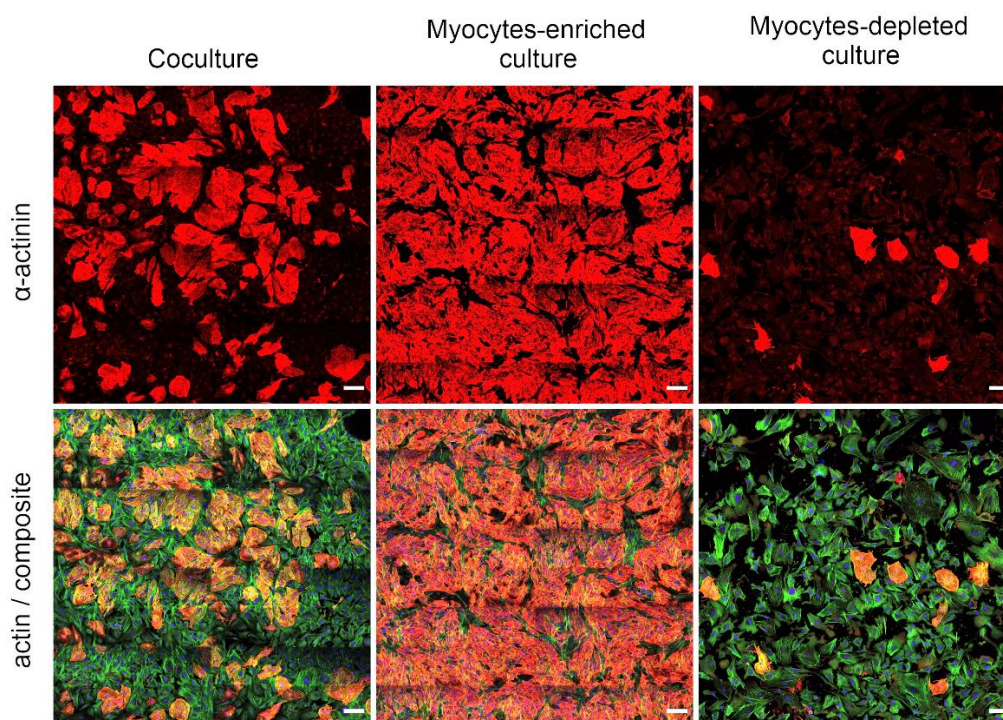


Figure 3.3: Cell composition of different cell culture systems: Overview tile-scan images of cardiac cultures obtained before and after cell enrichment using fusogenic liposomes. Cells were stained for sarcomeric α -actinin (red) and F-actin (green) to distinguish cardiomyocytes from non-myocytes in culture. α -actinin stained cardiomyocytes in each culture system i.e., coculture, myocytes-enriched culture and myocytes-depleted cultures, are shown (top row) with corresponding overlay images showing α -actinin, nuclei (blue) and F-actin (bottom row). Non-myocytes formed a marginally larger fraction of the cell population than cardiomyocytes in cocultures. In myocytes-enriched culture, cardiomyocytes formed a predominant fraction of the cell population while non-myocytes were predominant in myocytes-depleted cultures. Adopted from (Sridhar et al., 2020). Scale bars: 100 μ m.

Cell fraction in each cell culture system was determined quantitatively using the image processing routine described in section 2.9.1. The number of cardiomyocytes and non-myocytes was determined for the three culture systems. Fig. 3.4 shows the fraction of CMs and non-myocytes in each culture system on day 3 of culture. The fractions of CMs and non-myocyte population in each cell culture system were found to be as follows: coculture – 41% myocytes, 59% non-myocytes (N=4, n=14; s.d. 16%); myocytes-enriched culture – 64% myocytes, 36% non-myocytes (N=4, n=10; s.d. 15%); myocyte-depleted culture – 32% myocytes, 68% non-myocytes (N=4, n=11; s.d. 4%). The values represent the mean fraction of CMs and non-myocytes analyzed from the overview culture images of each culture system from individual isolates (N) and replicates (n).

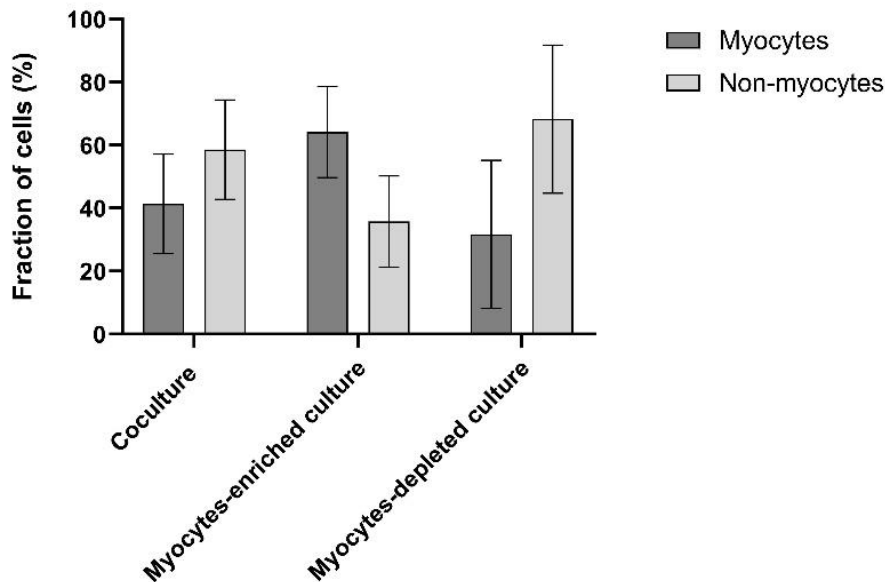


Figure 3.4: Fraction of cardiomyocytes and non-myocytes in different cell culture systems: Plot showing the mean fraction of cardiomyocytes and non-myocytes in cocultures, myocytes-enriched cultures and myocytes-depleted cultures with standard deviation (s.d.), N=4. In cocultures, the fraction of fibroblast population was higher than that of the cardiomyocytes. Cardiomyocyte fraction was highest in the myocytes-enriched culture system and fibroblast fraction was highest in myocytes-depleted culture system suggesting that the cell separation procedure enabled enrichment of specific cell type in these culture systems.

3.2 Ca²⁺-based analysis of cell activity in cultured myocardial cells

3.2.1 Ca²⁺ waves in myocardial cells

The activity of cultured myocardial cells was studied by following intracellular Ca²⁺ concentration ([Ca²⁺]_i)-changes over time. Since Ca²⁺ is essential for CM contraction, [Ca²⁺]_i

changes were recorded and analyzed to describe CM contractility over time. Spatial and temporal changes in $[Ca^{2+}]_i$ were analyzed from Ca^{2+} -induced fluorescence intensity-measurements in cells labeled with Fluo-4 Ca^{2+} indicator. Rhythmic Ca^{2+} sparks were observed in individual CMs, indicating spontaneous contractions. Synchronized Ca^{2+} sparks (Ca^{2+} waves) were observed in clusters of contracting CMs from day three (Fig. 3.5 and supplementary movie 1). These Ca^{2+} waves propagated across CMs in clusters at regular intervals and suggested a synchronous and rhythmic contraction in connected cells. In cocultures, spontaneous rhythmic Ca^{2+} waves could be seen in CMs but not in Fbs. In Fbs, intracellular $[Ca^{2+}]_i$ and Ca^{2+} oscillations were minimal compared to those in CMs (described in detail in the following sections). Thereby, upon Fluo-4 labeling, contracting CMs could be distinguished from Fbs in culture based on Ca^{2+} activity.

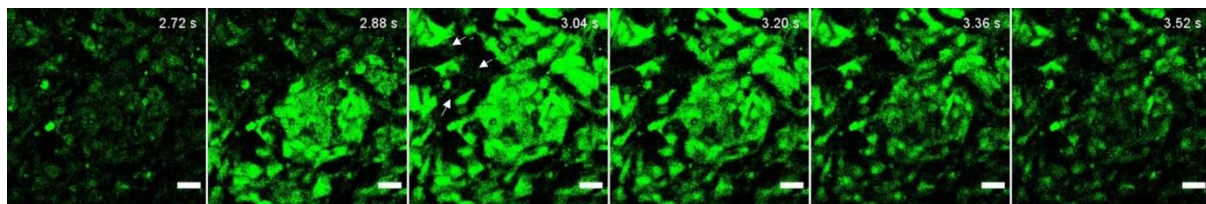


Figure 3.5: Spontaneous Ca^{2+} waves in coculture cardiomyocytes: Time series depicting spontaneous Ca^{2+} waves in contracting Fluo-4 labeled (green) cardiomyocytes in day 3 coculture. Rhythmic contractions marked by periodic Ca^{2+} waves were observed in cardiomyocytes while being absent in fibroblasts (marked by arrows; refer supplementary movie 1). Modified from (Sridhar et al., 2020). Scale bars: 50 μ m.

3.2.2 Characterization of spontaneous Ca^{2+} waves in myocardial cells

$[Ca^{2+}]_i$ -changes in myocardial cells were quantitatively analyzed using the Matlab routine described in section 2.9.2. $[Ca^{2+}]_i$ -changes in cells were studied following fluorescence intensity of Fluo-4 indicator. Fluorescence intensity of Fluo-4 indicator upon binding of Ca^{2+} (or simply referred to as Ca^{2+} intensity in this work) was represented as grey values averaged from all cells in each analysis ring (uniform width of 20 μ m) for every time point. Greyscale images corresponding to fluorescence images in Fig. 3.5 is shown in Fig. 3.6 a. The contracted and relaxed states of cells can be seen from the grey values in each analysis ring, starting from a randomly chosen CM (red) in the center. Plotting the fluorescence intensity-changes in coculture cells over time for each analysis ring (R1 – R6) showed Ca^{2+} intensity peaks from individual contractions as seen in Fig. 3.6 b, N = 10, n = 11. Since $[Ca^{2+}]_i$ changes were

represented as average intensity values from all cells of the analysis ring, the amplitude of intensity peaks was dependent on the number of cells, the type of cells (CMs/Fbs) in the analysis ring and uptake of the dye by each cell. Thereby, a small variation in amplitude of Ca^{2+} intensity peaks could be observed in the different analysis rings. However, the identical time interval between successive Ca^{2+} peaks i.e., frequency of Ca^{2+} peaks in all analysis rings as seen in Fig. 3.6 b confirmed the synchronization of contractility in cells in the cluster.

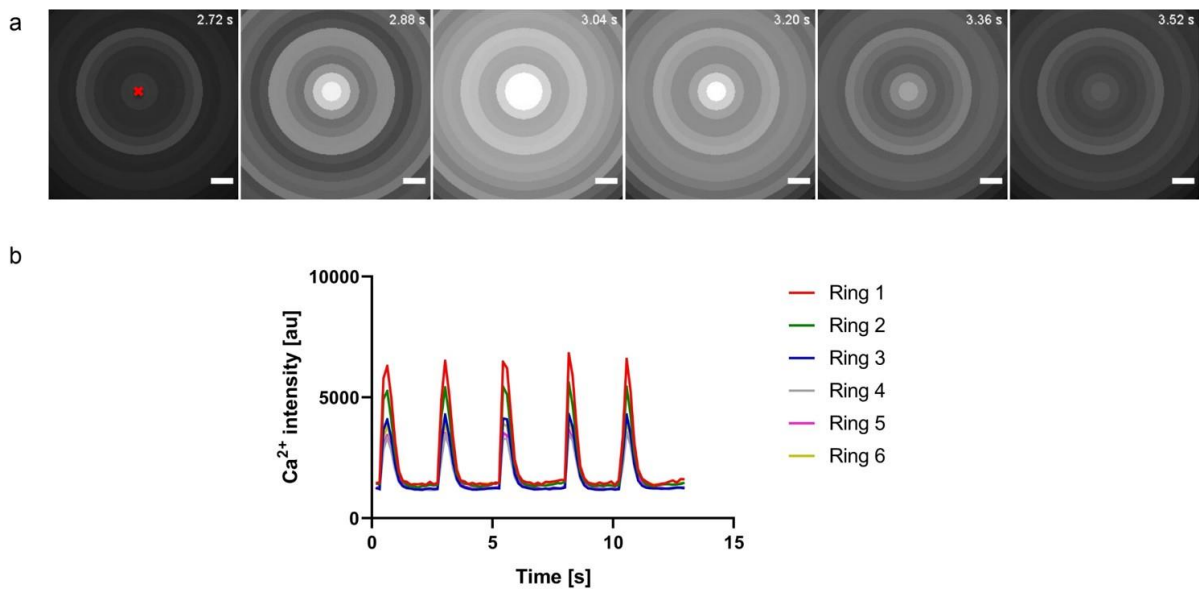


Figure 3.6: Ca^{2+} intensity-changes in coculture cells: **a)** Time-series images showing Ca^{2+} -induced fluorescence intensity-changes in coculture cells represented as grey values averaged over each analysis ring ($20\ \mu\text{m}$ width) starting from a central contracting cardiomyocyte (red). The contracted state can be seen from the high intensity values in the rings, while a low-intensity represented a relaxed state. Modified from (Sridhar et al., 2020). Scale bars: $50\ \mu\text{m}$. **b)** Plot of fluorescence intensity-changes with time in coculture cells showing Ca^{2+} intensity peaks representing contractions of cardiomyocytes in each analysis ring, $N = 10$. Modified from (Sridhar et al., 2020)

In order to characterize the $[\text{Ca}^{2+}]_i$ -changes in CMs and Fbs after cell enrichment, Ca^{2+} -induced fluorescence intensity was analyzed in myocytes-enriched and myocytes-depleted cultures. Plotting Ca^{2+} intensity-changes (as grey values) over time in myocytes-enriched cultures showed Ca^{2+} peaks at regular intervals in all analysis rings similar to those found in cocultures. The contractile frequency was identical in cells from all analysis rings (Ring 1 – 6) as seen in Fig. 3.7 a (supplementary movie 2), $N=5$, $n=7$, indicating synchronized contractility in these cells. Although the myocytes-depleted cultures sometimes consisted of myocytes, myocyte-free clusters could be found in the cultures. Ca^{2+} intensity-analysis in manually chosen clusters

of myocytes-depleted cultures showed a lack of distinct Ca^{2+} intensity peaks, unlike coculture and myocytes-enriched culture cells, indicating the absence of CMs in these clusters (Fig. 3.7 b and supplementary movie 3) for $N = 4$, $n = 6$. Although Ca^{2+} intensity oscillations were observed in these cells, they were minimal in comparison to the Ca^{2+} intensity-changes in contractile CMs. Ca^{2+} intensities were different across each analysis ring, which could be explained by a possible variation in the number of cells in analysis rings or uptake of dye by the cells in different rings. Ca^{2+} intensity analysis thereby clearly showed the dynamic $[\text{Ca}^{2+}]_i$ –changes in cells from all three culture systems. Further, it also indicated the quality of cell enrichment in each culture system, and the CMs functionality was not affected by the cell-separation procedure.

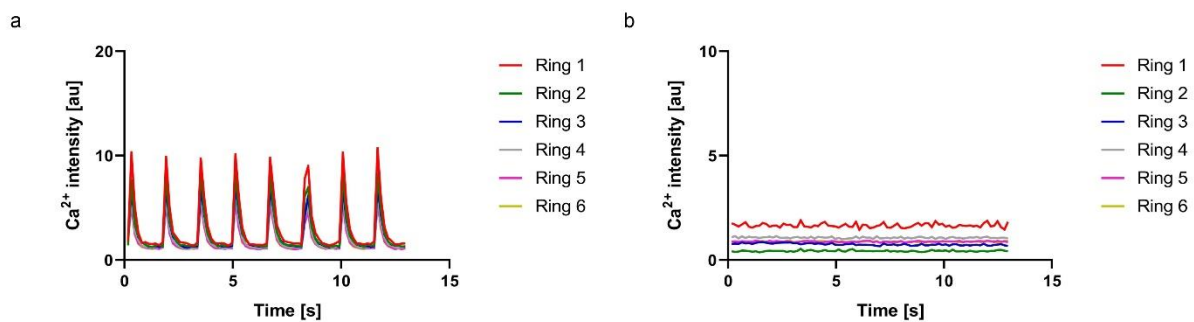


Figure 3.7: Ca^{2+} intensity-changes in myocytes-enriched and myocytes-depleted cultures: **a)** Plot of fluorescence intensity-changes with time showing Ca^{2+} intensity peaks in each analysis ring in myocytes-enriched cultures (refer supplementary movie 2), $N = 5$. Modified from (Sridhar et al., 2020). **b)** Plot showing Ca^{2+} -induced fluorescence intensity changes with time in myocytes-depleted culture. Fibroblasts in culture showed minimal Ca^{2+} changes over time. The presence of a large fraction of fibroblasts in these clusters can be seen from the lack of contractile Ca^{2+} peaks typically seen in cardiomyocytes (refer supplementary movie 3), $N = 4$. Modified from (Sridhar et al., 2020).

3.3 Effect of ablation of single-cells in cocultures of cardiomyocytes and fibroblasts

In order to study the effect of a single-cell death on surrounding cells of the cluster, target cells were selectively irradiated with a pulsed UV laser (3 – 5% of total laser output) for 1 – 2 s (1000 – 2000 short pulses) until the cell was killed. The effect of cell death on surrounding cells of the cluster was analyzed from the spatial and temporal $[\text{Ca}^{2+}]_i$ changes in cells before and after ablation. To study the effect of a single CM death on surrounding CMs, clusters containing numerous contracting CMs exhibiting rhythmic Ca^{2+} waves were manually chosen in cocultures. A single central CM was selectively irradiated with laser pulses to induce cell death. Laser-induced cell death was confirmed from the mechanical disruption of the target

cell (phase contrast channel in supplementary movie 4) as well as from permanent loss of Ca^{2+} intensity in the cell upon ablation as seen in fluorescence images in Fig. 3.8 and supplementary movie 4.

CM death resulted in a strong increase in $[\text{Ca}^{2+}]_i$ over time in surrounding CMs (Sridhar et al., 2020), as seen from the time series fluorescence images. Ablation-induced Ca^{2+} increase was higher in cells close to the ablated cell compared to the cells located farther. Increased $[\text{Ca}^{2+}]_i$ in surrounding CMs upon ablation was followed by a briefly interrupted contractility. However, CMs located far from the ablated cell, with relatively minimal increase in $[\text{Ca}^{2+}]_i$, continued to contract without interruption. This suggested a distance-dependent effect of single-cell death on the cluster upon ablation. With time, $[\text{Ca}^{2+}]_i$ in affected cells decreased, starting from the distantly located affected CMs towards the point of ablation as seen from the 50 s and 100 s fluorescence images. With decreasing $[\text{Ca}^{2+}]_i$, a renewed contractility was detected as seen from the reappearance of contraction in cells (105 s). Further, an increased $[\text{Ca}^{2+}]_i$ could be seen in both relaxed and contracted states (greyscale images in Fig. 3.8), suggesting an increase in basal $[\text{Ca}^{2+}]_i$ following ablation, especially in cells in the highly affected region (marked by a dotted circle). This was confirmed from the greyscale images. In post-ablation contractions (5 s, 55 s, 105 s), $[\text{Ca}^{2+}]_i$ levels was higher compared to the levels at the contracted state before ablation (-7 s). Similarly, elevated $[\text{Ca}^{2+}]_i$ levels can be seen only for inner rings from relaxed states after ablation (50 s, 100 s) when compared to the levels before ablation.

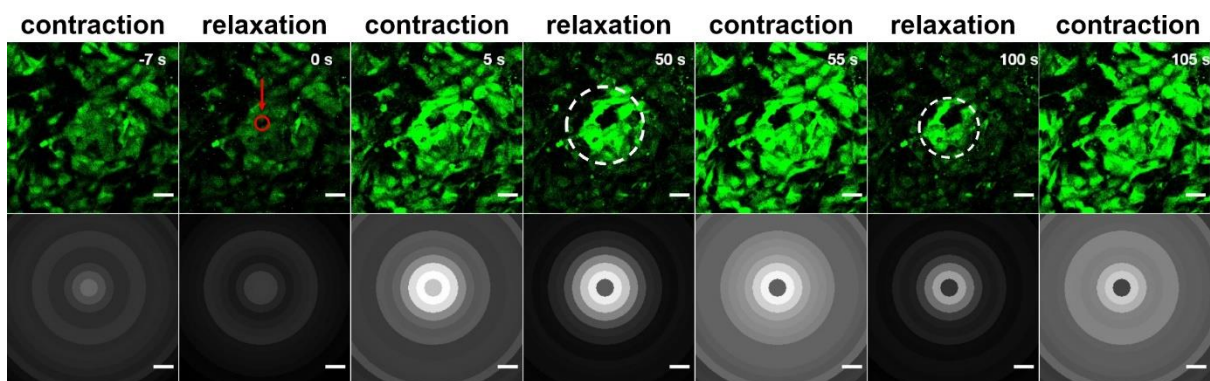


Figure 3.8: Laser-induced cardiomyocyte death resulted in a temporal intracellular calcium-increase in surrounding cardiomyocytes: Time-series images showing calcium waves in fluorescently labeled contracting cardiomyocytes (green) representing contracted and relaxed states, before and after ablation, with the ablated cell (red) in the central ring. Ablation resulted in increased $[\text{Ca}^{2+}]_i$ in surrounding cells with time (refer supplementary movie 4). The Time-point of ablation is set to $t = 0$ s. Corresponding grey-scale images show average grey values over each of the concentric rings (Ring 1 - 6) for that time point. The dashed ring at time point 50 s and 100 s indicates the decreasing affected area for high $[\text{Ca}^{2+}]_i$ over time. Adopted from (Sridhar et al., 2020). Scale bars: 50 μm .

Analysis of Ca^{2+} intensity-changes in cells over time confirmed the effect of ablation-induced single CM death on surrounding CMs. Plotting Ca^{2+} intensity in cells in each analysis ring (as F/F_0 ratio, where F is the fluorescence intensity at any given time point and F_0 is the average fluorescence intensity before ablation) with time showed rhythmic Ca^{2+} peaks in CMs before ablation. Ca^{2+} intensity-changes over time observed in Fig. 3.8 is plotted in Fig. 3.9 a. Ablation of single CM was marked by a permanent loss of Ca^{2+} intensity as seen in Ring 1. The time-point of ablation was set to $t = 0$ s. Following ablation-induced death of a CM, a sharp increase in Ca^{2+} intensity was observed in surrounding CMs (Ring 2 – 6) with time. Loss of rhythmic contractility for enhanced $[\text{Ca}^{2+}]_i$ in CMs was observed from the lack of distinct Ca^{2+} peaks briefly after ablation. However, Ca^{2+} intensity decreased to values identical to those before ablation with time, indicating decreasing $[\text{Ca}^{2+}]_i$ with time.

Moreover, a gradual recovery of contractility was observed in the affected cells, as seen from the renewed detection of Ca^{2+} intensity peaks in Fig. 3.9 a, that went along with a decrease in $[\text{Ca}^{2+}]_i$ over time. The farther the rings, the less affected they were with Ca^{2+} inflow and renewed contractility appeared earlier compared to the rings closer to the ablated cell. Further, analysis of maximum Ca^{2+} intensity ($[\text{Ca}^{2+}]_{\text{max}}$) following ablation in each of the analysis rings indicated that the time point of maximum $[\text{Ca}^{2+}]_i$ was (t_{Fmax}) delayed in successive analysis rings (shown in inlay in Fig. 3.9 b). The time-delay in $[\text{Ca}^{2+}]_i$ -increase in CMs in successive analysis rings indicated a flow of Ca^{2+} (Ca^{2+} propagation) from the immediately located CMs to the connected CMs over time, $N = 8$, $n = 10$.

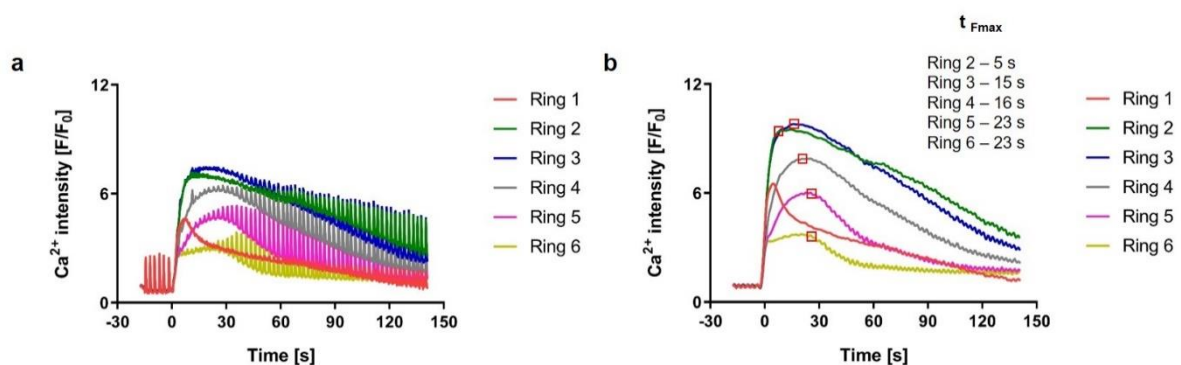


Figure 3.9: Ablation-induced Ca^{2+} intensity-changes in coculture cardiomyocytes: **a)** Plot of Ca^{2+} fluorescence intensity-changes (original intensity) with time in cocultures corresponding to Fig. 3.8. Ablation of single cardiomyocyte (Ring 1) resulted in increased Ca^{2+} intensity over time in surrounding rings. Modified from (Sridhar et al., 2020). **b)** Plot showing relative Ca^{2+} fluorescence-intensity (i.e. the slowly varying component of fluorescence signals averaged over each ring) with time, indicating $[\text{Ca}^{2+}]_i$ of cells before and after ablation, $N = 8$. The time-points of maximum fluorescence intensity (t_{Fmax}) for each of the analysis rings is shown within the plot. Modified from (Sridhar et al., 2020).

To study the effect of single-cell death particularly pronounced for Fbs in cocultures, clusters containing actively contracting CMs surrounded by numerous Fbs were manually chosen. Ablation of a single contracting CM in these clusters resulted in a rapid, transient increase in $[Ca^{2+}]_i$ of surrounding Fbs, as shown in Fig. 3.10 and supplementary movie 5 (Sridhar et al., 2020). The $[Ca^{2+}]_i$ -spike spread radially like a solitary wavefront through the surrounding Fbs starting from the ablated cell. This Ca^{2+} spike formation was induced irrespective of whether CMs or Fbs were ablated in the cluster. $[Ca^{2+}]_i$ decreased to initial values within a short period of time (< 50 s) as seen from the greyscale images before and after ablation in Fig. 3.10.

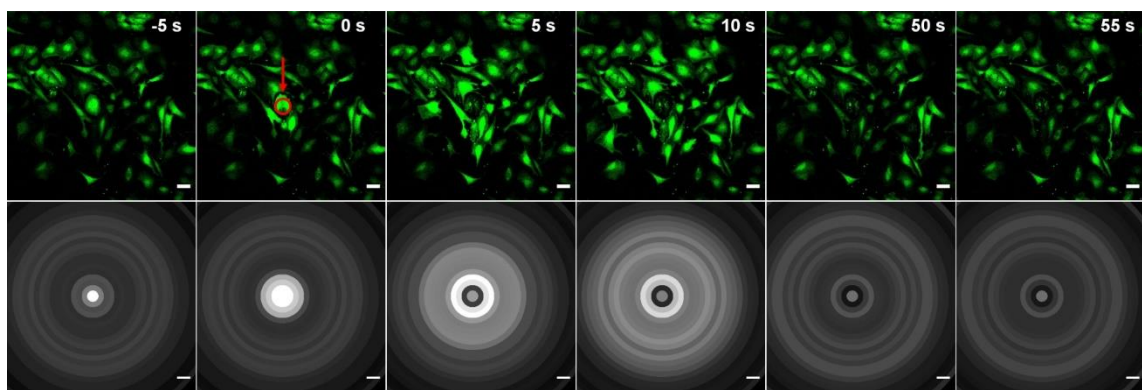


Figure 3.10: Impact of ablation-induced cell death on fibroblasts in cocultures: Time-series images (green) showing propagation of a rapid, transient wave of Ca^{2+} along the cells after ablation of a central cardiomyocyte (red, refer supplementary movie 5). Corresponding grey-scale images show grey values averaged over each of the concentric rings at that time point. The Time-point of ablation is set to $t = 0$ s. Adopted from (Sridhar et al., 2020). Scale bars: $50 \mu\text{m}$.

To analyze the changes in $[Ca^{2+}]_i$ after ablation, Ca^{2+} intensities from Fig. 3.10 were plotted with time. Plotting Ca^{2+} intensity-changes over time confirmed the formation of a single spike in $[Ca^{2+}]_i$ in surrounding Fbs upon ablation of a single central CM (Fig. 3.11 a, b). CM death can be seen from the loss of contractility and a permanent drop in Ca^{2+} intensity (Ring 1) after ablation. The time point of ablation was set to $t = 0$ s. Interestingly, the spike in $[Ca^{2+}]_i$ was transient as the $[Ca^{2+}]_i$ dropped to values before ablation within 60 s post ablation. Moreover, the magnitude of ablation-induced $[Ca^{2+}]_i$ -increase was nearly comparable in all the rings. The time-delay in $[Ca^{2+}]_i$ -spike formation (shown in the inlay in Fig. 3.11 b) in successive rings (shown in inlay in Fig. 3.11 b) was found to be marginal, which indicated a rapid propagation of Ca^{2+} along Fbs. Therefore, analysis of laser-induced single CM death in cocultures resulted in a distance-dependent, briefly sustained $[Ca^{2+}]_i$ -increase and a briefly interrupted contractility

in surrounding CMs and a rapid, transient $[Ca^{2+}]_i$ -spike of comparable magnitude in surrounding Fbs, $N = 9$.

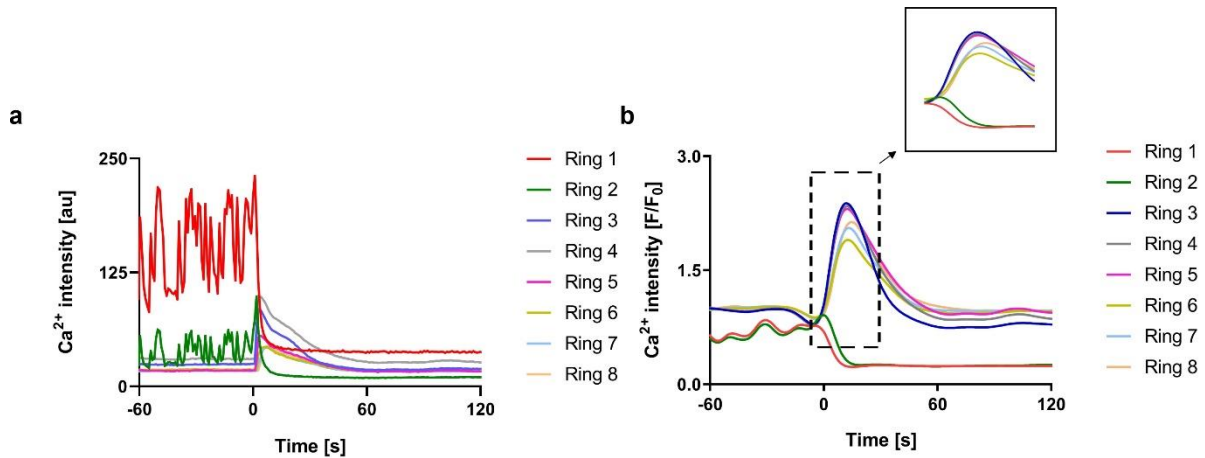


Figure 3.11: Ablation-induced Ca^{2+} intensity-changes in coculture fibroblasts: **a)** Plot depicting changes in Ca^{2+} fluorescence intensity (original intensity values) with time (corresponding to Fig. 3.10), indicating averaged $[Ca^{2+}]_i$ of rings (Ring 1-8) before and after ablation. Ablation of a central contracting cardiomyocyte (Ring 1 and 2) resulted in a momentary spike in $[Ca^{2+}]_i$ of surrounding fibroblasts in the cluster. Ca^{2+} intensity values returned to initial levels within a short period of time post ablation. **b)** Plot depicting relative Ca^{2+} fluorescence intensity with time, indicating $[Ca^{2+}]_i$ of cells (from Ring 1-8) before and after ablation, $N = 9$. The inlay shows a zoom-in of the single Ca^{2+} spike moving through the successive rings. Adopted from (Sridhar et al., 2020).

3.3.1 Analysis of ablation-induced Ca^{2+} propagation speed in cardiomyocytes and fibroblasts

Ca^{2+} intensity analysis clearly indicated a propagation of Ca^{2+} along CMs and Fbs upon single cell-ablation in coculture clusters. In order to analyze the speed at which Ca^{2+} propagated along the surrounding cells in the cluster, the intensity values were plotted against time to determine the time point at which maximum intensity (t_{max}) was detected in each of the analysis rings (explained in detail in section 2.9.2). To check for the difference in Ca^{2+} propagation in CMs and Fbs in cocultures, radial Ca^{2+} propagation speed was calculated from ablation experiments pronounced for CMs and Fbs separately. Since the renewed contractility of CMs hindered the accurate determination of the time point of maximum intensity as described in section 2.9.2, propagation speed was determined from slowly varying component of Ca^{2+} signal intensity in CMs. In Fbs, propagation speed was determined based on original intensity values.

Ablation-induced Ca^{2+} propagation speed was plotted across each analysis ring (Fig. 3.12) to understand the propagation behavior in CMs and Fbs with distance. As cells in farther rings were unaffected by ablation and continued to contract (seen from continual Ca^{2+} waves after ablation), only the rings most affected by ablation, having a threshold value of a two-fold increase in $[\text{Ca}^{2+}]_i$, were chosen for propagation speed analysis along CMs. Thereby, only the cells within 100 μm from the ablated cell, which were above the threshold value, could be selected in coculture clusters. Plot of radial Ca^{2+} propagation speed with distance clearly showed the difference in Ca^{2+} propagation along CMs and Fbs in cocultures (Fig. 3.12). The radial Ca^{2+} propagation speed in CMs ranged from 7 $\mu\text{m/s}$ (s.e.m. 2 $\mu\text{m/s}$) to 4 $\mu\text{m/s}$ (s.e.m. 0.7 $\mu\text{m/s}$) for $N = 10$ (where N refers to individual isolates; sample size including replicates, $n = 15$). In Fbs, the speeds were in the about 20 $\mu\text{m/s}$ for $N = 9$. Thereby, ablation-induced Ca^{2+} propagation speeds were at least three-fold higher for Fbs in most analysis rings. Comparing radial Ca^{2+} propagation speeds in CMs and Fbs in cocultures showed a significantly higher speed in Fbs for a distance of up to 100 μm from the ablated cell (Multiple t-tests, Holm-Sidak method, $\alpha = 0.05$), suggesting a possible difference in mechanisms underlying Ca^{2+} propagation in these cell types.

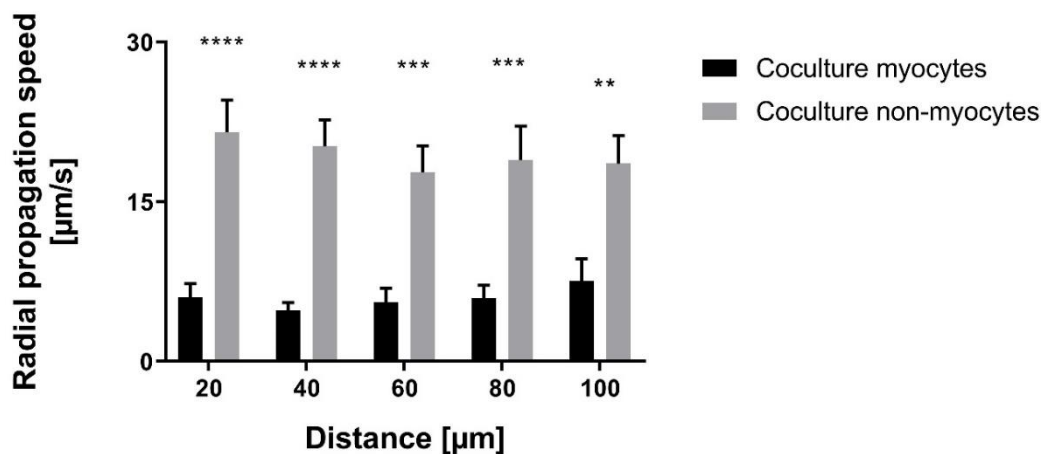


Figure 3.12: Ablation-induced radial Ca^{2+} propagation speed in coculture cardiomyocytes and fibroblasts: Plot of mean radial Ca^{2+} propagation speed along cardiomyocytes and fibroblasts with distance from the ablated cell in cocultures. Ca^{2+} propagation speed along cardiomyocytes is plotted only for the rings highly affected due to Ca^{2+} inflow (R1 – R5), $N = 10$ ($n = 15$) for myocytes and $N = 9$ ($n = 9$) for fibroblasts. Ca^{2+} propagation speed along fibroblasts is plotted along the rings R1 – R10. Error bars represent s.e.m. Ca^{2+} propagation was significantly faster in fibroblasts compared to that in cardiomyocytes (Multiple t-tests, Holm-Sidak method, $\alpha = 0.05$). The significance levels were set to 5% ($\alpha = 0.05$) for all the analyses. P-value of < 0.05 was considered significant. The significance levels were indicated by * for p-value ≤ 0.05 , ** for ≤ 0.01 , *** for ≤ 0.001 and **** for ≤ 0.0001 .

3.4 Characterization of cell-type-specific effect of ablation using separate cultures of cardiomyocytes and fibroblasts

3.4.1 Effects of single-cell death in the cardiomyocytes-enriched culture system

To investigate whether the ablation-induced effects observed in coculture cells were cell-type specific, single-cell death was analyzed in myocytes-enriched and myocytes-depleted clusters (Sridhar et al., 2020). Myocytes-enriched cultures consisted of numerous clusters of CMs contracting rhythmically and synchronously. Ablation of single CM in a cluster of CMs resulted in $[Ca^{2+}]_i$ increase in surrounding CMs with time (Fig. 3.13 and supplementary movie 6). Similar to the ablation effect in coculture CMs, a high $[Ca^{2+}]_i$ was observed in closely connected cells than in distantly located cells in the cluster. Moreover, an increased $[Ca^{2+}]_i$ was followed by a brief loss of contractility in surrounding CMs. Loss of contractility can be seen at time points 5 s, 50 s and 55 s post ablation in Fig. 3.13. Farther located cells were less affected by ablation and showed continual contractions. With time, $[Ca^{2+}]_i$ decreased in the affected cells (100 s, 105 s), and a renewed contractility was found. However, $[Ca^{2+}]_i$ in very closely connected cells to the ablated cell remained high during the experimental time-frame.

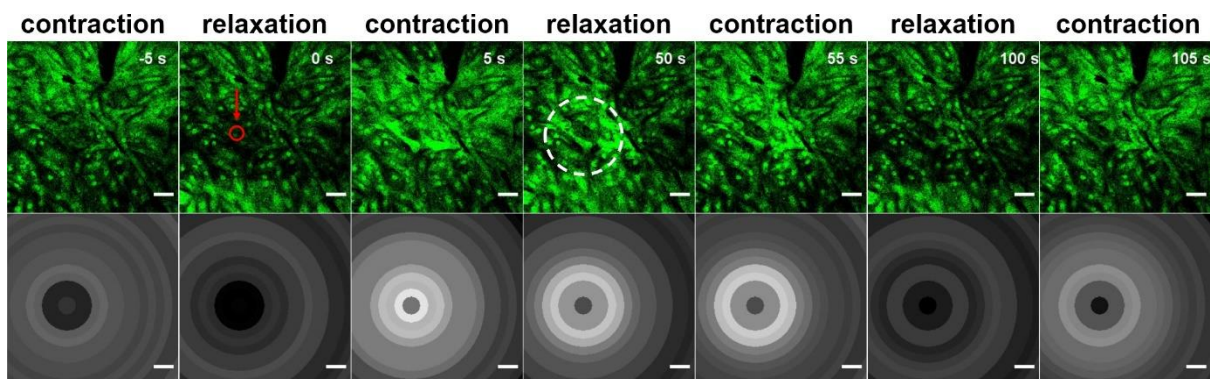


Figure 3.13 Impact of cardiomyocyte death in cardiomyocytes-enriched cultures: Time-series images (green) showing calcium waves in fluorescently labeled contracting myocytes representing contracted and relaxed states, before and after ablation (refer supplementary movie 6). The ablated cell is indicated by a red circle. Times before and after ablation ($t = 0$) are indicated. Corresponding grey-scale images show grey values averaged over each of the concentric rings at that time point. The dashed ring at time point 50 s indicates the affected area for high $[Ca^{2+}]_i$. After an additional 50 s, $[Ca^{2+}]_i$ levels returned to levels similar to those before ablation. Adopted from (Sridhar et al., 2020). Scale bars: 50 μ m.

Analysis of Ca^{2+} intensity-changes in cells over time confirmed the effects of ablation on surrounding cells. Plotting Ca^{2+} intensity values with time showed a sharp increase in Ca^{2+} intensities in the surrounding CMs (Ring 2 – 6). Similar to the observations from CMs in coculture, the increase in $[\text{Ca}^{2+}]_i$ levels was distance-dependent, as seen from the magnitude of $[\text{Ca}^{2+}]_i$ -increase post ablation. The closely located rings showed a higher $[\text{Ca}^{2+}]_i$ -increase compared to the cells located farther in the clusters. The time-delay for maximum intensity post ablation in successive rings indicated a propagation of Ca^{2+} from one cell to another from the point of ablation. Analysis of radial Ca^{2+} propagation speed with distance along CMs in myocytes-enriched cultures showed that the propagation speeds ranged from $9 \mu\text{m/s}$ (s.e.m. $3 \mu\text{m/s}$) to $4 \mu\text{m/s}$ (s.e.m. $0.9 \mu\text{m/s}$) for $N = 5$, $n = 7$. Ca^{2+} intensity returned to values before ablation in ~ 2 min post ablation as shown in Fig. 3.14. In some ablation experiments, Ca^{2+} intensity decreased below pre-ablation levels which could be explained by possible bleaching of the fluorophore over time.

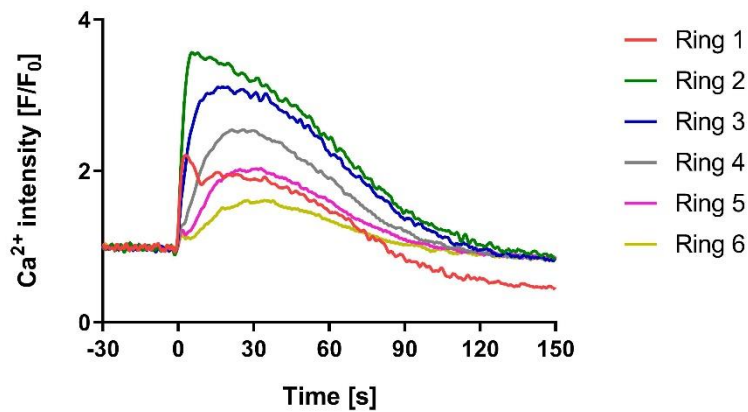


Figure 3.14: Ablation-induced Ca^{2+} intensity-changes in cardiomyocytes-enriched culture: Plot depicting changes in Ca^{2+} intensity with time (slowly varying component of fluorescence intensity) in myocytes-enriched cultures (corresponding to Fig. 3.13) before and after ablation ($t = 0$ s). Ablation resulted in a sustained increase in $[\text{Ca}^{2+}]_i$ in surrounding myocytes and was accompanied by a brief interruption in the contractility (refer supplementary movie 6). Ca^{2+} intensity values returned to values similar to pre-ablation values with time and contractility recovered with decreasing $[\text{Ca}^{2+}]_i$ over time, $N = 5$. Modified from (Sridhar et al., 2020).

3.4.2 Effects of single-cell death in the cardiomyocytes-depleted culture system

To understand whether the effects of ablation observed in fibroblasts in cocultures was also cell-type specific, single-cell death was analyzed in myocytes-depleted cultures

(Sridhar et al., 2020). Although myocytes-depleted cultures predominantly contained non-myocytes, CMs were found to some extent (refer section 3.1). Therefore, cell clusters containing very few or no myocytes were selectively chosen, as the presence of myocytes could interfere with the analysis of ablation effects in non-myocytes. Ablation of a single Fb in myocytes-depleted cultures resulted in a rapid $[Ca^{2+}]_i$ spike-formation in surrounding cells of the cluster (Fig. 3.15 and supplementary movie 7), similar to the observations in coculture Fbs. The $[Ca^{2+}]_i$ -spike formed upon ablation spread across the cluster like a solitary wavefront propagating along the Fbs starting from the ablated cell. $[Ca^{2+}]_i$ decreased to initial values before ablation within a short period of time (~ 45 s) as seen from the grey-scale images in Fig. 3.15.

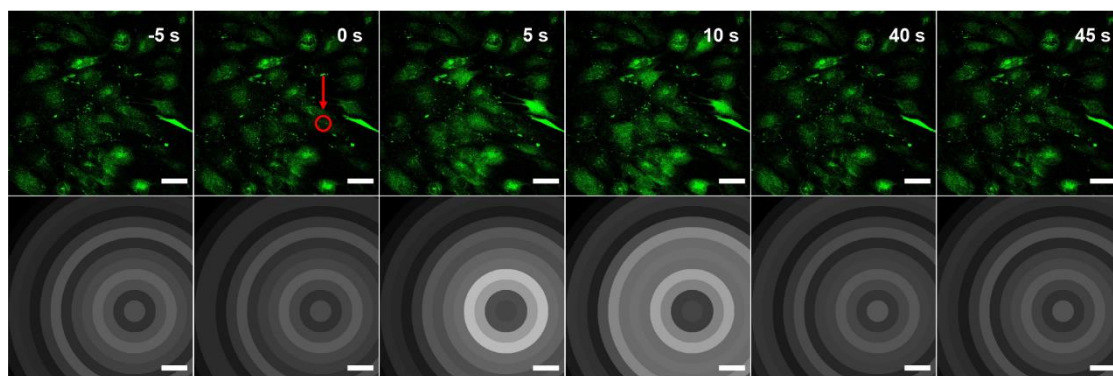


Figure 3.15: Ablation of fibroblasts in myocytes-depleted cultures: Time-series images (green) showing the propagation of a transient, solitary wave of Ca^{2+} along fluorescently labeled fibroblasts after single-fibroblast ablation (red, refer supplementary movie 7). Corresponding grey-scale images show grey values averaged over each of the concentric rings (Ring 1 - 8) for that time point. Adopted from (Sridhar et al., 2020). Scale bars: 50 μ m.

Plotting Ca^{2+} changes against time confirmed the formation of a transient spike in $[Ca^{2+}]_i$ upon ablation similar to those in coculture Fbs. Cell death can be seen from the loss of Ca^{2+} intensity upon ablation ($t = 0$ s) in Ring 1 in Fig. 3.16. The $[Ca^{2+}]_i$ spike was transient as $[Ca^{2+}]_i$ levels returned to initial values within 45 s post ablation. Analysis of radial Ca^{2+} propagation speeds with distance in myocytes-depleted cultures showed speeds of about 20 μ m/s for $N = 8$ ($n = 14$). The difference in the pattern on Ca^{2+} increase and Ca^{2+} propagation indicated a difference in Ca^{2+} regulation in these cell types and will be discussed in detail in the upcoming sections.

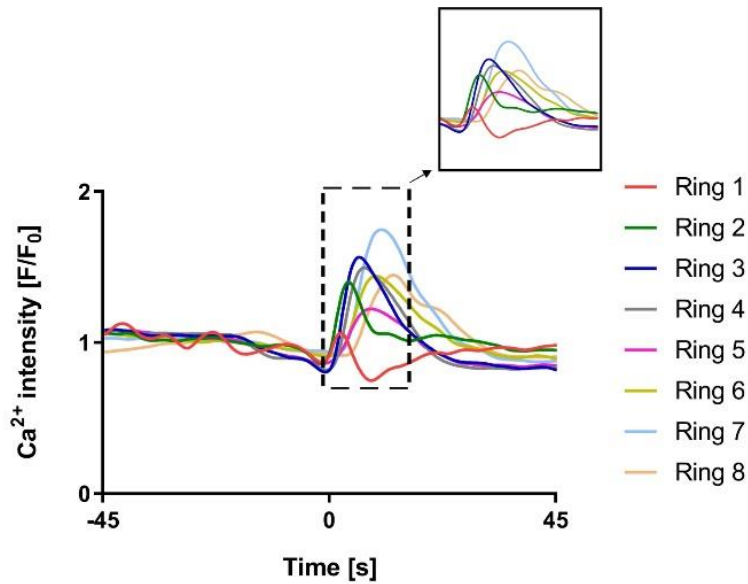


Figure 3.16: Ablation-induced Ca^{2+} intensity-changes in myocytes-depleted culture: Plot depicting changes in Ca^{2+} fluorescence intensity with time (corresponding to Fig. 3.15), indicating $[\text{Ca}^{2+}]_i$ of cells before and after ablation ($t = 0$ s). Ablation of a single fibroblast resulted in a spike in $[\text{Ca}^{2+}]_i$ in surrounding fibroblasts. Ca^{2+} intensity values returned to initial levels within a short period of time post ablation. The inlay shows a zoom-in of the Ca^{2+} spike moving sequentially along the subsequent rings (Ring 1 – 8) with the same axes in the main plot, $N = 8$. Modified from (Sridhar et al., 2020).

3.4.3 Comparison of Ca^{2+} propagation speeds along cardiomyocytes and fibroblasts across different cultures

Analysis of radial Ca^{2+} propagation speed with distance in myocytes-enriched cultures and myocytes-depleted cultures showed that the propagation speeds were similar to the speeds measured in coculture CMs and Fbs respectively. The plot of Ca^{2+} propagation speeds along CMs and Fbs from each cell culture system is shown in Fig. 3.17 a. Here, propagation speeds were calculated based on the slowly varying signal intensities for CMs and original signal intensities for Fbs. Ca^{2+} propagation was significantly faster in Fbs compared to CMs for a distance of $100 \mu\text{m}$ from the ablated cell (Sidak's multiple comparisons test, $\alpha = 0.05$). In order to exclude the possibility that the difference in propagation speeds arise from different methods used (slowly varying intensities for CMs and original intensities for Fbs), the propagation speeds in Fbs were also determined using slowly varying Ca^{2+} intensity values. Comparison of propagation speeds calculated from original intensities across all culture systems showed that the speeds in Fbs were significantly higher than in CMs (Fig. 3.17 b; Kruskal-Wallis test, $\alpha = 0.05$). While the propagation speeds in CMs were about $5 - 10 \mu\text{m/s}$ across a distance of $100 \mu\text{m}$, in Fbs the speeds were about $20 \mu\text{m/s}$ across a distance of $200 \mu\text{m}$. The difference in

propagation speed in CMs and Fbs across different culture systems suggested an underlying difference in Ca^{2+} propagation and regulation mechanisms in these cell types.

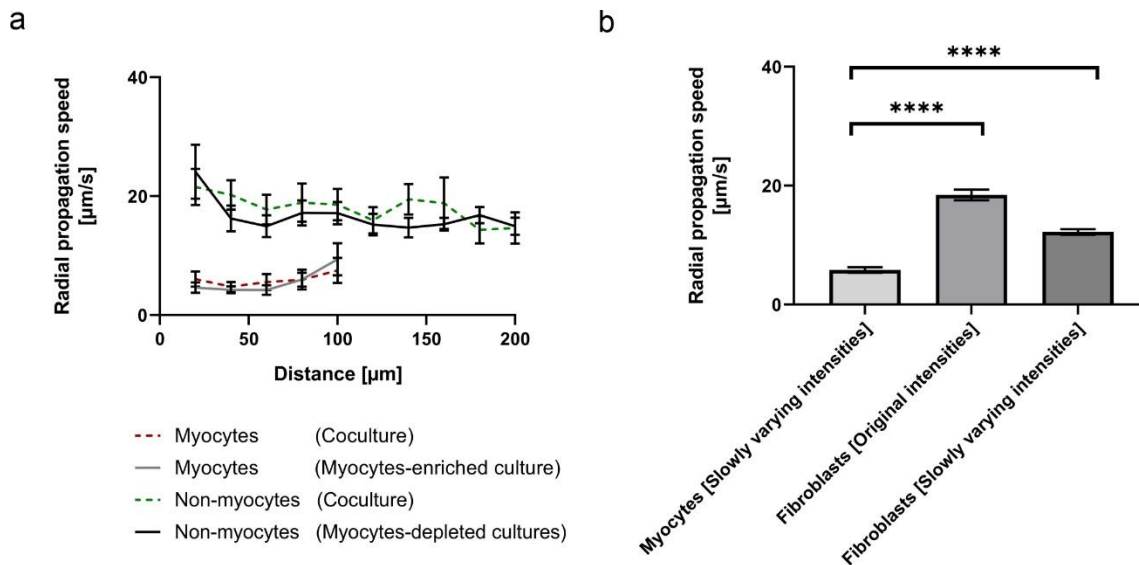


Figure 3.17: Cell-type-specific propagation of Ca^{2+} in myocardial cells: a) Plot showing mean radial Ca^{2+} propagation speed with distance in different cell culture systems represented as mean values with error bars showing s.e.m. Ca^{2+} propagation was faster in fibroblasts than cardiomyocytes in cocultures as well as enriched cultures, suggesting Ca^{2+} propagation speed was cell-type specific. **b)** Bar graph showing mean radial Ca^{2+} propagation speed in cardiomyocytes and fibroblasts from (a). Comparing Ca^{2+} propagation speed in cardiomyocytes with speed in fibroblasts determined using original as well as slowly varying intensity values showed that the speeds were significantly higher in fibroblasts (Kruskal-Wallis test, $\alpha = 0.05$). $N = 18$ ($n = 28$) for myocytes and $N = 17$ ($n = 25$) for non-myocytes. The significance levels were set to 5% ($\alpha = 0.05$) for all the analyses. P-value of < 0.05 was considered significant. The significance levels were indicated by * for p -value ≤ 0.05 , ** for ≤ 0.01 , *** for ≤ 0.001 and **** for ≤ 0.0001 .

To analyze the magnitude of ablation-induced $[\text{Ca}^{2+}]_i$ -increase in CMs and Fbs, the fold-change in $[\text{Ca}^{2+}]_i$ after ablation was determined (as described in section 2.9.2) for all culture systems. $[\text{Ca}^{2+}]_i$ fold-increase was higher in CMs (cocultures and myocytes-enriched cultures combined) compared to Fbs (cocultures and myocytes-depleted cultures combined) (Fig. 3.18 a). The $[\text{Ca}^{2+}]_i$ full recovery times were also determined for CMs and Fbs (refer section 2.9.2). The $[\text{Ca}^{2+}]_i$ recovery times were significantly higher in CMs (cocultures and myocytes-enriched cultures combined) compared to Fbs (cocultures and myocytes-depleted cultures combined) for a distance of up to 100 μm from the ablated cell (Fig. 3.18 b; Multiple t-tests, Holm-Sidak method, $\alpha = 0.05$). Moreover, similar to $[\text{Ca}^{2+}]_i$ fold-change, a decreasing

trend was found for recovery times with distance in CMs. Taken together, these results clearly suggest a higher magnitude of $[Ca^{2+}]_i$ -increase and a slower recovery to initial $[Ca^{2+}]_i$ levels in CMs compared to the Fbs. Moreover, the higher $[Ca^{2+}]_i$ increase and slower recovery in CMs closely connected to the ablated cell compared to the farther located CMs confirmed the observed distance-dependent effect (refer section 3.3) of ablation in CMs.

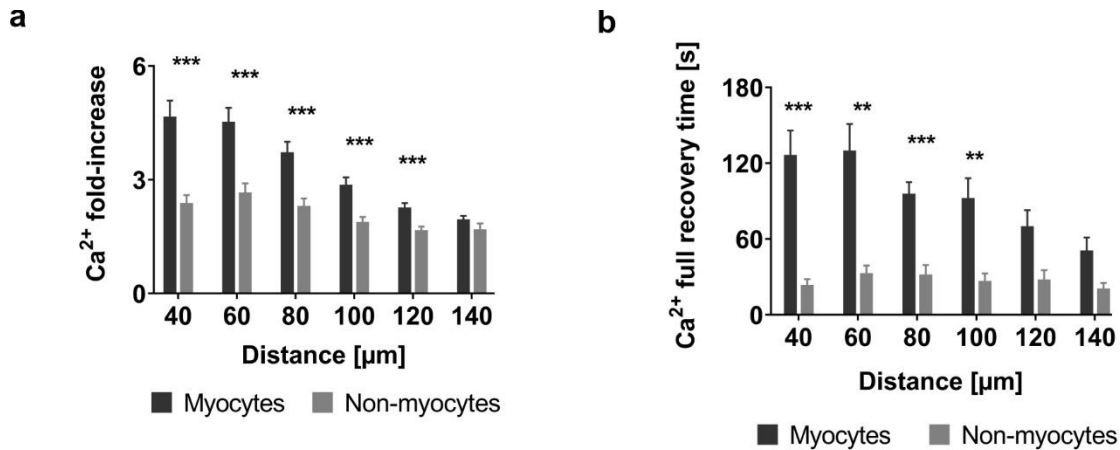


Figure 3.18: Ca^{2+} -increase and recovery in cardiomyocytes and non-myocytes: **a)** Graph showing mean $[Ca^{2+}]_i$ -increase in cardiomyocytes (cocultures and myocytes-enriched cultures) and fibroblasts (cocultures and myocytes-depleted cultures), with error bars showing standard error (s.e.m.). The $[Ca^{2+}]_i$ -increase was significantly higher for CMs close to the ablated-cell and decreased with distance (Multiple t-tests, Holm-Sidak method, $\alpha = 0.05$). $N = 18$ ($n = 28$) for myocytes and $N = 17$ ($n = 25$) for non-myocytes. **b)** Graph showing mean time-point (seconds) of recovery, i.e., when $[Ca^{2+}]_i$ values returned to values before ablation, in cardiomyocytes (cocultures and myocytes-enriched cultures) and fibroblasts (cocultures and myocytes-depleted cultures) at different distance from the ablated cell. The recovery times were significantly higher for cardiomyocytes compared to the fibroblasts for a distance of up to 100 μ m from the ablated cell. The error bars show standard error (s.e.m.). $N = 16$ ($n = 22$) for myocytes and $N = 15$ ($n = 21$) for non-myocytes. P-value of < 0.05 was considered significant. The significance levels were indicated by * for p -value ≤ 0.05 , ** for ≤ 0.01 , *** for ≤ 0.001 and **** for ≤ 0.0001 .

Overall, the analysis of $[Ca^{2+}]_i$ -changes in myocardial cells over time showed that the laser-induced death of single cells (CM/Fb) affected surrounding cells in the cluster. An increased $[Ca^{2+}]_i$ was observed in both CMs and Fbs in the cluster over time upon ablation. However, the impact of ablation was completely different in CMs and Fbs. While ablation resulted in a slow and sustained $[Ca^{2+}]_i$ -increase in connected CMs, a fast and transient $[Ca^{2+}]_i$ increase was observed in surrounding Fbs. $[Ca^{2+}]_i$ -increase in CMs was distance-dependent as cells closely located to the ablated cell were highly affected compared to the cells located farther. The

magnitude of $[Ca^{2+}]_i$ increase post ablation was significantly higher in CMs compared to Fbs. Furthermore, ablation-induced high $[Ca^{2+}]_i$ affected the contractility of CMs for a brief period of time and the contractility recovered following a decrease in $[Ca^{2+}]_i$ with time.

3.5 Recovery of contractility in cardiomyocytes affected by increased $[Ca^{2+}]_i$

Analysis of $[Ca^{2+}]_i$ -changes after ablation showed a brief loss of contractility in CMs closely connected to the ablated cell and detection of renewed peaks with time. In order to analyze the time point at which the contractility recovered after ablation in CMs, pre-ablation Ca^{2+} intensity peaks and renewed Ca^{2+} peaks after ablation were analyzed. As distinct Ca^{2+} peaks were no longer present following a high influx of Ca^{2+} into the cells, determination of the frequency of renewed contractile peaks was not possible after ablation. Therefore, the amplitude of Ca^{2+} peaks was compared before and after ablation using a Matlab routine described in section 2.9.2. Since a complete recovery of Ca^{2+} amplitudes could not be found during the experimental time-frame for many experiments, half-recovery times were determined. The time-point at which the amplitude post ablation recovered to values 50% of average amplitude before ablation was determined (half-recovery time) for each analysis ring (Ring 1-10). The half-recovery times were plotted across a distance of 200 μm to understand the distance-dependent recovery behavior in cells. As the first analysis ring contained the ablated cell, recovery cannot be determined for this ring and was therefore excluded from recovery analysis.

Plotting the mean half-recovery times across distance showed a decrease in half-recovery time with distance in coculture CMs (Fig. 3.19) (Sridhar et al., 2020). The mean half-recovery times ranged from 53 s (s.e.m. 11 s) in Ring 2 to 27 s (s.e.m. 4 s) in Ring 10 for $N = 10$ ($n=14$). Longer half-recovery times in closely connected cells (40 μm) and shorter half-recovery times in cells located at a long distance from the ablated cell once again confirmed the distance-dependent impact of ablation on surrounding cells. Further, half-recovery times of CMs in myocytes-enriched cultures also showed a decrease with a distance similar to that observed in cocultures. The mean half-recovery times in myocytes-enriched cultures ranged from 62 s (s.e.m. 14 s) in Ring 2 to 39 s (s.e.m. 6 s) in Ring 10, $N = 6$ ($n=9$) (Sridhar et al., 2020). The recovery times were higher for all analysis rings and more heterogeneous in enriched-cultures compared to those in cocultures. Although not significant, the difference in half-recovery times in CMs in myocytes-enriched cultures and cocultures indicated that the cell composition of these cultures may affect CMs recovery. More specifically, it could represent an underlying functional role of Fbs in CMs recovery.

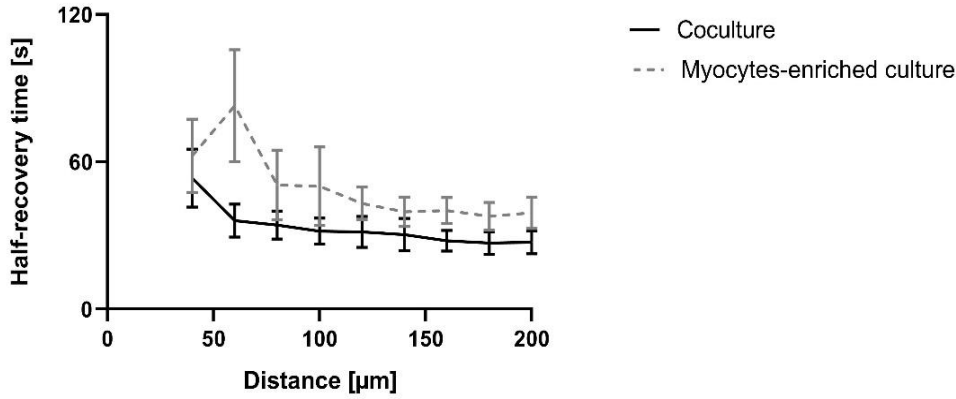


Figure 3.19: Recovery of contractility in cardiomyocytes in cocultures and myocytes-enriched cultures after ablation: Plot showing half-recovery times in cardiomyocytes in cocultures and myocytes-enriched cultures across a distance of 200 μm (Ring 2 - 10) from the ablated cell. Half-recovery times are given as mean values with error bars showing s.e.m. The half-recovery times showed a decreasing trend with distance in both coculture (N = 10) and cardiomyocytes enriched culture (N = 6). (Modified from Sridhar et al., 2020).

3.6 Ca²⁺-based connectivity between cardiomyocytes and fibroblasts

3.6.1 Patterned growth of cardiomyocytes and fibroblasts

Analysis of ablation-induced $[Ca^{2+}]_i$ changes indicated a difference in both Ca^{2+} propagation and regulation in CMs and Fbs. Moreover, a marginal difference in recovery behavior of CMs in cocultures and myocytes-enriched cultures indicated that the presence of Fbs in culture might have influenced CM recovery after ablation. To investigate whether Fbs mediate Ca^{2+} transport/signaling between CMs, CMs and Fbs were cultured in patterns using cell culture inserts as described in section 2.5. In silicone inserts containing three wells separated by a distance of 500 μm from each other, the central well was seeded with coculture cells while the other two wells were seeded with dense CM clusters obtained from fusion-based cell separation (refer section 2.2.3). Upon removal of inserts following cell attachment, Fbs from coculture mixture in the central well proliferated with time and eventually bridged the gap between CM clusters in the other wells by day 5. Immunolabelling of sarcomeric α -actinin (red) and F-actin (green) in these cultures confirmed the formation of fibroblast-bridges between CM clusters on either side as seen in Fig. 3.20.

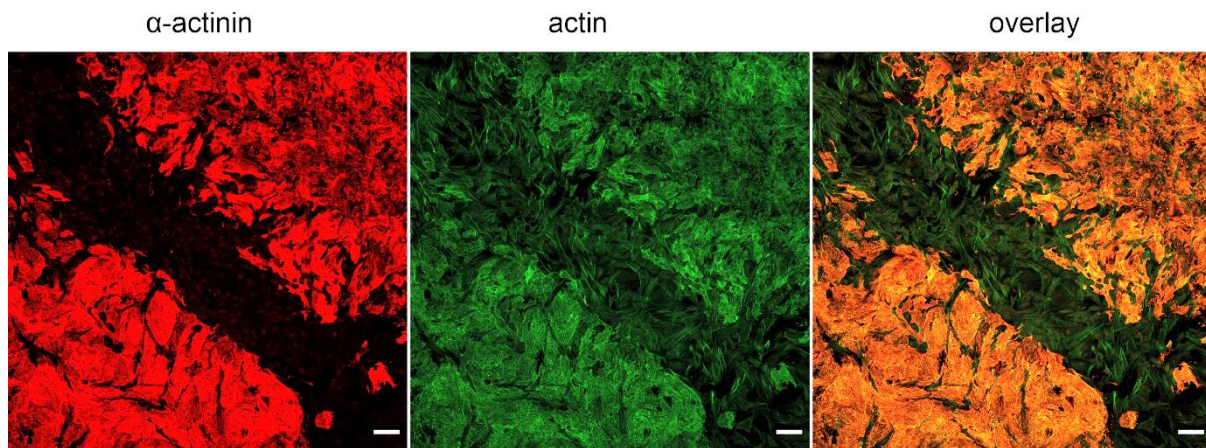


Figure 3.20: Patterned growth of cardiomyocytes and fibroblasts using cell culture inserts: Immunolabelling images showing cardiomyocyte clusters (left) from adjacent wells stained for sarcomeric α -actinin (red) and a composite image of the same (right) showing sarcomeric α -actinin (orange) and F-actin (green). Cardiomyocytes contained sarcomeres, while fibroblasts lacked sarcomeres and contained only F-actin. Fibroblasts from coculture well (right-side cluster) proliferated over time upon removal of culture-insert, bridging the gap between cardiomyocytes on either side by day 5. Scale bar: 100 μ m.

3.6.2 Fibroblasts mediated Ca^{2+} changes in myocyte-clusters separated by long distances

Fluo-4 labeling of cell clusters in culture inserts showed the presence of typical Ca^{2+} waves in CMs but not in Fbs (Fig. 3.21). Synchronized Ca^{2+} waves were observed in CM clusters on either side of the fibroblasts-bridge in day 5 culture. Moreover, analysis of $[\text{Ca}^{2+}]_i$ -changes also showed a synchronization of Ca^{2+} waves between CM clusters on either side of the fibroblast-bridge (increased $[\text{Ca}^{2+}]_i$ in Fig. 3.21 (center)), suggesting the presence of a Fbs-mediated coupling of contractility in CM clusters on either side.

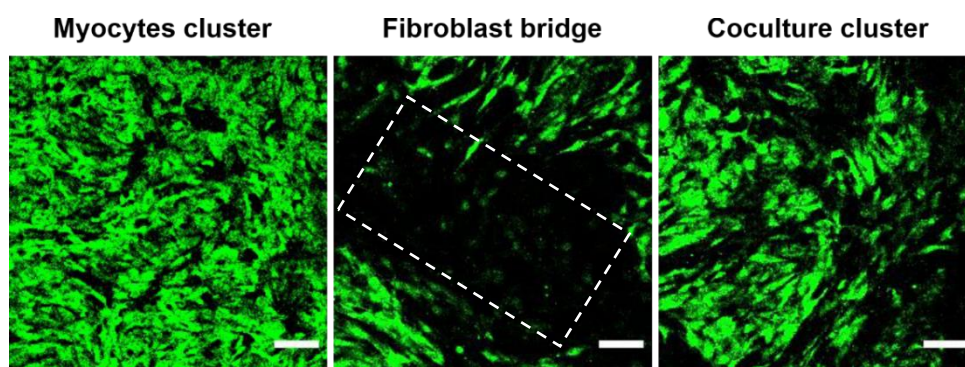


Figure 3.21: Spontaneous Ca^{2+} waves in cells cultured using culture-inserts: Ca^{2+} waves in Fluo-4 labelled cells in myocyte-enriched cluster, coculture cluster and fibroblast-bridge between the two clusters showing contraction in cardiomyocytes. Fibroblasts between myocyte clusters on either side are shown in the area bound by a rectangle (white). Scale bars: 50 μ m.

To analyze whether cell death in the CM cluster at one end affected the CMs on the other end, a single CM was selectively ablated in the CM cluster, as seen in Fig. 3.22 and supplementary movie 8. Ablation of CM resulted in an increased $[Ca^{2+}]_i$ in surrounding CMs of the cluster similar to the observations from cocultures and myocytes-enriched cultures. Increased $[Ca^{2+}]_i$ briefly affected the contractility of CMs. The contractility was gradually restored in affected CMs with decreasing $[Ca^{2+}]_i$ over time. More importantly, ablation-induced death of CM in the cluster at one end resulted in a brief interruption of contractility of CMs on the other side (supplementary movie 8), $N = 1$.

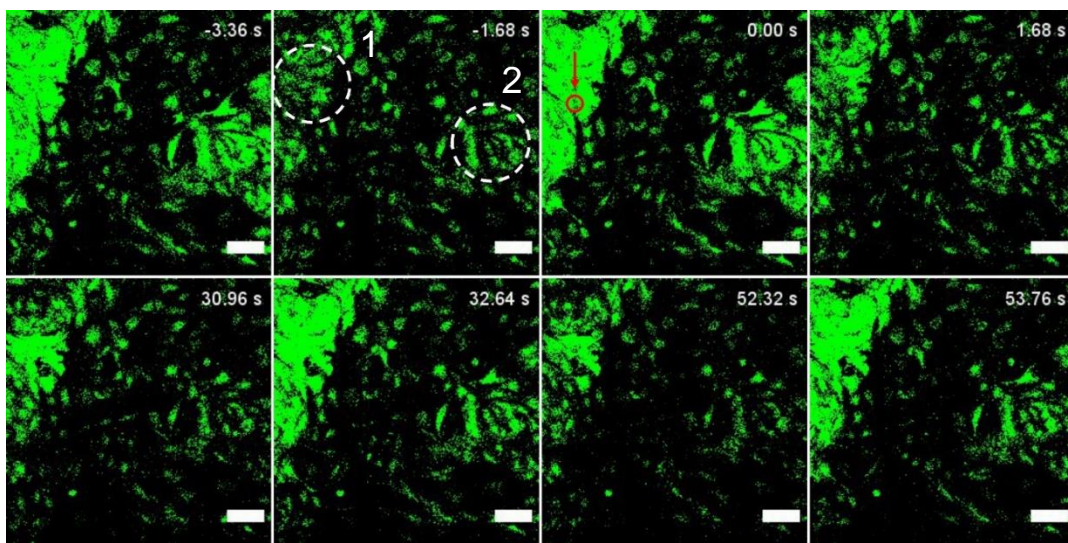


Figure 3.22: Ca^{2+} intensity-changes in clusters of cardiomyocytes separated by fibroblast-bridge: Time series images showing Ca^{2+} intensity-changes in Fluo-4 labeled cell clusters before and after ablation. Ca^{2+} waves can be seen in contracting cardiomyocyte clusters (marked by white circles) on either end separated by a distance of $\sim 500 \mu m$. Fibroblasts between cardiomyocyte clusters can be seen having minimal Ca^{2+} oscillations. Ablation of a cardiomyocyte (red) in cluster 1 resulted in Ca^{2+} increase in surrounding cardiomyocytes with time and further briefly affected cardiomyocyte contractility in cluster 2 (refer supplementary movie 8), $N = 1$. Scale bars: $50 \mu m$.

In order to qualitatively analyze the effect of ablation on both CM cell clusters as well as in the fibroblast-bridge, Ca^{2+} changes were plotted with time as seen in Fig. 3.23 a - c. Ablation of single CM resulted in an increased $[Ca^{2+}]_i$ in surrounding cells of the cluster (Ring 2 - 6) with time. Following ablation, a short spike in $[Ca^{2+}]_i$ was observed in the Fbs cluster, as shown in Fig. 3.23 b. Although the fibroblast-bridge predominantly consisted of Fbs, some CMs were still found, due to which oscillations in $[Ca^{2+}]_i$ could be observed. Moreover, a brief increase in $[Ca^{2+}]_i$ was also observed in the myocytes-cluster on the other side of the fibroblast-bridge

separated by a distance of $\sim 500 \mu\text{m}$ from the ablated cell as shown in Fig. 3.23 c. Ca^{2+} spike in fibroblast-bridge and myocytes-cluster at the far end following ablation suggested a fibroblast-mediated propagation of Ca^{2+} signals between CMs.

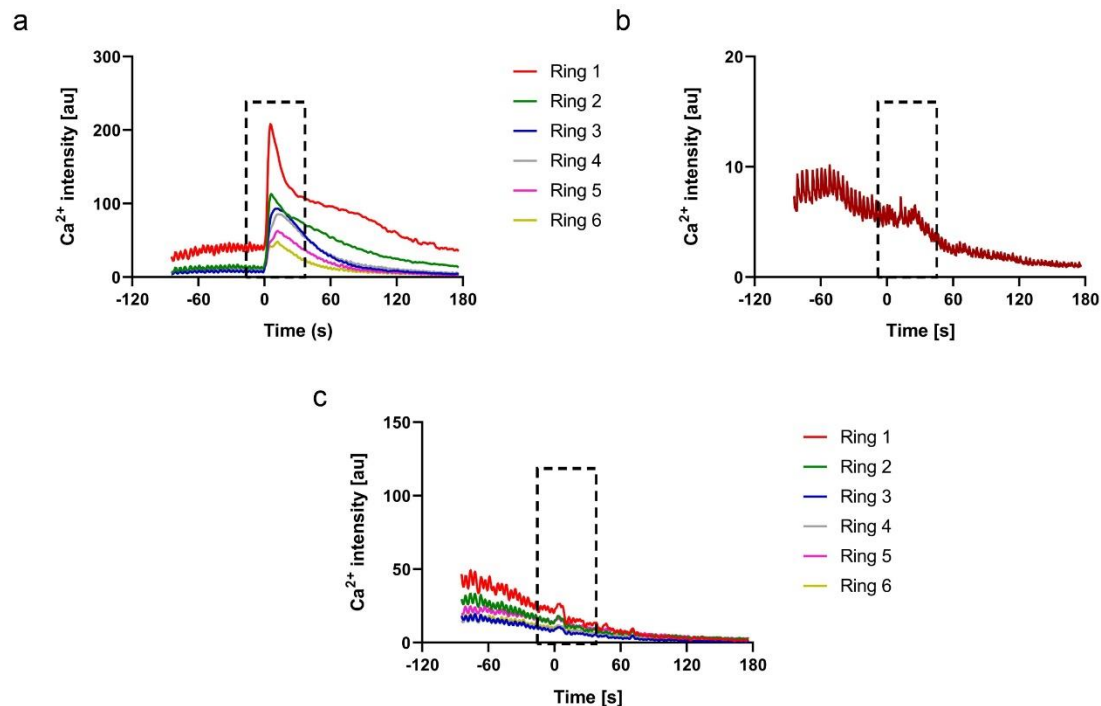


Figure 3.23: Ablation-induced Ca^{2+} changes in cardiomyocyte and fibroblast clusters: **a)** Plot depicting Ca^{2+} intensity-changes (slowly varying signal intensity) in cardiomyocytes in cluster 1 with time. Ablation of a single cardiomyocyte (Ring 1) in cluster 1 resulted in increased $[\text{Ca}^{2+}]_i$ in surrounding cardiomyocytes over time. The time point of ablation is set to $t = 0$ s. **b)** Plot of Ca^{2+} changes (original intensities) in fibroblasts showing a spike in Ca^{2+} closer to the time point of ablation indicating an ablation-induced Ca^{2+} increase. **c)** Ca^{2+} changes (slowly varying component) in cardiomyocyte cluster 2 upon ablation of single cardiomyocyte in the cluster located $500 \mu\text{m}$ apart and separated by fibroblasts.

Plotting Ca^{2+} changes before and after ablation in the CM cluster on the other side of the ablated cluster showed a briefly delayed contraction closer to the time point of ablation as seen from the single delayed Ca^{2+} peak in Fig. 3.24. The time point of ablation was set to $t = 0$ s. The time-point of interrupted contractility coincided with the time-point of maximum $[\text{Ca}^{2+}]_i$ in the plot shown in Fig. 3.23 a. The synchronous contractions in CM clusters separated by Fbs as well as the briefly interrupted contractility following ablation hence argue for a fibroblast-mediated functional coupling of CM clusters.

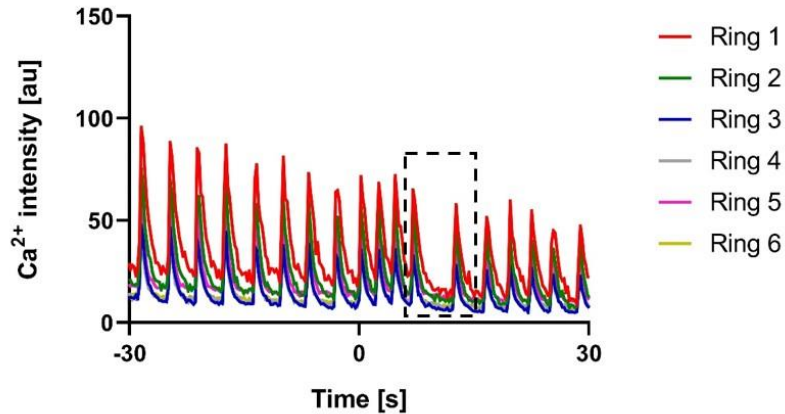


Figure 3.24: Effect of ablation on cardiomyocyte cluster at the other end of fibroblast-bridge: Plot depicting Ca^{2+} intensity-changes in myocyte cluster 2 (in Fig. 3.22) upon ablation of single myocyte in myocyte cluster 1. The time point of ablation was set to $t = 0$ s. Ablation of single cardiomyocyte in cluster 1 resulted in a delayed contraction in cardiomyocytes in cluster 2, as seen from the delayed Ca^{2+} peak in rhythmically contracting myocytes in the cluster.

3.7 Analysis of the long-term impact of ablation on affected cardiomyocytes

3.7.1 Long-term analysis of ablation-induced Ca^{2+} changes

Although the enhanced $[\text{Ca}^{2+}]_i$ in surrounding cells affected by ablation decreased with time, complete recovery to initial $[\text{Ca}^{2+}]_i$ levels before ablation was not observed during the experimental time-frame. In order to investigate if $[\text{Ca}^{2+}]_i$ levels after ablation recovered to initial levels with time, Ca^{2+} imaging was performed for a longer time duration. Following $[\text{Ca}^{2+}]_i$ -changes in cells after ablation for extended periods of time showed that the $[\text{Ca}^{2+}]_i$ levels returned to levels before ablation. Fig. 3.25 shows Ca^{2+} intensity changes for an extended duration in a CM cluster affected by ablation. Ablation ($t = 0$ s) resulted in an increased $[\text{Ca}^{2+}]_i$ in surrounding cells (Ring 2–6) with time. Ca^{2+} intensity changes in CMs in the cluster for a short period of time before and after ablation is shown on top in Fig. 3.25. Although bleaching of the fluorophore could have resulted in decreasing Ca^{2+} intensity over time, detection of renewed Ca^{2+} peaks ~ 25 min post ablation clearly indicated the recovery of contractility in affected CMs with decreasing $[\text{Ca}^{2+}]_i$ and therefore argue for recoverable stress levels for surrounding CMs over time, $N = 2$, $n = 3$. It can be noted that in Ring 2, which is closely connected to the ablated CM, the Ca^{2+} peaks were not as prominent as other rings, which may indicate a high inflow of Ca^{2+} had a lasting effect on contractility of only closely connected CMs in the cluster.

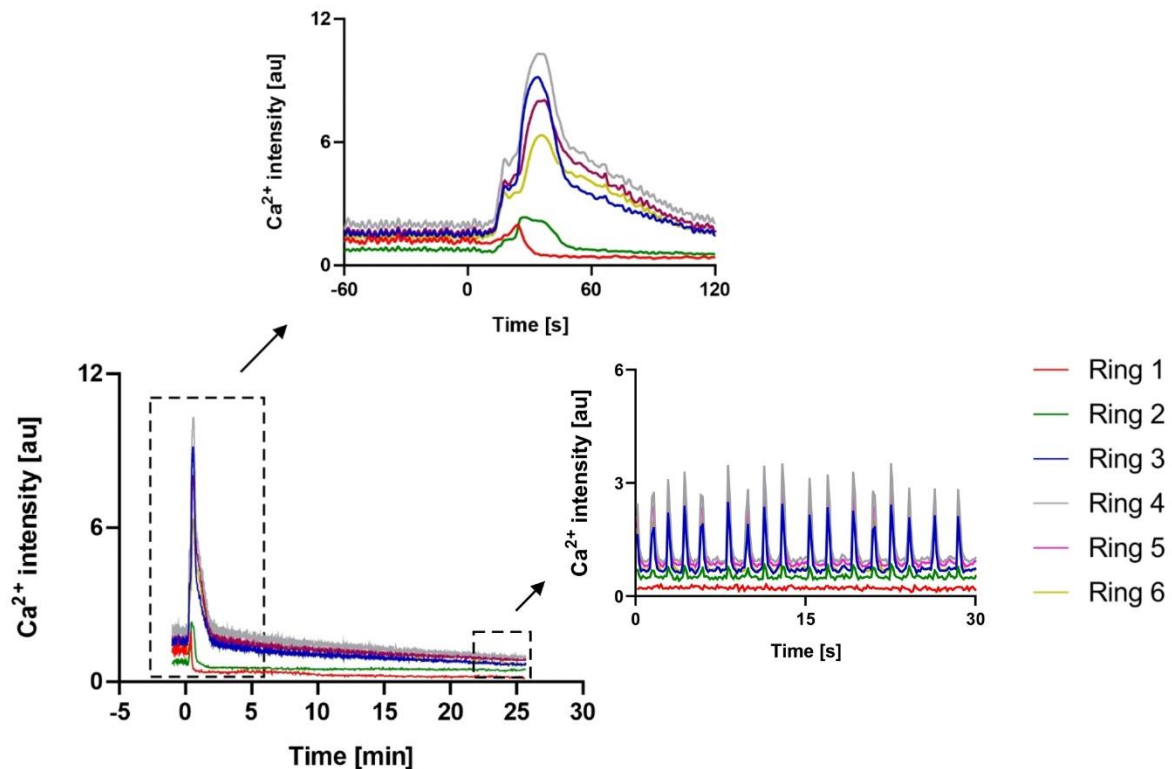


Figure 3.25: Long-term analysis of Ca^{2+} -changes in coculture cells after ablation: Changes in Ca^{2+} fluorescence intensity (slowly varying component) with time (in min), showing $[\text{Ca}^{2+}]_i$ of cells before and after ablation. $[\text{Ca}^{2+}]_i$ in affected cells was restored to normal levels with time. Inlay (top) shows Ca^{2+} fluorescence intensity values (slowly varying component) plotted against time (in sec) specifically for short duration before and after ablation ($t = 0$ s). Inlay (bottom) shows Ca^{2+} peaks ~ 25 min post ablation indicating the recovery of contractility in affected cells over time, $N = 2$.

3.7.2 Ablation-induced high $[\text{Ca}^{2+}]_i$ triggered strong contractility in cardiomyocytes

The high $[\text{Ca}^{2+}]_i$ in CMs post ablation resulted in a prolonged contracted state of cells until $[\text{Ca}^{2+}]_i$ decreased with time. The strong contractility in CMs affected by high Ca^{2+} inflow was accompanied by membrane retraction in connected cells of the cluster close to the point of ablation (Fig. 3.26 and supplementary movie 9). Fig. 3.26 shows the ablation ($t = 0$ s) of a single CM (red) in CMs cluster resulting in an increased $[\text{Ca}^{2+}]_i$ with time. As CMs contracted in clusters, sustained high $[\text{Ca}^{2+}]_i$ caused retraction of CMs (marked by white arrows) in the cluster. The ablation-induced retraction of cell membranes in the affected cluster was irreversible as seen from images showing decreased $[\text{Ca}^{2+}]_i$ (300 s and 360 s) after ablation.

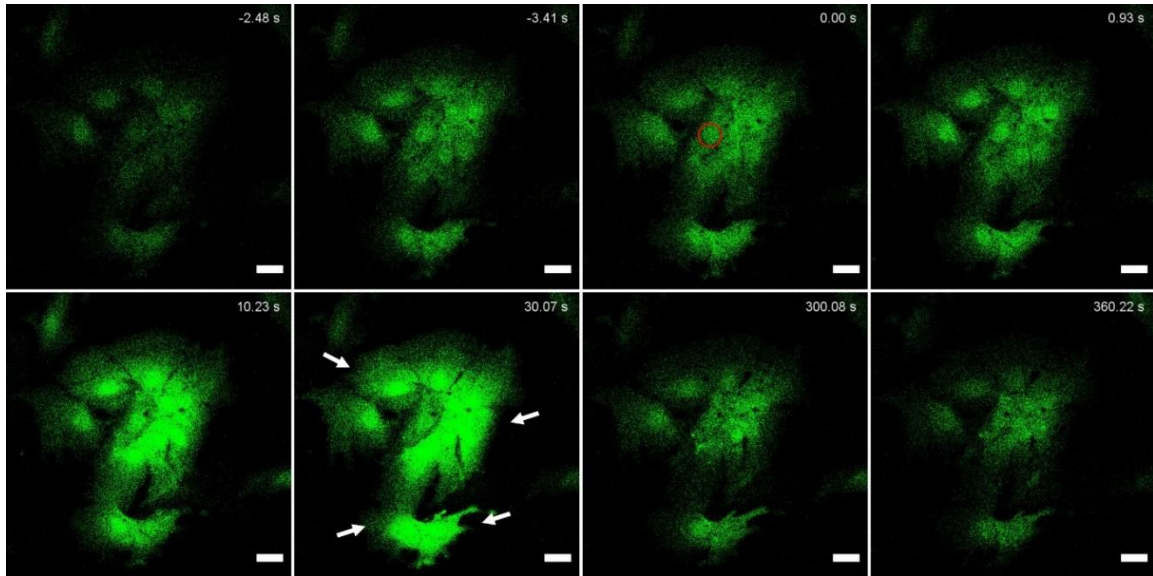


Figure 3.26: Impact of high $[Ca^{2+}]_i$ in myocytes affected by ablation: Time series images showing the increase in $[Ca^{2+}]_i$ over time following ablation. High $[Ca^{2+}]_i$ resulted in the loss of contractility as cells remained in a contracted state for a brief period of time after ablation. Sustained high $[Ca^{2+}]_i$ triggered retraction of cardiomyocytes in the cluster. Retracted cells are indicated by white arrows. Cardiomyocytes in close proximity as well as in distant locations from the ablated cell suffered damages as a result of high Ca^{2+} inflow (refer supplementary movie 9). Modified from (Sridhar et al., 2020). Scale bars: 20 μ m.

3.7.3 Analysis of contractile forces in cardiomyocytes before and after ablation

Since ablation resulted in an increased $[Ca^{2+}]_i$ and briefly impaired contractility in surrounding CMs with time, contractile forces were analyzed to quantitatively determine the ablation-induced changes to CM contractility. To investigate contractile force changes over time, CMs obtained after fusion-based cell separation were cultured on fluorescent bead-coupled elastomeric substrates ($E = 15$ kPa). On day 3, CMs contracted in clusters observed from rhythmic $[Ca^{2+}]_i$ changes. Small clusters of CMs (5 - 10 cells) were chosen for the analysis of traction force changes before and after ablation. Ablation of a single central CM in these clusters resulted in Ca^{2+} influx into clustered CMs over time as seen in Fig. 3.27 and supplementary movie 10. Similar to the effects of ablation in coculture and enriched culture CMs as described previously, Ca^{2+} levels decreased to values comparable to those before ablation with time, $N = 2$, $n = 6$.

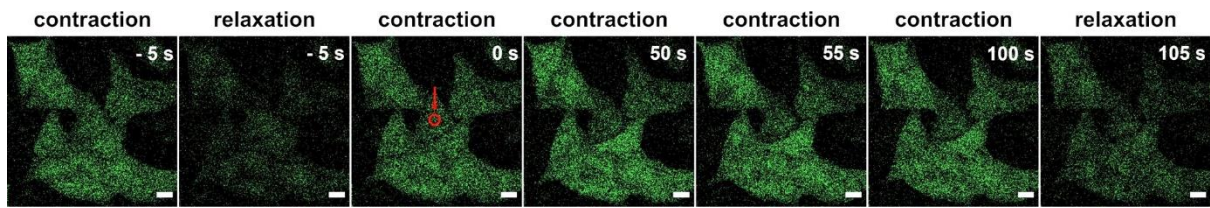


Figure 3.27: Effect of ablation of cardiomyocyte on surrounding cells in soft elastomeric substrates: Time series showing Ca^{2+} changes in cardiomyocytes in enriched cultures on soft substrates ($E = 15$ kPa) before and after ablation. The ablated cell is marked in red and the time point of ablation is set to $t = 0$ s. Ablation resulted in increased $[\text{Ca}^{2+}]_i$ in surrounding myocytes and with time $[\text{Ca}^{2+}]_i$ levels recovered (refer supplementary movie 10). Scale bars: $20 \mu\text{m}$.

To study the effect of ablation, Ca^{2+} changes were analyzed in individual cells (indicated as Cell area 1 – 5 in Fig. 3.28 a) as average grey values within the cell area for every time point. Ablation occurred at cell area 3. Plotting Ca^{2+} intensity values with time showed an increase in $[\text{Ca}^{2+}]_i$ in the surrounding cells (Cell area 1, 2, 4 and 5) over time as seen in Fig. 3.28 b.

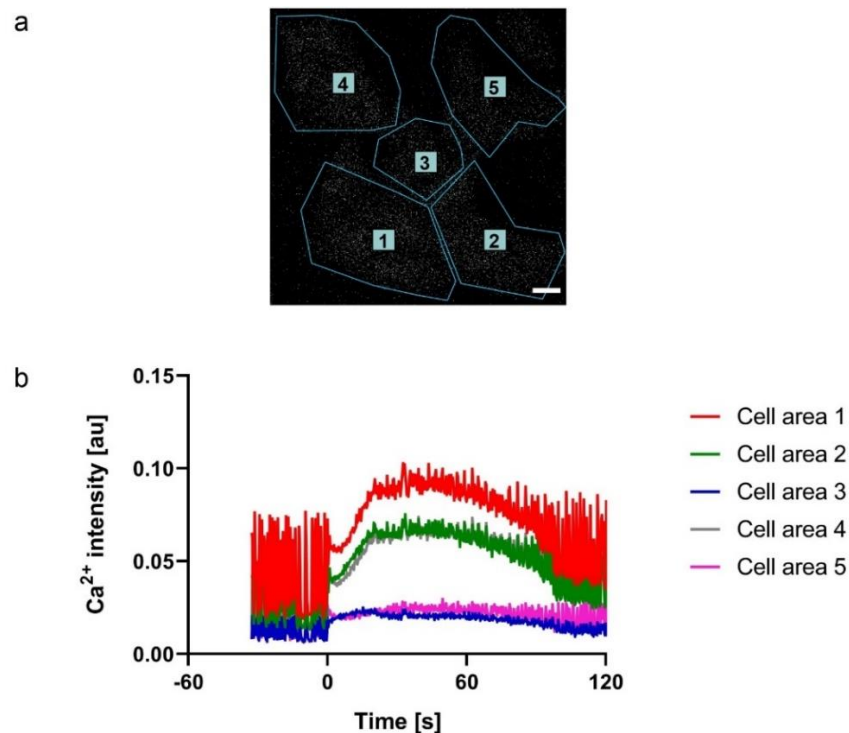


Figure 3.28: Analysis of ablation-induced Ca^{2+} intensity-changes in cardiomyocytes on soft bead-coupled substrates: **a)** Cell outline of contracting cardiomyocytes cultured on bead-coupled substrates ($E = 15$ kPa). Cells are labeled as Cell area 1 – 5. Scale bar: $20 \mu\text{m}$. **b)** Plot showing changes in Ca^{2+} fluorescence intensity in the cluster of cardiomyocytes before and after ablation. Ablation was performed in Cell area 3, and the time point of ablation is set to $t = 0$ s. Ablation resulted in increased $[\text{Ca}^{2+}]_i$ in surrounding cells (Cell areas 1, 2 and 4). $[\text{Ca}^{2+}]_i$ values decreased with time, and renewed contractile peaks were observed in affected cells, $N = 2$.

Analysis of ablation-induced Ca^{2+} propagation along CMs cultured on PDMS substrates showed trends very similar to those observed upon ablation in myocytes-enriched cultures on glass substrates as seen in Fig. 3.29 a (N=2, n=6). Analysis of half-recovery time with distance (Fig. 3.29 b) showed that the recovery was marginally faster on soft substrates compared to glass substrates and that the recovery times again decreased non-linearly with distance (N = 2, n=5). Since smaller clusters were chosen for the analysis of traction forces, half-recovery times were analyzed only up to 100 μm from the ablated cell.

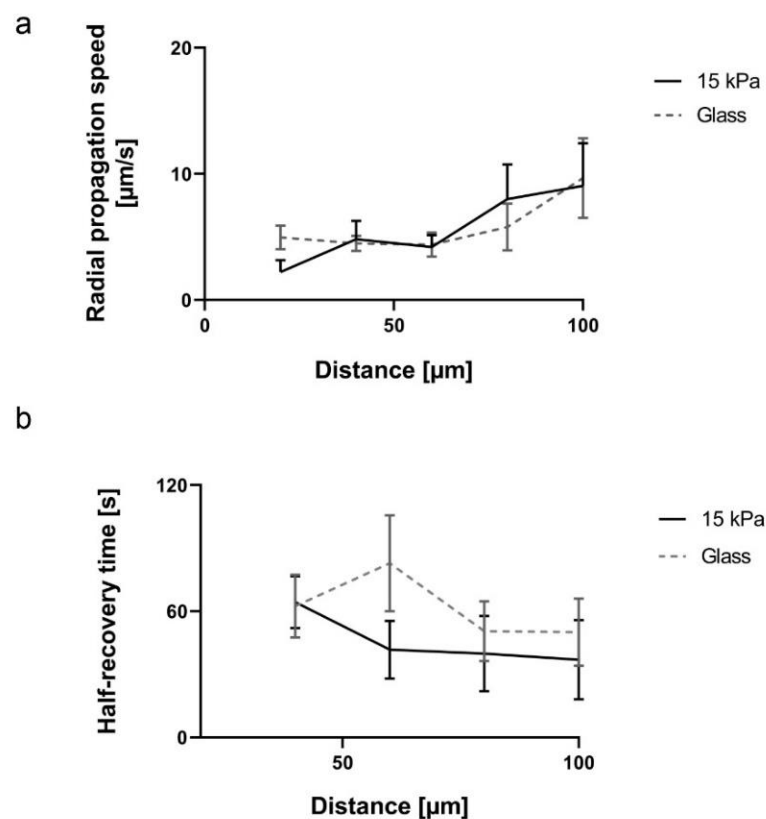


Figure 3.29: Analysis of ablation-induced Ca^{2+} propagation in cardiomyocyte clusters on soft substrates: a) Plot of Ca^{2+} propagation speeds with distance in myocytes-enriched cultures on glass and soft substrates ($E = 15$ kPa). Propagation speeds are given as mean values with s.e.m. error bars. Propagation speeds were similar across a distance of 100 μm from the ablated cell in glass and 15 kPa substrates, $N = 2$. **b)** Plot of mean half-recovery times with distance in myocytes-enriched cultures on glass and soft substrates with s.e.m. error bars showing a decrease in half-recovery time with distance. The half-recovery times were also almost comparable in glass and soft substrates, except that they were less heterogeneous in soft substrates than the times in glass substrates, $N = 2$.

In order to investigate the effect of single-cell death and subsequent $[Ca^{2+}]_i$ -increase on the contractile forces of surrounding cells in the cluster, contractile forces were determined for each cell area before and after ablation. As cells displayed synchronized contraction, the relaxed state of cells was taken as the reference for analysis of contractile forces. Here, the bead positions at relaxed state were taken as the reference from which displacement vector fields (DVF) and subsequently, traction stress exerted by the cells were calculated (refer section 2.9.3). Plotting the contractile forces for times before and after ablation showed a loss of contractility in surrounding CMs following ablation ($t = 0$ s) of a single central CM (Fig. 3.30 a). Comparison of contractile forces over time (Fig. 3.30 b) with temporal changes in $[Ca^{2+}]_i$ (Fig. 3.30 c) showed that the contractility of CMs increased following a high influx of Ca^{2+} into the cells upon ablation. CMs remained in the contracted state for a prolonged period of time that corresponded well with elevated levels of $[Ca^{2+}]_i$. Rhythmic contractions reappeared for decreasing $[Ca^{2+}]_i$ with time, as confirmed from the renewed detection of contractile force peaks. These results confirmed that the ablation-induced high $[Ca^{2+}]_i$ resulted in a high contractility and a loss of spontaneous contractile behavior in surrounding CMs.

Interestingly, a comparison of $[Ca^{2+}]_i$ and traction force-changes in surrounding CMs post ablation showed that the changes in contractile forces were in agreement with the $[Ca^{2+}]_i$ -changes as seen from Fig. 3.30 b, c. This confirmed the effect of ablation-induced $[Ca^{2+}]_i$ -increase on CM contractility. Moreover, the high contractile force after ablation could explain the prolonged contracture and retraction of CMs described previously (refer section 3.7.2). With decreasing $[Ca^{2+}]_i$, the (contractile) recovery behavior could be observed within ~ 2 minutes post ablation.

In Cell area 5 in Fig. 3.30 c, the $[Ca^{2+}]_i$ -increase was minimal and almost comparable to the increase in Cell area 3 (ablated cell) following ablation. However, the cell exhibited an increased contractile force. This could be due to the influence of connected CMs in the cluster or those extending outside of the field-of-view. Moreover, the Ca^{2+} intensity-changes also indicated that the CMs connected to the ablated cell is not affected by Ca^{2+} inflow alike. This difference could have arisen due to the difference in cell size and the magnitude of Ca^{2+} influx in these cells from the ablated cell.

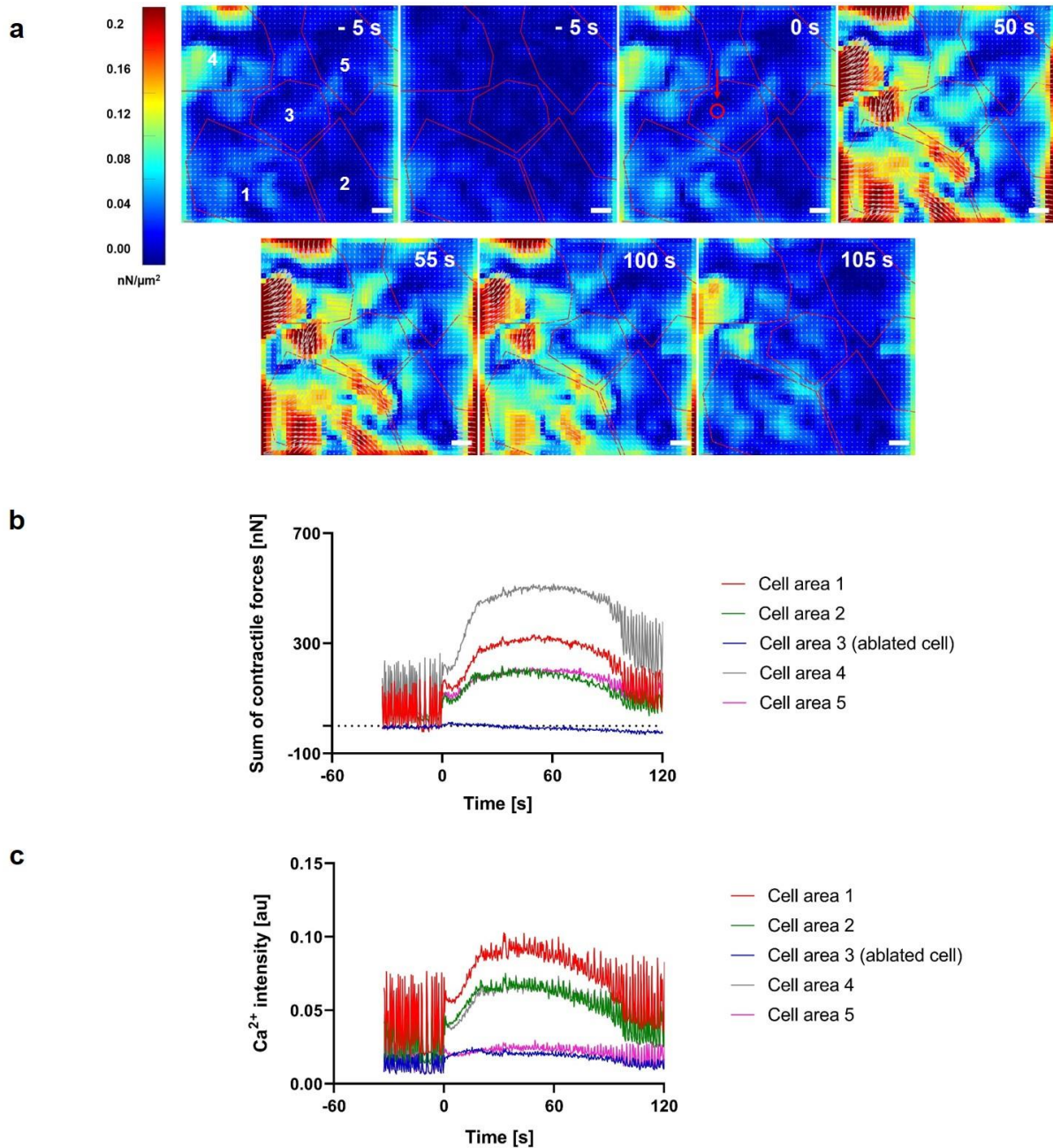


Figure 3.30: Analysis of contractile forces in cardiomyocyte cluster before and after ablation:
a) Time-series images showing contractile forces for times before and after ablation in a cluster of cardiomyocytes numbered 1 - 5. The time-point of ablation is set to $t = 0$ s. Ablation of a central cardiomyocyte (red) in the cluster resulted in an increased contractile force in surrounding myocytes. The forces decreased to levels comparable to pre-ablation levels with time. Scale bars: $20 \mu\text{m}$. **b)** Plot depicting changes in the sum of contractile forces in cells (Cell area 1 – 5) with times before and after ablation. The time point of ablation is set to $t = 0$ s. Ablation occurred in Cell area 3. Contractile forces in surrounding cells (Cell area 1, 2, 4 and 5) increased after ablation, followed by loss of distinct contractile peaks. Renewed contractile peaks were seen in the affected cells with time. **c)** Ca^{2+} intensity-changes in cardiomyocytes in the cluster over time (corresponding to the Figures 3.27 and 3.28). The increase in forces and subsequent recovery were in agreement Ca^{2+} increase and recovery, confirming that ablation of single myocyte affected connected myocytes by an increased contractile force resulting from a high cytosolic $[\text{Ca}^{2+}]_i$. The contractility recovered with decreasing $[\text{Ca}^{2+}]_i$ with time.

3.8 Mechanisms underlying ablation-induced Ca^{2+} propagation in myocardial cells

3.8.1 Diffusion of Ca^{2+} between cardiomyocytes upon ablation

Ablation-induced Ca^{2+} propagation followed different mechanisms in CMs and Fbs as seen from the Ca^{2+} propagation speeds along these cell types across different culture systems. In order to investigate the Ca^{2+} propagation in CMs in more detail, high-resolution Ca^{2+} imaging was performed on small clusters containing 4 - 5 connected CMs as described in (Sridhar et al., 2020). Ablation of a single CM resulted in Ca^{2+} inflow in a sequential manner from the point of ablation to the cell periphery and further to the connected cells, as seen in Fig. 3.31 and supplementary movie 11. Ca^{2+} propagated across the cells in 2 s from the time point of ablation ($t = 0$ s). Transfer of Ca^{2+} at cell-cell contacts (white squares) is shown in Fig. 3.31. The slow and sequential spread indicated diffusion of Ca^{2+} from one cell to another over time, $N = 2$.

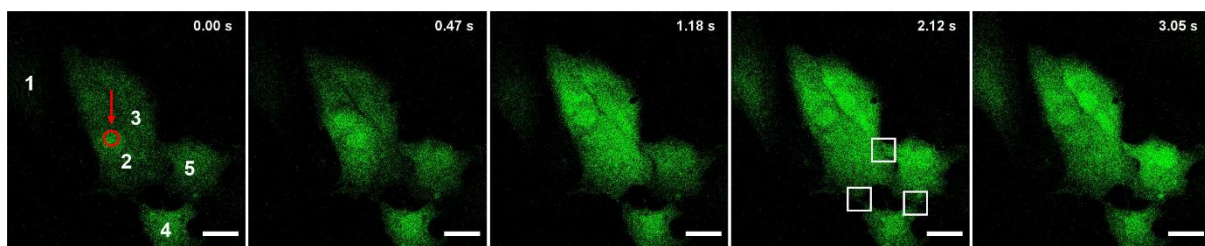


Figure 3.31: Intercellular mobility of Ca^{2+} at cell-cell junctions in cardiomyocytes: Time-series images showing Ca^{2+} flow along Fluo-4 labeled cardiomyocytes (green) after ablation (refer supplementary movie 11). The ablated spot is indicated in red. The connected cells in the cluster are numbered 2-5 and cell-cell contacts are marked by white squares, $N = 2$. Ca^{2+} flow along the cells from the ablated cell confirmed the direct transfer of Ca^{2+} between connected cardiomyocytes. Modified from (Sridhar et al., 2020). Scale Bars: 20 μm .

Analysis of Ca^{2+} intensity-changes over time confirmed the increase in $[\text{Ca}^{2+}]_i$ in every cell (numbered 1 – 5 in Fig. 3.32 a) following ablation. CMs in the cluster (cells 2 – 5) were non-contractile prior to ablation but could be well distinguished from non-myocytes (cell 1) based on the $[\text{Ca}^{2+}]_i$ levels in fluorescence images as well as from the Ca^{2+} intensity plot. Plotting Ca^{2+} intensity as grey values with time showed the increased $[\text{Ca}^{2+}]_i$ in connected CMs over time following ablation (Fig. 3.32 b). Although ablation-induced enhanced $[\text{Ca}^{2+}]_i$ in cells decreased over time, Ca^{2+} inflow into cell initiated contractility, particularly in cell 2.

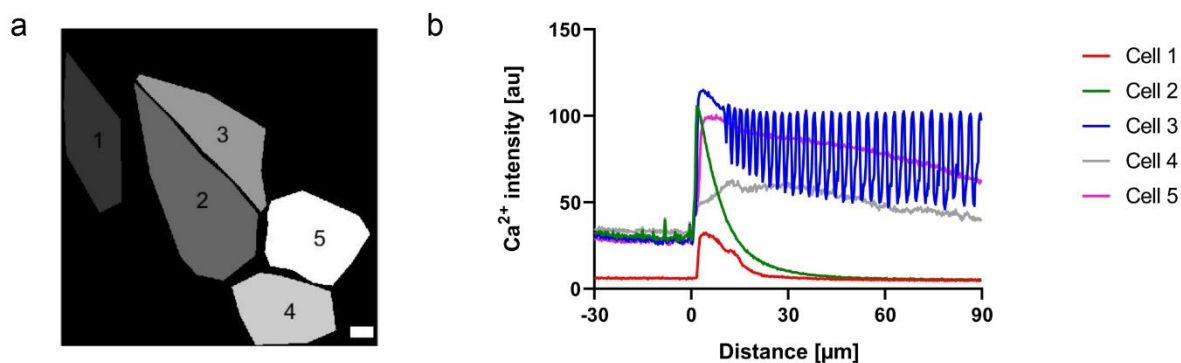


Figure 3.32: Analysis of ablation-induced Ca^{2+} propagation in cardiomyocytes: a) Figure showing an intensity mask of cardiomyocytes in the cluster (labeled 2 – 5) at a time-point before ablation. Scale bar: 10 μm . b) Plot depicting Ca^{2+} intensity in cardiomyocytes before and after ablation. Ablation occurred at Cell 2, and the time-point of ablation is set to $t = 0$ s. Ablation resulted in a drop in Ca^{2+} intensity in Cell 2, followed by a subsequent increase in $[\text{Ca}^{2+}]_i$ in connected cardiomyocytes (Cell 1, 3 and 4).

3.8.2 Analysis of gap junction proteins in cardiomyocytes and fibroblasts

Since gap junctions (GJs) regulate the diffusion of molecules and ions, including Ca^{2+} between connected CMs (Kumar & Gilula, 1996; C. Li et al., 2012), immunocytochemical analysis was performed to detect the presence of GJ proteins at cell-cell contacts. The gap junction alpha-1 protein, also known as connexin43 (Cx43), is the most prominently expressed GJ protein isoform in the heart (N. J. Severs et al., 2008). Therefore, cocultures of CMs and Fbs were stained for F-actin and connexin43 (Cx43). CMs were identified by the presence of densely packed sarcomeres, while non-myocytes lacked sarcomeres but contained prominent actin stress fibers. Immunocytochemical analysis using a monoclonal anti-Cx43 antibody showed Cx43 localized throughout Fbs (Fig. 3.33 a). However, Cx43-based GJ plaques could not be found at cell-cell contacts between CMs, CMs and Fbs or between Fbs.

To check for the presence of Cx43, Western blot analysis was performed with the protein-isolate from embryonic heart tissue and fibroblasts-overgrown cultures (14 days-old). Fibroblasts-overgrown cultures were used as three days-old cocultures and myocytes-depleted cultures contained numerous CMs. Fbs were passaged multiple times to remove CMs population. The cells used for the analysis were 14 days-old. Actin, which is present abundantly in both CMs and Fbs, was used as a protein control for the analysis. Western blot analysis revealed the presence of protein bands in both embryonic heart tissue and cells of fibroblasts-overgrown culture stained for actin (42 kDa) and Cx43 (43 kDa) (Fig.3.33 b).

Comparing the molecular weights of the protein bands with the ladder suggested the presence of a protein band at ~ 42 kDa, indicating the presence of actin. The protein band corresponding to Cx43 was found at ~ 50 kDa. The protein band size (~ 50 kDa) was comparable to the manufacturer's antibody testing data, and the increased molecular weight could be due to the phosphorylation of connexin43 phosphoprotein (Jeyaraman, Srisakuldee, Nickel, & Kardami, 2012).

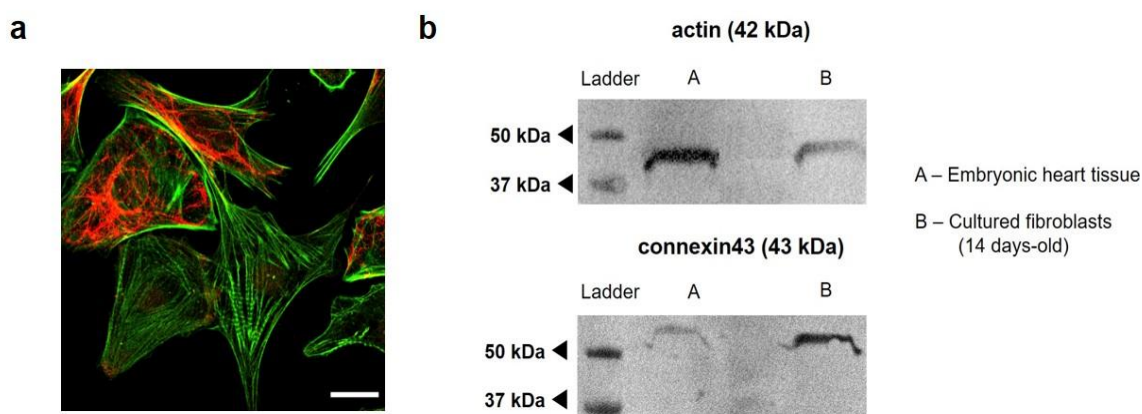


Figure 3.33: Analysis of proteins in heart tissue and cultured cells: a) Immunolabelling image of coculture of cardiomyocytes and fibroblasts stained for F-actin (green) and connexin43 (red). Cx43 was found in fibroblasts but gap junction plaques could not be found at cell-cell contacts between cardiomyocytes, cardiomyocytes and fibroblasts or between fibroblasts. Scale bar: 20 μ m. b) Immunoblot showing the presence of actin (42 kDa) and connexin43 (43 kDa) in total protein extract from embryonic heart tissue and fibroblasts-overgrown cultures.

Although Western blot analysis showed the presence of Cx43 in embryonic heart tissue and cells of fibroblasts-overgrown cultures, the presence of functional GJs could not be confirmed. Thereby, myocardial cells were immunolabelled for three major connexin isoforms involved in gap junction formation in mammalian hearts – connexin40 (Cx40), Cx43 and connexin45 (Cx45) (Desplantez, 2017; Gros & Jongasma, 1996) using polyclonal antibodies specific to these proteins. Among the different connexin isoforms, Cx43 was particularly found in CMs. Cx43-plaques were found along cell-cell contacts between adjacent CMs (Fig. 3.34). In this analysis, CMs in culture can be distinguished from non-myocytes based on F-actin staining. Cx43 was not found at CM-Fb and Fb-Fb cell-cell contacts across all culture systems, indicating the specificity of Cx43 protein for CMs. Moreover, other connexin isoforms - Cx40 and Cx45 were also absent in CM-CM, CM-Fb and Fb-Fb pairs across different culture systems, as seen in Fig. 3.34. Additionally, fibroblasts-overgrown cultures (14 days-old) were prepared in order to investigate the presence of GJ proteins in mature and well differentiated

Fbs. Immunocytochemical analysis showed the absence of all three GJ proteins (Cx40, Cx43 and Cx45) in these cells suggesting that Fbs lacked GJs in culture.

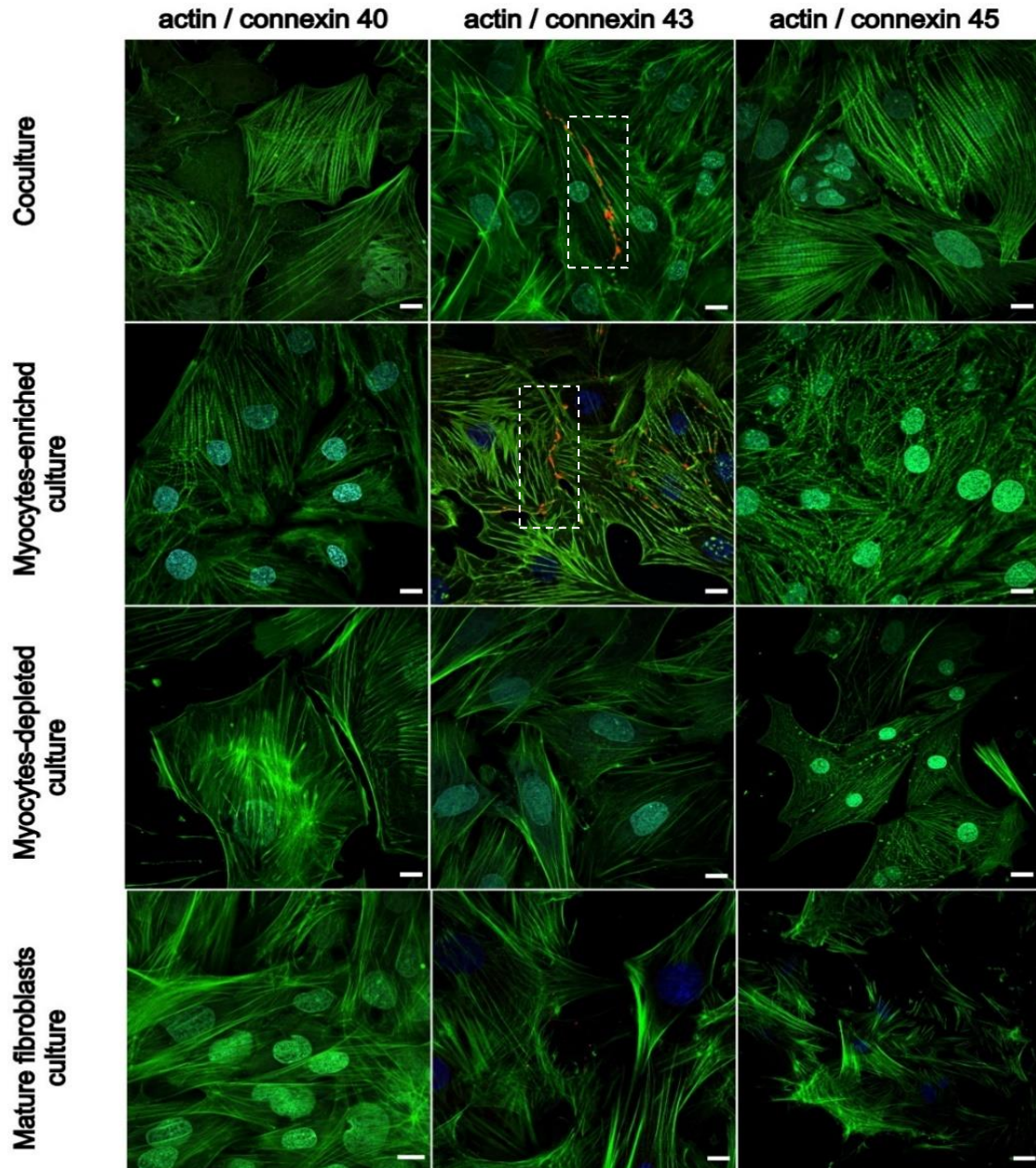


Figure 3.34: Immunocytochemical labelling of cardiomyocytes and fibroblasts for gap junction proteins: Immunocytochemical labelling of cells for gap junction proteins Cx40/Cx43/Cx45 (red), F-actin (green) and nucleus (blue). Cardiomyocytes can be identified by the presence of densely-packed sarcomere structures while fibroblasts lacked sarcomeres. Cx43-based gap junction plaques (red) can be seen at cell-cell contacts of cardiomyocytes (white-dotted lines) in both cocultures and myocytes-enriched cultures. Cx43 was absent in fibroblasts both in cocultures and myocytes-depleted cultures. Cx40 and Cx45 were absent in both myocytes and fibroblasts across all culture systems. Scale Bars: 10 μ m.

As described earlier, immunocytochemical analysis for gap junction proteins showed the presence of Cx43 between CMs. A high-resolution imaging of two closely connected CMs in cocultures showed the presence of Cx43 plaques along the cell-cell contact area between the cells as seen in Fig. 3.35.

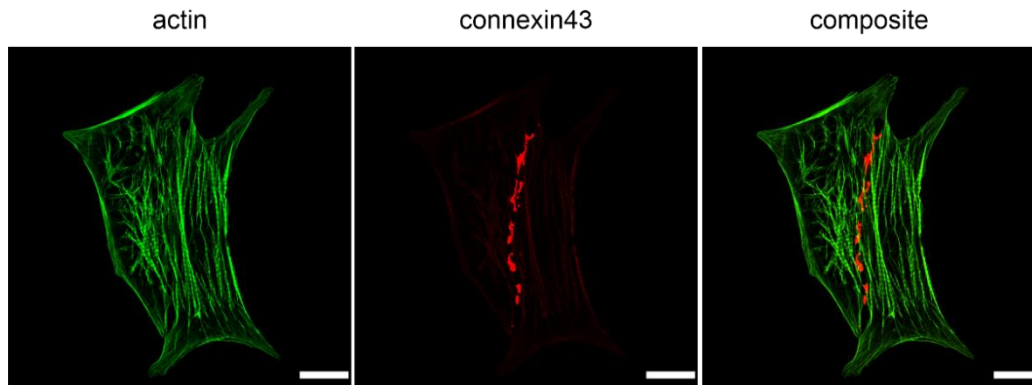


Figure 3.35: Immunocytochemical labeling of gap junction protein connexin43 in cardiomyocytes: Immunolabelling images showing cardiomyocytes stained for F-actin (green) and gap junction protein connexin43 (red). Connexin43 plaques can be seen localized along cell-cell contacts between the adjacent cardiomyocytes. Scale Bars: 10 μm .

To confirm whether the Cx43-based GJ plaques were specific to CMs, immunocytochemical co-labelling of Cx43 and α -actinin were performed in all three cell culture systems (Sridhar et al., 2020), as shown in Fig. 3.36. In myocytes-enriched cultures, Cx43-based gap junction plaques were found localized at cell-cell contacts between CMs. In coculture, Cx43-based gap junction plaques were found in cell-cell contacts between CMs but not between CMs and Fbs. In myocytes-depleted cultures, no Cx43-based gap junction plaques were found between the Fbs.

Taken together with high-resolution analysis of Ca^{2+} changes in connected CMs, the results from immunocytochemical analysis argue for Ca^{2+} propagation through Cx43-based gap junctions in CMs following laser-induced single cell death. In Fbs, Cx40/Cx43/Cx45 –based cell-cell contacts could not be detected, suggesting a lack of gap junction coupling in these cells. Although western blot analysis detected the presence of Cx43, the proteins extracted from the cells were 14 days-old Fbs, whereas the ablation experiments were performed on cultures that were not more than seven days old and predominantly in cultures that were three days old. Immunolabelling of Cx43 using a monoclonal antibody used for western blot analysis could

not detect specific gap junction plaques between Fbs or between CMs and Fbs. These results indicated a different mode of Ca^{2+} propagation in Fbs for which specific molecular markers could not be identified with certainty in this thesis work. Identification of molecular entities that facilitate Ca^{2+} propagation along Fbs could be useful for in-depth understanding of the basis of CM-Fb and Fb-Fb connectivity and underlying signaling mechanisms in the heart.

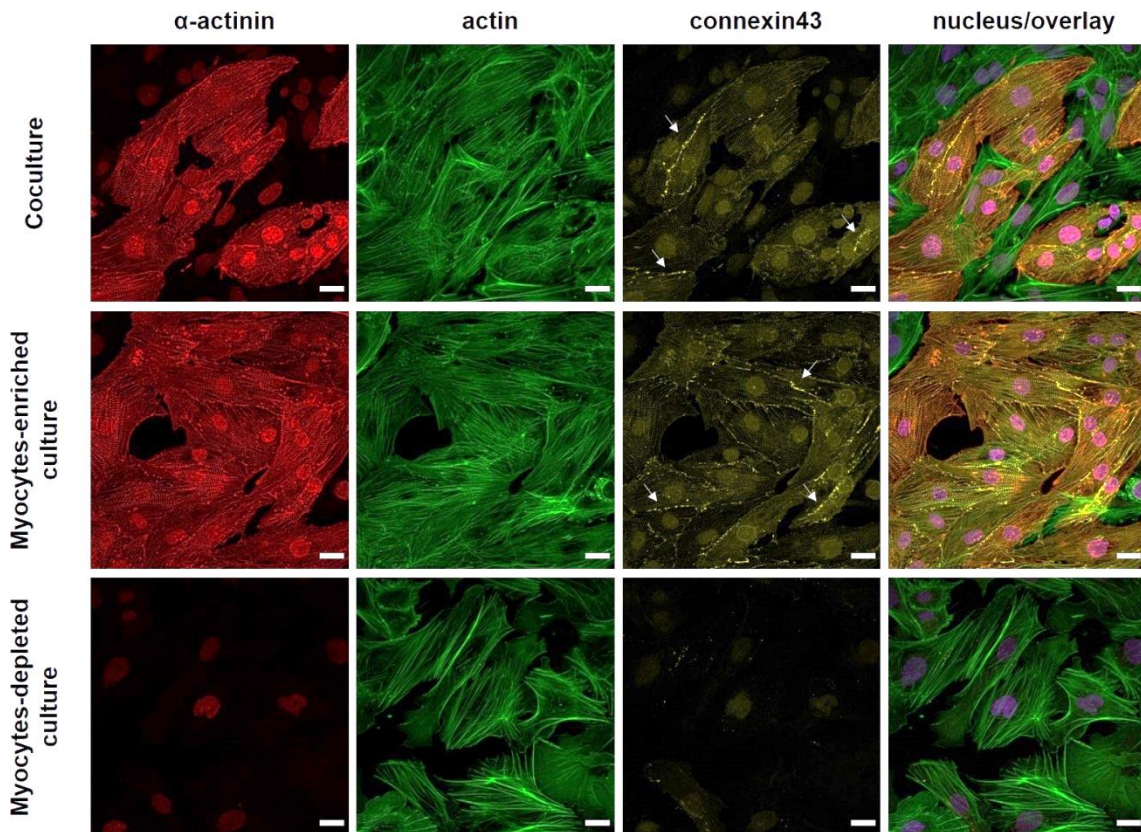


Figure 3.36: Immunocytochemical analysis to determine the specificity of Cx43-based gap junctions: Co-staining of Cx43 (yellow), myocyte-specific α -actinin (red), F-actin (green) and nucleus (blue) in coculture, myocytes-enriched culture and myocytes-depleted cultures. Co-staining of α -actinin and Cx43 clearly show the presence of gap junction protein Cx43 only between myocytes but not between fibroblasts or between myocytes and fibroblasts. The gap junction plaques are indicated using arrows. Modified from (Sridhar et al., 2020). Scale bars: 20 μm .

Chapter 4 Discussion

The myocardial tissue function is dependent on the functional connectivity between its constituent cells. Owing to the intercellular connectivity, injury/death of the constituent cells could be communicated to the connected cells to elicit a coordinated response in the tissue (Garcia-Dorado & Ruiz-Meana, 2000). Following a myocardial injury, the fate of the myocardial tissue and disease progression can be attributed to the adaptation/maladaptation of cells over time (Dispersyn et al., 2002; Matsushita et al., 1999). Therefore, investigating the response of connected myocardial cells to cell death in myocardial tissues and the underlying signaling mechanisms is essential to understand the pathophysiology of myocardial injury. The findings from this thesis work illustrate the impact of laser-induced single-cell death on surrounding cardiomyocytes (CMs) and fibroblasts (Fbs) in myocardial cell clusters based on intracellular Ca^{2+} concentrations ($[\text{Ca}^{2+}]_i$). The effects of targeted ablation of single cells in myocardial cell clusters, accompanying signals and response of surrounding cells are discussed in detail in the upcoming sections.

4.1 Mechanisms underlying $[\text{Ca}^{2+}]_i$ regulation in CMs

Ca^{2+} is a second messenger in cells which is involved in the signaling of various cellular functions. Ca^{2+} -mediated signaling works through cellular or organelle level changes in $[\text{Ca}^{2+}]$. $[\text{Ca}^{2+}]_i$ homeostasis is tightly maintained in cells through ion channels, pumps and associated transport proteins (Bagur & Hajnóczky, 2017; Carafoli, 2002). In CMs, Ca^{2+} is an essential link between excitation and contraction (E-C coupling) and therefore, cellular $[\text{Ca}^{2+}]$ changes are directly linked to CMs functionality (Eisner et al., 2017; Fearnley et al., 2011). In this study, cellular response to single-cell death was analyzed on the basis of spatial and temporal $[\text{Ca}^{2+}]$ changes. The findings from this work showed a distance-dependent $[\text{Ca}^{2+}]_i$ -increase in CMs surrounding the ablated cell over time, indicating a passive flow of Ca^{2+} along the connected CMs starting from the ablated spot. The increased cytosolic $[\text{Ca}^{2+}]$ briefly interrupted the rhythmic contractile behavior of the cells. Interestingly, a gradual recovery of contractility was observed with decreasing $[\text{Ca}^{2+}]_i$ in a time range of a few minutes (~ 2 min) post ablation (refer supplementary movie 4).

The increased $[\text{Ca}^{2+}]_i$ in surrounding CMs upon ablation of a single cell in the cluster and subsequent recovery can be explained by the intracellular regulation of Ca^{2+} by different regulatory mechanisms. In CMs, intracellular $[\text{Ca}^{2+}]$ levels are primarily regulated by distinct Ca^{2+} influx and efflux mechanisms that include voltage-gated L-type calcium channels

(LTCCs), sodium-calcium (Na^+ - Ca^{2+}) exchanger (NCX), sarcoplasmic/endoplasmic reticulum calcium-ATPase (SERCA) and ryanodine receptors (RyRs). While the cytosolic influx of Ca^{2+} is predominantly governed by LTCCs (in the plasma membrane) and RyRs (in sarcoplasmic reticulum (SR)), efflux of cytosolic Ca^{2+} is governed by NCX (in the plasma membrane) and SERCA2a (in SR) (Bers, 2000; Fearnley et al., 2011). The observed $[\text{Ca}^{2+}]_i$ -increase in CMs surrounding the ablated cell could have been mediated by different Ca^{2+} entry mechanisms. Firstly, a direct transfer of Ca^{2+} from the ablated CM to the connected CMs through intercellular junctions (Garcia-Dorado & Ruiz-Meana, 2000). Secondly, the instant death of CMs could result in disrupted cell-cell junctions through which a surge of extracellular Ca^{2+} may flow into the surrounding CMs (C. Li et al., 2012). Thirdly, Ca^{2+} entry through other Ca^{2+} channels such as voltage-gated Ca^{2+} channels also presents a possible means of Ca^{2+} entry into CMs. Moreover, an influx of Ca^{2+} from the ablated cell into the surrounding CMs could trigger a release of Ca^{2+} from the SR (calcium-induced calcium release (CICR)), which stores about 1000-fold higher Ca^{2+} than cytosol (Fearnley et al., 2011).

While an entry of extracellular Ca^{2+} through voltage-gated L-type channels and subsequent CICR-induced $[\text{Ca}^{2+}]_i$ increase in connected CMs is possible, this may not represent the primary mechanism underlying a high $[\text{Ca}^{2+}]_i$ following ablation. This is due to the gating of L-type calcium channels in CMs. When Ca^{2+} enters the CM through L-type channels, it activates the CICR pathway, which increases cytosolic $[\text{Ca}^{2+}]_i$, following which these channels are closed by voltage and intracellular $[\text{Ca}^{2+}]_i$ gating mechanisms (Kubalová, 2003). Therefore, no further entry of Ca^{2+} is possible. However, in the findings from this work, the mean $[\text{Ca}^{2+}]_i$ -increase was found to be more than two-fold in the closely connected CMs after ablation, suggesting that Ca^{2+} influx through mechanisms besides L-type and CICR mediated entry. Moreover, the voltage-dependent increase would have resulted in a comparable magnitude of $[\text{Ca}^{2+}]_i$ -increase in CMs located at different distances from the ablated cell. However, a distance-dependent increase was observed, suggesting that L-type and CICR based entry was not the primary Ca^{2+} entry mechanism in surrounding CMs following ablation.

The high-resolution analysis of Ca^{2+} in CMs showed a direct transfer of Ca^{2+} sequentially into the connected cells with time (refer Fig. 3.31 and supplementary movie 11). In CMs, gap junctions (GJs) form intercellular connections that enable the flow of molecules and ions, including Ca^{2+} , into the connected cells. The disruption of these cell-cell junctions could result in an inflow of extracellular Ca^{2+} . However, gating mechanisms have been identified, which results in uncoupling of gap junctions at high $[\text{Ca}^{2+}]_i$ (Peracchia, 2004; Wei, Cassara, Lin, &

Veenstra, 2019), and this mechanism could prevent further entry of Ca^{2+} . Although the CICR pathway and extracellular Ca^{2+} entry through GJs may represent additional mechanisms of $[\text{Ca}^{2+}]_i$ -increase in CMs after ablation, the findings strongly argue that the direct flow of Ca^{2+} from the ablated cell to the connected cells represent the primary mechanism underlying the observed $[\text{Ca}^{2+}]_i$ -increase.

The brief interruption in contractility in CMs affected by a high cytosolic $[\text{Ca}^{2+}]_i$ can be explained by Ca^{2+} handling in CMs. It had been previously reported in CMs that only about 1% of cytoplasmic Ca^{2+} remains free while the remainder is being bound to cytoplasmic buffers, of which the troponin C (TnC) followed by SERCA2a (SERCA isoform in CMs) are the two most predominant buffers of Ca^{2+} (Smith & Eisner, 2019). TnC is a calcium-binding sub-unit of the troponin complex (refer section 1.2.3), while SERCA2a is a Ca^{2+} pump through which cytosolic Ca^{2+} is pumped into SR after sarcomere contraction.

The affected contractility of CMs following a high $[\text{Ca}^{2+}]_i$ in CMs can be explained by the binding of cytosolic Ca^{2+} to TnC in myofilaments. As myofilament contraction and relaxation occurs by constant binding and unbinding of Ca^{2+} in TnC, a high cytosolic $[\text{Ca}^{2+}]_i$ meant that Ca^{2+} was readily available to bind and not recycled constantly into the SR. Moreover, the sensitivity of TnC to Ca^{2+} also influences the rate of contraction (Davis & Tikunova, 2008). The SERCA2a pump activity depends on the dissociation of phospholamban (PLN) from SERCA2a-PLN complex. Previous studies had shown that this dissociation can be regulated by high cytosolic Ca^{2+} . However, it is not clearly understood if Ca^{2+} overload, which is several times in magnitude than physiological systolic $[\text{Ca}^{2+}]_i$, could upregulate SERCA2a activity. Therefore, following ablation, the high cytosolic $[\text{Ca}^{2+}]_i$, resulting in constant Ca^{2+} binding to myofilaments could explain the affected contractility of CMs.

The $[\text{Ca}^{2+}]_i$ levels and contractility of the affected CMs recovered over time. In CMs closely located to the ablated cell (40 μm), the mean contractile half-recovery times were ~ 1 min in cocultures and myocytes-enriched cultures. Moreover, in CMs across all culture systems, full $[\text{Ca}^{2+}]_i$ recovery could be seen within 2-3 min from the time-point of ablation. In CMs from coculture as well as myocytes-enriched culture, the recovery of contractility went along with the efflux of excess Ca^{2+} from the cells. Thereby, the farther the cells were from the ablated cell, the lesser the ablation-induced Ca^{2+} inflow and faster recovery of $[\text{Ca}^{2+}]_i$ and contractility (Fig. 3.18). The faster recovery for less affected CMs and a slower recovery for CMs highly affected by Ca^{2+} inflow suggested a systematic extrusion of Ca^{2+} from the affected CMs over

time (Bers, 2000). The various Ca^{2+} regulatory mechanisms in CMs are summarized in Fig. 4.1. Additionally, Ca^{2+} regulation by mitochondrial Ca^{2+} uniporter (MCU) is also shown which regulate mitochondrial $[\text{Ca}^{2+}]$. The importance of mitochondrial Ca^{2+} levels is described later.

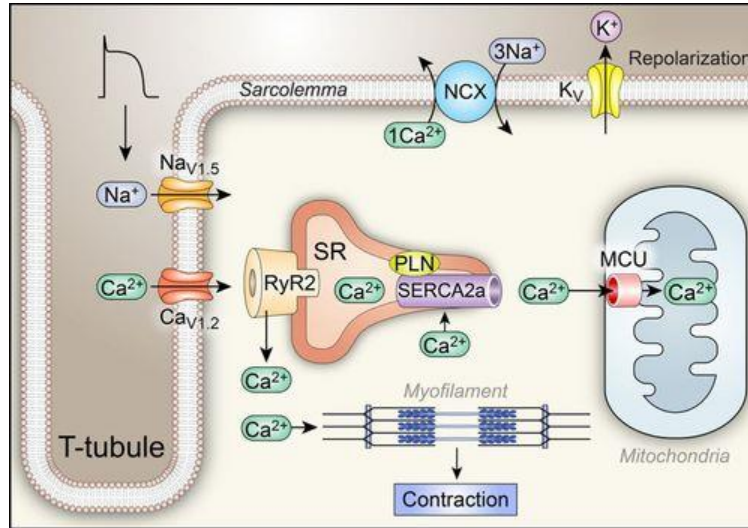


Figure 4.1: Ca^{2+} regulation in cardiomyocytes: Schematic illustration of Ca^{2+} regulatory mechanisms in cardiomyocytes. Membrane potential changes from action potential current (mediated by voltage-gated Na^+ and K^+ channels) facilitate Ca^{2+} entry through voltage-gated L-type Ca^{2+} channels ($\text{Ca}_v1.2$). Ca^{2+} entry triggers the further release of Ca^{2+} from RyR2 channels in the sarcoplasmic reticulum (SR). Ca^{2+} diffuses through the cell and binds to myofilaments to trigger sarcomere contraction. Following contraction, Ca^{2+} is released from the myofilaments and is mostly pumped into the SR through SERCA2a . The remaining Ca^{2+} is extruded from the cell by NCX in exchange for Na^+ . Adopted with permission from (Luo & Anderson Mark, 2013).

In CMs, SERCA and NCX are responsible for the depletion of cytosolic Ca^{2+} following myofilament contraction (Fearnley et al., 2011). In rat ventricular CMs, 92% of Ca^{2+} efflux is carried out by SERCA2a , while NCX is responsible only for 7% of the efflux (Bers, 2002). While SERCA pumps cytosolic Ca^{2+} into SR, NCX facilitates the removal of Ca^{2+} from the cell. The decreasing $[\text{Ca}^{2+}]_i$ in the affected CMs with time must depend on an adaptation mechanism that either activates cellular Ca^{2+} efflux rates of underlying mechanisms in a time range of seconds or regulates Ca^{2+} flow through GJs. For the latter, gating mechanisms have been identified, as previously mentioned, that can cause uncoupling of GJs at high $[\text{Ca}^{2+}]_i$ (Peracchia, 2004). This suggests for a possible closure of GJs upon high $[\text{Ca}^{2+}]_i$ and thereby efflux of excess Ca^{2+} from CMs could have been achieved by enhanced activity of NCX . Unlike SERCA (high affinity-low volume), NCX (low affinity-high volume) responds quickly to

changes in intracellular $[Ca^{2+}]_i$ based on $[Ca^{2+}]_i$. Moreover, increased NCX activity had been reported in failing canine hearts for an increased $[Ca^{2+}]_i$. (Hobai Ion & O'Rourke, 2000; R. Wang, Wang, He, Sun, & Sun, 2020).

Besides these mechanisms, Ca^{2+} -dependent inactivation of L-type channels could possibly limit further Ca^{2+} entry in CMs affected by a high $[Ca^{2+}]_i$ as a negative feedback mechanism (Kubalová, 2003). RyR2 closure for high cytosolic $[Ca^{2+}]_i$ and opening for high (SR) luminal $[Ca^{2+}]_i$ had been previously described in CMs, which meant further release of Ca^{2+} from SR may not be possible (Laver, 2018). Taken together, it can be argued that NCX-mediated systematic efflux of Ca^{2+} regulates the restoration of $[Ca^{2+}]_i$ levels and hence contractility in the affected CMs. Further, the recovery of $[Ca^{2+}]_i$ levels and contractility in CMs suggested a recoverable stress level in connected CMs following single-cell death in cell clusters. Moreover, these Ca^{2+} regulatory mechanisms for increased $[Ca^{2+}]_i$ levels also suggest for adaptation in CMs that prevent further increase of $[Ca^{2+}]_i$. These mechanisms could explain the recovery of connected CMs over time following the single-cell ablation described in this work.

4.2 Cell culture systems enabled characterization of cell-specific responses to Ca^{2+}

Standard *in vitro* cardiac cell culture models do not accurately reproduce the *in vivo* structural organization of cardiac Fbs or their interrelation with CMs. Most cardiac cell cultures often try to restrict Fb content to enable the study of CMs in particular (Camelliti, Borg, & Kohl, 2005). In recent years, *in vitro* studies on myocardial physiology/pathophysiology have considered an essential role of Fbs in myocardial tissues (Archer et al., 2018; Cavallini & Tarantola, 2019; Rother et al., 2015). Moreover, it had been reported that in species such as rats, Fbs form the major fraction of cell population next to CMs (Banerjee et al., 2007). Therefore, the inclusion of Fbs in cell culture models is essential to make it comparable to native myocardial tissues. As native myocardial tissues are comprised of CMs as well as Fbs, ablation-induced changes in both these cell types were analyzed in detail in this study. In cocultures, the effect of single-cell ablation was different in CMs and Fbs. The difference in ablation-induced Ca^{2+} propagation, $[Ca^{2+}]_i$ -increase and $[Ca^{2+}]_i$ recovery in CMs and Fbs indicated a cell-type-specific regulation of Ca^{2+} in these cells. Hence, ablation experiments were performed in separate cell culture systems with a defined population of CMs and Fbs.

Freshly prepared myocardial cocultures from embryonic rats consisted of CMs as well as Fbs. The Fb fraction was generally higher than the CM fraction (59% Fbs vs. 41% CMs) (Fig. 3.3). The higher Fb content in these cultures could be explained by the proliferation of Fbs over

time. In the study from Banerjee et al. (Banerjee et al., 2007), it was reported that CMs constituted about 60% of the cell population in early neonatal rat hearts while Fbs constituted 30%. However, Fbs proliferated and formed more than 60% of the cell population on day 15, while the CM fraction was reduced to 30%, suggesting an overgrowth of Fbs over CMs with time. Thereby, the day three cocultures used in this thesis work, with numerous clusters of CMs surrounded by Fbs, were nearly comparable in cellular composition to myocardial tissues in mammalian hearts and were hence suitable for subsequent ablation experiments.

Although various cell separation techniques, based on size discrimination, centrifugal elutriation, or enzymatic digestion of the other tissue, were described, these techniques were time-consuming, not applicable to all cell types and, more importantly, stressful for the cells (Hersch et al., 2016). Especially with the primary cell isolation procedure that involved several enzymatic digestion and centrifugation steps, additional stressful steps could affect cell viability and functionality (Louch, Sheehan, & Wolska, 2011). Fusion-based biotinylation labeling of cells provided an advantage over antibody-based labeling as it was cell-type specific. Moreover, a cell viability of up to 80% could be obtained using this procedure (Hersch et al., 2016). Thereby membrane fusion using fusogenic-liposomes and subsequent magnetic labeling was ideally suited for the separation of CMs from the remaining myocardial cells.

In myocytes-enriched cultures, the mean fraction of CMs was found to be 64% (s.d. 15%). However, cultures with as high as 84% CMs were also obtained following cell-separation. The roughly one-third population of Fbs in these cultures is due to the proliferation of Fbs, resulting in an increased fraction over time. In myocytes-depleted cultures, the fraction of CMs was lower than in cocultures (32% (s.d. 24%)). In some myocytes-depleted cultures, more than 90% Fb fraction was found. The cross-contamination of CMs in myocytes-depleted cultures and Fbs in myocytes-enriched culture was undesirable as it might interfere with the functional analysis in homogeneous Fbs population. Analysis of fusion-efficiency with a shorter fusion time (< 2 min) and multiple elution steps could be useful to assess if purer cell populations could be obtained by the cell separation procedure. For ablation experiments in myocytes-depleted cultures, cell clusters predominantly containing Fbs were manually chosen. Similarly, in myocytes-enriched cultures, clusters containing predominantly CMs were used. In ablation experiments, CMs were distinguished from Fbs by the presence of calcium waves (refer Fig. 3.5 and supplementary movie 1) upon Fluo-4 labeling. The cell separation procedure thus enabled the characterization of ablation effects for CMs and Fbs in carefully chosen clusters with an almost homogeneous population of cells.

Comparison of $[Ca^{2+}]_i$ -increase showed a higher increase for CMs compared to the Fbs up to a distance of 140 μm from the ablated cell. Moreover, a significantly faster $[Ca^{2+}]_i$ -recovery was observed in Fbs compared to CMs for a distance of up to 100 μm from the ablated cell (Fig. 3.18 b). The difference in magnitude of $[Ca^{2+}]_i$ -increase and $[Ca^{2+}]_i$ recovery times in CMs and Fbs suggested a difference in Ca^{2+} handling in these cell types. Furthermore, a significantly higher Ca^{2+} propagation speed along Fbs compared to CMs across all culture systems indicated a difference in Ca^{2+} propagation mechanisms in these cell types.

4.3 Gap junctions mediated Ca^{2+} propagation in CMs but not in Fbs

In CMs, GJs play an important role in the intercellular transport of molecules up to 1 kDa, including Ca^{2+} , IP3 and other metabolites across cells (Kumar & Gilula, 1996). GJs are essential for the propagation of cardiac action potential and synchronous contraction of CMs (Rohr, 2004). Therefore, immunocytochemical analysis was performed to identify the presence of GJ proteins that could facilitate ablation-induced Ca^{2+} flow between connected cells. Immunocytochemical analysis identified Cx43, the most prominent gap junction protein isoform in mammalian hearts (N. J. Severs et al., 2008), between CMs in cocultures as well as myocytes-enriched cultures (Fig. 3.32). Besides Cx43, two other isoforms of connexin protein were previously identified in myocardial tissues - connexin40 (Cx40) and connexin45 (Cx45), which have different spatial and temporal expression patterns and show variations in conductance (Desplantez, 2017; Gros & Jongsma, 1996; Kanno & Saffitz, 2001). However, findings from immunocytochemical analysis in this thesis work showed the presence of only Cx43, but not Cx40 and Cx45, between CMs.

Cx40 and Cx45 have been shown to be regulated developmentally in the heart. While Cx43 is abundantly found in the atrium, ventricle, and distal His-purkinje system, Cx40 is found in the atrial and His-purkinje system and Cx45 is found in sinoatrial and atrioventricular nodes in adult hearts. Previous studies had shown that Cx40 and Cx45 are expressed in cardiac morphogenesis but are downregulated later (Alcoléa et al., 1999; Kanno & Saffitz, 2001). Further, in cultured rat CMs, Cx43 was found at early stages of culture, whereas Cx45 was downregulated at early stages, and the expression levels were enhanced at later stages (later than two weeks) (Polontchouk, Valiunas, Haefliger, Eppenberger, & Weingart, 2002). The presence of Cx43 in GJs but an absence of Cx40 and Cx45 in this work could therefore be explained by the developmental stage of the rat hearts used. Since the ablation experiments were performed in cells from E18/19 embryonic stage rat hearts, analysis of connexins in rats

at a different developmental stage was not performed. Moreover, Ca^{2+} flow through Cx43-based GJs has been shown previously (C. Li et al., 2012), but the role of Cx40 and Cx45 in Ca^{2+} diffusion is still not clear. In addition to the observations from sequential Ca^{2+} transfer between connected CMs, the presence of Cx43 plaques at cell-cell contacts between adjacent CMs strongly argued for a flow of Ca^{2+} through Cx43-based GJs in connected CMs upon ablation.

To confirm the presence of GJ-based Ca^{2+} propagation in cells, the endocrine disruptor ioxynil octanoate (IO) was added to the Fluo-4 labeled coculture cells. Ioxynil octanoate has been previously shown to inhibit Cx43-based GJ formation between rat liver epithelial cells (IAR20 cell line) (Leithe, Kjenseth, Bruun, Sirnes, & Rivedal, 2010). Due to the low aqueous solubility of IO, the specific effects of the compound on cells could not be studied. Moreover, the presence of dimethylsulfoxide (DMSO) affected cell functionality when incubated for one hour. DMSO was shown to affect cell functionality over time (refer supplementary figure 1) (Verheijen et al., 2019). Thereby clear conclusions could not be drawn whether the Cx43-inhibitor had an effect on the GJ communication between these cells. Several blockers of GJ channels have been described so far particularly targeting the heart and the brain (Dhein, 2004; Manjarrez-Marmolejo & Franco-Pérez, 2016). However, pharmacological blocking of cardiac GJs is affected by the lack of complete understanding of the specificity of the compounds used and the pathways involved (Dhein, 2004).

Of note, gap junction plaques (Cx40, Cx43, and Cx45) were not found in cultured Fbs (Fig. 3.33). Western blot analysis of proteins from embryonic rat heart tissue and fibroblasts-overgrown cultures detected a band at ~ 50 kDa when labeled with a monoclonal anti-Cx43 antibody. The shift in band size could be explained by the phosphorylation of the protein (Jeyaraman et al., 2012). Detection of Cx43 in western blot analysis could be due to the presence of CMs in fibroblasts-overgrown cultures. However, immunocytochemical analysis of day 3 coculture of CMs and Fbs with the same antibody could not specifically detect Cx43-based gap junction plaques at cell-cell contacts between CMs or between Fbs (refer Fig. 3.33). Immunocytochemical analysis using a polyclonal antibody against Cx43 could detect gap junction plaques between CMs but not between Fbs or between CMs and Fbs (Fig. 3.36).

Previous research has shown the expression of connexin proteins (Cx40, Cx43 and Cx45) in cardiac Fbs in tissues as well as cultured cells. The presence of these connexins was detected in different animal species, including mouse, rat, sheep and rabbit. More importantly, the

presence of functional gap junctions between cardiac Fbs and CMs as well as between Fbs were described (Johnson & Camelliti, 2018). However, most of these analyses were performed in Fbs from adult, neonatal or pathological hearts. The presence of functional connexin-based GJs in prenatal or embryonic cardiac Fbs is not clear. In this study, immunocytochemical analysis could not detect the presence of all three connexins in embryonic rat Fbs in young (3 days) and old cultures (14 days). The absence of connexin-based GJs in Fbs in this work could be due to the developmental stage of the animal used (prenatal) or different phenotypes of Fbs (normal vs pathological) to those described in the fore-mentioned studies.

4.4 Ca²⁺ propagation and handling in fibroblasts

The absence of GJ plaques between Fb-Fb and CM-Fb pairs and faster and almost constant Ca²⁺ propagation speeds for longer distances (200 µm) in Fbs compared to CMs suggested an indirect mode of Ca²⁺ propagation in Fbs as opposed to the direct flow observed in CMs. Previously electrotonic interaction between CMs and Fbs had been observed (Kohl & Noble, 1996) and such an interaction could serve as the basis for the connectivity between CMs and Fbs in this study. Moreover, previous studies have reported an electrotonic modulation of impulse conduction in CMs by myofibroblasts (Miragoli, Gaudesius, & Rohr, 2006). Further, it had been reported that Fbs are capable of synchronizing contraction among individual CMs and that these contractions are accompanied by synchronous membrane potential fluctuations in the interconnecting Fbs (Gaudesius et al., 2003). In intact tissue, evidence has been presented that mechanosensitive Fbs in the sinoatrial region are electrically coupled to atrial CMs (Kohl & Gourdie, 2014). Based on these evidences, it is possible that ablation-induced changes in membrane potential could be propagated along the surrounding Fbs, which could trigger Ca²⁺ entry through Ca²⁺-permeable channels.

It had been previously reported that in contrast to CMs, Fbs lack functional L-type Ca²⁺ channels, which facilitate a voltage-gated Ca²⁺ entry (Kohl & Noble, 1996). Therefore, changes in membrane potential in Fbs might depend on an alternative mechanism that could facilitate Ca²⁺ entry through other channels. In Fbs, both external Ca²⁺ entry and intracellular Ca²⁺ release (from ER) mechanisms have been described previously (Feng et al., 2019). For example, ATP-activated Ca²⁺-permeable non-selective cation channels called Purinergic receptors (P2XRs) have been identified in cardiac Fbs. The non-selective cation permeation of P2XRs not only brings Ca²⁺ into the cells but also causes depolarization (Surprenant & North, 2009). Among different isoforms, P2X4 and P2X7 receptors mRNAs were found in cultured

human ventricular Fbs. However, expression and the function of these channels in spontaneously mediating Ca^{2+} entry in cardiac Fbs needs further investigation (Feng et al., 2019).

The transient receptor potential (TRP) channels present a possible mechanism of non-selective Ca^{2+} entry in Fbs. The TRPs belong to a superfamily of non-voltage-gated Ca^{2+} -permeable ion channels (Clapham, 2003; Venkatachalam & Montell, 2007). TRP channels are responsive to a wide range of stimuli, including thermal, mechanical, oxidative, chemical, and nociceptive stresses, and local autocrine or paracrine environmental cues (Feng et al., 2019). TRP channels contribute to Ca^{2+} homeostasis by directly conducting Ca^{2+} or indirectly via membrane depolarization and modulation of voltage-gated Ca^{2+} channels (Falcón et al., 2019). Many TRP channel genes have been detected at the RNA level by qPCR or RT-PCR in isolated rat Fbs, cultured human cardiac Fbs, freshly isolated human atrial Fbs and isolated mouse cardiac Fbs (Yue, Xie, & Nattel, 2011). Recently, TRPM7 mediated Ca^{2+} signaling had been reported to be involved in TGF- β 1-elicited fibrosis in human atrial fibrillation, which suggests for a role of TRP channels in Ca^{2+} signaling in cardiac Fbs (Du et al., 2010).

Although TRP channels are not voltage-gated channels, some evidence showed that these channels are weakly sensitive to membrane potentials under non-physiological conditions and in combination with other stimuli (Zheng, 2013). Further, key components of the Ca^{2+} release-activated Ca^{2+} channel (CRAC) have been found in cardiac Fbs. The molecular components of CRAC channels consist of the pore-forming subunit Orai and the Ca^{2+} release-sensing subunit STIM (Nguyen et al., 2018). The CRAC mechanism is regulated by Ca^{2+} depletion from the stores, which triggers Ca^{2+} entry into cells. In other cell types, TRP channels and STIM/ORAI proteins rely on the activity of K^+ channels that hyperpolarize the cell membrane potential in order to maintain the electrochemical driving force for Ca^{2+} entry (N. Nielsen, Lindemann, & Schwab, 2014). Of note, voltage-gated K^+ channels have been found in cardiac Fbs (Walsh & Zhang, 2008). These mechanisms suggest a Ca^{2+} propagation in cardiac Fbs through membrane potential changes following ablation that regulate voltage-gated ion channels (e.g., K^+ channels) that indirectly facilitate Ca^{2+} entry through the TRP channels.

The sharp $[\text{Ca}^{2+}]_i$ spike and faster $[\text{Ca}^{2+}]_i$ recovery (< 1 min) observed in Fbs following ablation in this work indicated that Ca^{2+} efflux was instantaneous in these cells. The transient $[\text{Ca}^{2+}]_i$ increase in Fbs compared to a sustained increase in CMs could be due to the difference of Ca^{2+} handling. In CMs, the myofilaments act as a buffer of Ca^{2+} while Fbs lack these myofilaments.

In human ventricular Fbs, the mRNA expression of NCX and SERCA has been detected. These channels could represent the Ca^{2+} efflux mechanisms in Fbs (J. B. Chen et al., 2010; Feng et al., 2019). A relatively less regulated Ca^{2+} efflux can also occur through plasma membrane calcium ATPase (PMCA). In recent years, it has been demonstrated that PMCA4 plays a significant role in the regulation of signal transduction in the heart. Among the four PMCA (PMCA1 – 4), PMCA4 has been shown to be involved in cardiac Fb-regulated CM hypertrophy through a paracrine mechanism. Further, it was shown that the basal Ca^{2+} level in PMCA4 knock-out Fbs was 25% higher than that in control Fbs, indicating that PMCA could regulate Ca^{2+} efflux in cardiac Fbs (Mohamed et al., 2016). The above described Ca^{2+} regulatory proteins/channels and the absence of myofilaments that buffer cytosolic Ca^{2+} together present the possible mechanisms underlying the rapid recovery of $[\text{Ca}^{2+}]_i$ in Fbs.

In this study, cell death in myocardial cell clusters clearly illustrated a connectivity between the cells. However, the functional relevance of this connectivity between CMs and Fbs in myocardial tissues needed further investigation. The role of Fbs in Ca^{2+} signaling in myocardial clusters was studied by the patterned growth of CMs and Fbs using culture inserts (Fig. 3.21). The Ca^{2+} waves in CM clusters separated by a distance of about 500 μm from each other were found to be synchronized (refer supplementary movie 8) indicating a possible Fbs-mediated coupling of Ca^{2+} waves between CM clusters. Moreover, ablation of a single CM on one cluster was followed by a delayed contraction in the CM cluster on the other end of the fibroblast-bridge. Although only a minor delay in contraction was found in the other cluster upon ablation, long-distance impacts of single-cell death observed in this analysis suggested a possible functional coupling of CMs by Fbs. This finding supports the previously described electrotonic coupling of CMs and Fbs in the heart (Quinn et al., 2016) and further indicates the possibility of functional significance of CM-Fb interactions i.e., synchronizing CM activity.

4.5 Functional significance of Ca^{2+} signals in cardiomyocytes and fibroblasts

Short-term analysis of contractile recovery behavior showed half-recovery of contractile amplitudes in CMs from cocultures and myocytes-enriched cultures. In most experiments, contractile half-recovery could not be observed in CMs within 40 μm from the ablated cell. Moreover, long-term analysis of ablation-induced $[\text{Ca}^{2+}]_i$ -changes in coculture for an extended duration showed a lack of complete recovery in closely connected cells (located 40 μm from the ablated cell) after ~ 25 mins post ablation (refer Fig. 3.25), which suggested that these cells may be permanently/irreversibly affected by the high Ca^{2+} inflow. In addition to the observed

effects of high $[Ca^{2+}]_i$, retraction of membranes in CMs in the cluster due to a high contracture further underlines the detrimental effects of increased $[Ca^{2+}]_i$ on CMs (refer supplementary movie 9).

In order to estimate the impact of enhanced $[Ca^{2+}]_i$ on CM contractility, traction force analysis was performed. Traction force analysis required high spatial resolution to accurately track bead displacements while maintaining an appropriate temporal resolution to capture individual contractions in cells. Thereby, traction force-changes could be measured only for smaller clusters ($\sim 100 \mu\text{m}$ radius) of CMs. Moreover, the presence of DMSO in the Fluo-4 limited the long-term measurement of forces as exposure to DMSO affected CMs contractility from 3-6 hours after loading of dye even at 0.25% final concentration (refer supplementary Fig. 1). Traction force analysis for short durations clearly showed the prolonged high contracture in CMs with increased $[Ca^{2+}]_i$ and interrupted contractility. Only with a decrease in $[Ca^{2+}]_i$, contractility was restored in CMs. Comparing Ca^{2+} changes with traction force-changes over time in CMs showed a similar temporal pattern after ablation. From these results, a clear link between increased $[Ca^{2+}]_i$ levels and contractility was confirmed for CMs surrounding the ablated cell. $[Ca^{2+}]_i$ -increase signaled a briefly disrupted contractility in connected CMs.

Since Ca^{2+} plays a central role in E-C coupling, strict regulation of Ca^{2+} handling is essential in CMs. The Ca^{2+} transport mechanisms include Ca^{2+} cycling between cytosol and extracellular space as well as between cytosol and intracellular stores. These mechanisms tightly regulate cytosolic $[Ca^{2+}]$ levels in CMs as change in cytosolic $[Ca^{2+}]$ levels can influence the $[Ca^{2+}]$ levels in the nucleus, SR and mitochondria. Ca^{2+} is also involved in transcriptional regulation through signaling pathways regulated by proteins such as calmodulin, calcineurin, CamKII and calpain. Further, Ca^{2+} , when locally enhanced in nuclear microdomains, might bind to a very specific region of the DNA and recruit Ca^{2+} -dependent enzymes to spatially modify chromatin structure and potentially influence transcription (Dewenter et al., 2017).

Further, Ca^{2+} overload is a characteristic feature of myocardial injury. If the cytoplasm is Ca^{2+} -overloaded, the mitochondria take up Ca^{2+} at the expense of oxidative phosphorylation (Santulli, Xie, Reiken, & Marks, 2015; Vassalle & Lin, 2004). Moreover, high levels of $[Ca^{2+}]$ could cause mitochondrial swelling and dysfunction that underlies or contributes to cell death (Williams, Boyman, & Lederer, 2015). Mitochondrial damage is regarded as a sign of myocardial cell transformation from reversible to irreversible damage (Williams et al., 2015). Increased intracellular $[Ca^{2+}]$ can also activate some phospholipases such as protein kinase C

and phospholipase A that destroy cell membrane skeleton (Putney & Tomita, 2012; R. Wang et al., 2020). Due to their role in $[Ca^{2+}]_i$ regulation, Ca^{2+} channels in CMs have been a common pharmacological target for acute myocardial conditions as well as chronic cardiomyopathies. By regulating Ca^{2+} channels, some of these drugs prevent contractile dysfunction in the heart (R. Wang et al., 2020). These mechanisms underline the pharmacological significance of Ca^{2+} signals and disrupted $[Ca^{2+}]_i$ homeostasis in the heart. The presence of Ca^{2+} regulatory mechanisms that actively extrudes Ca^{2+} represents the adaptation of CMs that could prevent Ca^{2+} overload and associated damage in these cells.

In this study, ablation of single cell resulted in at least 2-fold increase in surrounding Fbs. However, during the short experimental time-frame it was unclear if increased $[Ca^{2+}]_i$ had an impact on the Fb functionality. In the native heart, fibrosis is an important feature of various pathologies including arrhythmia, hypertrophy and heart failure (Feng et al., 2019). The differentiation of Fbs to myofibroblasts is an important step in fibrosis as myofibroblasts are predominant cell type that secrete ECM proteins. A variety of pathological stimuli including myocardial injury, oxidative stress and inflammatory stimuli have been associated with fibrogenesis. Among other signaling mechanisms, Ca^{2+} signaling has also been associated with cardiac fibrogenesis. $[Ca^{2+}]_i$ can activate pathways that promote pro-fibrotic gene expression (Feng et al., 2019). As mentioned earlier, Ca^{2+} signals mediated by TRPM7 channel were previously reported to confer with fibrogenesis in human atrial fibrillation (Du et al., 2010). Investigating Fb proliferation and differentiation to myofibroblasts can provide clues about the effect of observed ablation-induced Ca^{2+} signals in Fbs.

The membrane potential changes that represent a possible mechanism of Ca^{2+} propagation in Fbs could be measured using electrophysiological methods like whole-cell patch-clamp in current clamp mode and microelectrode array (MEA) (G.-R. Li et al., 2009; Natarajan et al., 2011). However, due to the difficulty in combining the patch clamp and confocal microscopy in one setup as well as possible experimental difficulty (e.g. in forming high-resistance gigaseal to reliably measure membrane potential changes), the technique was not performed in this study. Although MEA could be used to study membrane potential changes in cultured cells, this method could not be used in combination with laser ablation.

Since non-selective Ca^{2+} entry through TRP channels have been described to be essential for Ca^{2+} signaling in cardiac Fbs, detection of TRP channel genes and knock out of these genes or blocking these channels using chemical blockers could reveal the involvement of these

channels in Ca^{2+} propagation (Falcón et al., 2019; Feng et al., 2019; Moran, McAlexander, Bíró, & Szallasi, 2011). Given the importance of Ca^{2+} signaling in cardiac Fbs in the context of fibrogenesis, identifying the Ca^{2+} signaling mechanisms could be useful for a better understanding of fibrosis-associated cardiac pathologies.

Chapter 5 Conclusion and Outlook

This research work focuses on the characterization of the impact of cell death on connected cells in myocardial cell clusters. The findings from this research work illustrate the spontaneous response of connected cells in clusters to single cell-death based on intracellular Ca^{2+} concentrations ($[\text{Ca}^{2+}]_i$). Laser-induced single cell-death resulted in an increased $[\text{Ca}^{2+}]_i$, which briefly affected the contractile force and contractility of connected cardiomyocytes (CMs). The contractility recovered with decreasing $[\text{Ca}^{2+}]_i$ in a time scale of few minutes, suggesting an adaptation of CMs that rapidly extrudes excess Ca^{2+} from the cells. Moreover, the recovery of contractility in connected CMs also suggested recoverable stress levels in these cells following a single-cell death in myocardial cell clusters. Besides these effects of Ca^{2+} propagation along connected CMs, Ca^{2+} propagation was also observed along fibroblasts (Fbs). Whereas the $[\text{Ca}^{2+}]_i$ -increase after ablation was slow and sustained in CMs, in Fbs, a transient spike in $[\text{Ca}^{2+}]_i$ was observed following the death of a single CM or Fb in cell clusters. This suggested a difference in Ca^{2+} handling and propagation mechanisms in CMs and Fbs. Further, it was observed that Fbs between CM clusters could couple the activity of CMs, which indicated functional connectivity between CMs and Fbs.

Analysis of Ca^{2+} propagation in CMs showed a direct flow of Ca^{2+} between adjacent CMs and the presence of gap junction plaques that argued for a gap junction-based diffusion of Ca^{2+} upon ablation. In Fbs, gap junction plaques could not be detected from the immunocytochemical analysis. The absence of gap junction plaques together with a comparatively faster and almost constant Ca^{2+} propagation speed for a distance of 200 μm suggested a putative membrane potential-mediated Ca^{2+} propagation in connected Fbs triggered by the laser-induced death of a connected cell.

In CMs, the entry of Ca^{2+} is facilitated by voltage-gated L-type calcium channels. Whereas Fbs lack voltage-gated Ca^{2+} channels. Therefore, Ca^{2+} propagation in these cells must depend on an alternative mechanism that could only be speculated at this point. In cardiac Fbs, non-selective ion channels and store-operated ion channels have been identified. These channels may facilitate Ca^{2+} entry by the influence of other voltage-gated channels, such as the K^+ channels, which could sense membrane potential changes following ablation. Among the various Ca^{2+} channels, the transient receptor potential (TRP) channels and effectors of store-operated Ca^{2+} -entry – the stromal interaction molecule (STIM) and Orai channels have been shown to be involved in Ca^{2+} signaling in cardiac Fbs. Given that TRP channels were

previously reported to be involved in Ca^{2+} signaling in cardiac Fbs, analyzing the expression of TRP channels and blocking them can be the first steps to validate the presence of these channels in cardiac Fbs and their possible role in Ca^{2+} signaling.

The increased $[\text{Ca}^{2+}]_i$ could signal various functions in cells. In CMs, the increased $[\text{Ca}^{2+}]_i$ had an immediate impact on contractility. The contractility recovered with decreasing $[\text{Ca}^{2+}]_i$ over time. To understand the impact of these Ca^{2+} signals on cell functionality further, long-term analysis of the affected cells is required. Long-term analysis of the CMs affected by a high $[\text{Ca}^{2+}]_i$ could reveal whether the affected cells survive or are irreversibly damaged. In Fbs, the signaling potential of the observed $[\text{Ca}^{2+}]_i$ -spike could not be studied from the short-term analyses performed in this study. Previously Ca^{2+} signals have been reported to promote fibrogenesis, which suggests the possible role of these signals to initiate the fibrogenesis pathway. Therefore, analyzing Fb proliferation and differentiation to myofibroblasts using myofibroblasts marker such as α -smooth muscle actin (α -SMA) could be useful in this context. However, such long-term analyses should also consider the detrimental effects of dimethyl sulfoxide in the Ca^{2+} indicator and the radicals released during ablation.

The synchronization of contractility between CMs clusters separated by Fbs and delayed contraction in CM cluster at one end upon ablation in the cluster at the other end suggested that Fbs are involved in functional coupling of CMs. These findings support previous studies that describe electrotonic interaction between CMs and Fbs and electrical coupling of CMs by Fbs. The presence of mechanisms that enable coupling of CM activity as well as the spread of cell death signals across long distances could therefore describe an essential role of Fbs in signaling in myocardial tissues.

Overall, this thesis work characterizes the response of myocardial cells to single-cell injury, adaptation of connected CMs, underlying signaling mechanisms and functional interconnectivity in myocardial cells. These findings will provide a better understanding of the impact of an injury in myocardial tissues and adaptations in cells that could possibly restore the function of the affected tissues. Further, this work also illustrates the functional connectivity between cardiomyocytes and fibroblasts in myocardial cell cultures.

Supplementary results

Supplementary movie 1: Ca²⁺ waves in Fluo-4 labelled coculture cells: Time-series showing Ca²⁺ waves in coculture cells labelled with Fluo-4 Ca²⁺ indicator. Rhythmic and synchronized Ca²⁺ waves can be observed in myocytes in the cluster.

Supplementary movie 2: Ca²⁺ waves in myocytes-enriched culture cells: Time-series showing Ca²⁺ waves in a cluster of myocytes in myocytes-enriched culture. Synchronized contractions can be observed from Ca²⁺ waves in myocyte clusters

Supplementary movie 3: Ca²⁺ waves in cells of myocytes-depleted culture: Time-series showing Ca²⁺ oscillations in non-myocytes in myocytes-depleted culture. Unlike myocytes, Ca²⁺ oscillations were minimal in fibroblast clusters.

Supplementary movie 4: Ablation-induced Ca²⁺ propagation in coculture cardiomyocytes: a) Time-series showing Ca²⁺ propagating along the myocytes upon ablation of a single myocyte. The ablated myocyte is indicated by red circle. An increase in Ca²⁺ can be seen in connected myocytes after ablation (t = 0 s). Distant cells are little or not affected by ablation, as indicated by continuing Ca²⁺ waves even after ablation. Ca²⁺ intensity values of closely connected myocytes return to values identical to intensity values before ablation. b) Phase-contrast time-series images showing disruption of target cell (red circle) after ablation. (Sridhar et al., 2020)

Supplementary movie 5: Ablation-induced Ca²⁺ propagation in non-myocytes in cocultures: Time-series showing Ca²⁺ propagating along the non-myocytes upon ablation of single-central myocyte. The ablated myocyte is indicated by red circle. A spike in Ca²⁺ can be seen after ablation (t = 0 s), after which the Ca²⁺ intensity drops to values values identical to intensity before ablation. (Sridhar et al., 2020)

Supplementary movie 6: Ablation-induced Ca²⁺ propagation in cardiomyocytes in myocytes-enriched cultures: Time-series showing changes in Ca²⁺ with time in myocytes-enriched cultures before and after ablation (t = 0 s). Ablation resulted in sustained increase in [Ca²⁺]_i in surrounding myocytes. Ca²⁺ values returned to values identical to pre-ablation values with time.

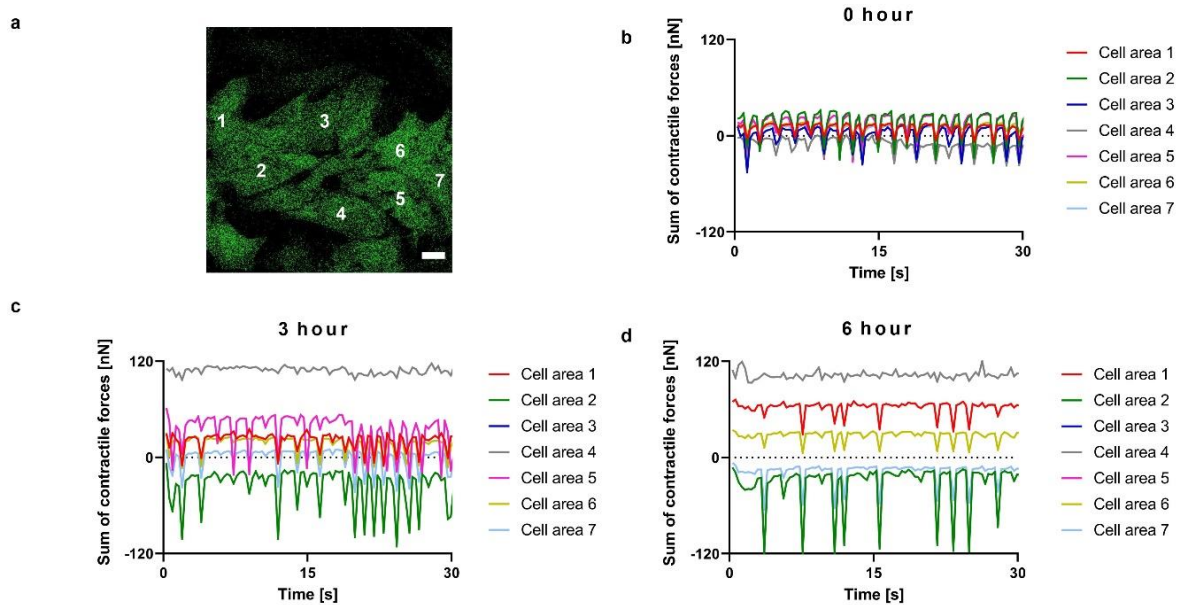
Supplementary movie 7: Ablation-induced Ca²⁺ propagation in non-myocytes in myocytes-depleted cultures: Time-series showing changes in Ca²⁺ fluorescence intensity with time, before and after ablation (t = 0 s). Ablation of single fibroblast resulted in a spike in [Ca²⁺]_i in surrounding fibroblasts. Ca²⁺ intensity values returned to initial levels within a short period of time post ablation. (Sridhar et al., 2020)

Supplementary movie 8: Ca²⁺-changes in myocyte and non-myocyte clusters after removal of culture insert: Time-series images showing Ca²⁺ changes in Fluo-4 labelled cell clusters before and after ablation. Ca²⁺ waves were seen in contracting myocyte clusters (marked by white circles) on either end separated by a distance of 500 μm. Fibroblasts between myocyte clusters can be seen having minimal Ca²⁺ oscillations. Ablation of a myocyte (red) in one cluster (left) resulted in Ca²⁺ increase in surrounding myocytes with time. Ablation briefly affected myocyte contractility in the other cluster (right).

Supplementary movie 9: Ablation-induced changes in surrounding cardiomyocytes in cluster: $[Ca^{2+}]_i$ -increase in connected cells after ablation is accompanied by membrane retraction in connected cells of the cluster. The ablated region is indicated by red circle and the retraction of cells in the cluster is indicated by arrows. The time point of ablation is set to $t = 0$ s. (Sridhar et al., 2020)

Supplementary movie 10: Effect of ablation of cardiomyocytes on soft elastomeric substrates with covalently-coupled fluorescent microbeads: a) Time-series showing Ca^{2+} changes in myocytes in enriched cultures on soft substrates ($E = 15$ kPa) before and after ablation. The ablated cell is marked in red and time point of ablation is set to $t = 0$ s. Ablation resulted in an increased $[Ca^{2+}]_i$ in surrounding myocytes with Ca^{2+} levels being restored with time. Phase contrast (b) and bead channels (c) show loss of contractility in surrounding cardiomyocytes following ablation as cells remained in contracted state until $[Ca^{2+}]_i$ levels decreased. Contractility reappeared in cells with time.

Supplementary movie 11: Time-series showing sequential diffusion of Ca^{2+} across connected cardiomyocytes: Ablation-induced diffusion of Ca^{2+} across Fluo-4 labelled cardiomyocytes through cell-cell contacts. Ablated region is indicated by red circle and the time point of ablation is set to $t = 0$ s. Ca^{2+} sequentially diffuses across the three connected cells in about 2 s from the time point of ablation. The closely connected myocyte exhibited rapid intracellular Ca^{2+} oscillations with time. (Sridhar et al., 2020)



Supplementary figure 1: Long-term effect of dimethyl sulfoxide on cardiomyocytes activity:

a) Fluo-4 labelled cardiomyocytes in a myocytes-enriched cluster cultured on soft ($E = 15$ kPa) bead-coupled substrates. The cell areas for analysis of traction force-changes over time is marked (Cell area 1 – 7). Scale bar: $20\ \mu\text{m}$. After addition of Fluo-4 AM indicator, the cells were imaged for ~ 30 s after 3 hours and 6 hours to examine the long-term effects of the dye on cells while preventing phototoxicity as much as possible by reducing the imaging time. **b)** Plot of contractile force-changes for cell areas marked in (a) with time showing rhythmic and synchronized peaks. Since the contracted state of the cells were taken as the reference image in this example, the inverted peaks represent relaxation of cardiomyocytes. **c)** Plot of contractile force-changes with time 3 hours after addition of the $5\ \mu\text{M}$ Fluo-4 AM indicator. The indicator consisted of 0.5% (v/v) dimethyl sulfoxide (DMSO). The contractility of the cells were affected as seen from the irregular peaks and no peak (Cell area 4) as well as loss of synchronous contractions. **d)** Plot of contractile force-changes 6 hours post addition of the Fluo-4 AM indicator. The contractility in cells were perturbed as seen from the loss of rhythmic and synchronous peaks compared to (a).

Abbreviations

[Ca²⁺]_i – Intracellular calcium concentration

μg – microgram

μJ – microjoule

μl – microliter

μm – micrometer

μM – micromolar

ADP – adenosine diphosphate

AF – Atrial fibrillation

AJ – adherens junction

AM ester – acetoxymethyl ester

AP – Action potential

ATP – adenosine triphosphate

ATPase - adenosinetriphosphatase

au – Arbitrary units of fluorescence intensity

AVN – Atrioventricular node

BM – Basement membrane

CAD – Coronary artery disease

CaM – calmodulin

CB – Cytoskeletal buffer

CICR – Calcium-induced calcium release

CM – Cardiomyocyte

CNS – Central nervous system

CO₂ – carbon dioxide

CRAC – Calcium release-activated channel

CVD – Cardiovascular disease

Cx – connexin

Cx40 – connexin40

Cx43 – connexin43

Cx45 – connexin45

Cy3 – cyanine 3
DAG complex - dystrophin-associated glycoprotein complex
DAMP – Danger-associated molecular pattern
DDR2 – discoidin domain-containing receptor 2
DES - desmin
DiR – 1,10-dioctadecyl-3,3,30,30-tetramethylindotricarbocyanine iodide
DISC – Death induced signaling complex
DMEM – Dulbecco’s minimum essential medium
DMSO – dimethyl sulfoxide
DNA – deoxyribonucleic acid
DNAse – deoxyribonuclease
DOPE – 1,2-dioleoyl-sn-glycero-3-phosphoethanolamine
DOTAP – 1,2-dioleoyl-3-trimethylammonium-propane
DPSS – Diode-pumped solid-state laser
DSC – desmocollin
DSG – desmoglein
DSP – desmoplakin
DVF – Displacement vector field
EBSS – Earl’s balanced salt solution
EC – Endothelial cell
E-C coupling – Excitation-contraction coupling
ECM – Extracellular matrix
EDTA – ethylenediaminetetraacetic acid
EGTA – ethylene glycol-bis(β -aminoethyl ether)-N,N,N',N'-tetraacetic acid
ER – Endoplasmic reticulum
Fb – Fibroblast
FBS – Fetal bovine serum
FL – Fusogenic liposome
 F_{\max} – maximum fluorescence intensity
 F_{\min} – minimum fluorescence intensity
FRAP – Fluorescence recovery after photobleaching
GFM – Generalized first moment

GJ – Gap junction
HBSS – Hank’s balanced salt solution
HCl – hydrochloric acid
HEPES – 4-(2-hydroxyethyl)-1-piperazineethanesulfonic acid
HF – Heart failure
HNX – H⁺-Na⁺ exchanger
Hz – hertz
I/R – Ischemia/Reperfusion
ICD – Intercalated disc
IF – Intermediate filament
IL – interleukin
IMM – inner mitochondrial membrane
IO – ioxynil octanoate
IP3 - 1,4,5-trisphosphate
IP3R - 1,4,5-trisphosphate receptor
iPSC – induced pluripotent stem cells
ITS – insulin-transferrin-selenium
kDa – kilodalton
kHz – kilohertz
kPa – kilopascal
L – liter
LSM – Laser scanning microscope
LTCC – L-type calcium channel
LV – Left ventricle
MEA – Microelectrode array
MES – 2-(4-morpholino)ethanesulfonic acid
MgCl₂ – magnesium chloride
MI – Myocardial infarction
MI/R – Myocardial Ischemia/Reperfusion
mL – milliliter
mm – millimeter
mM – millimolar

MPT – Mitochondrial pore transition
mPTP – Mitochondrial permeability transition pore
mV – millivolt
MW – Molecular weight
NA – Numerical aperture
NaCl – sodium chloride
NaOH – sodium hydroxide
NCX – sodium (Na⁺)-calcium(Ca²⁺) exchanger
nJ – nanojoule
nm - nanometre
nN – nanonewton
ns - nanosecond
OMM – Outer mitochondrial membrane
PBS – phosphate buffered saline
PDMS – polydimethylsiloxane
PKA – protein kinase A
PKC – protein kinase C
PKG – plakoglobin
PKP – plakophilin
PMCA – Plasma membrane calcium ATPase
PMT – Photomultiplier tube
px – pixel
qPCR – Quantitative polymerase chain reaction
RGB – Red, green, blue color model
RIPA – radioimmunoprecipitation assay
RNA – ribonucleic acid
ROS – reactive oxygen species
rpm – revolutions per minute
RT – Room temperature
RT-PCR – reverse transcriptase-polymerase chain reaction
RyR – ryanodine receptor
s - second

SAN – Sinoatrial node
SDS – sodium dodecyl sulfate
SERCA – Sarcoplasmic/endoplasmic reticulum calcium ATPase
SF – stress fiber
SMC – Smooth muscle cell
SOCE – Store-operated calcium entry
SR – Sarcoplasmic reticulum
STIM – stromal interaction molecule
TGF – tumor growth factor
TLR – toll-like receptor
TnC – troponin C
TNF – tumor necrosis factor
TnI – troponin I
TnT – troponin T
TRP – Transient receptor potential
UV – Ultraviolet
V - Volt
VDF – Vector displacement field
VOCC – Voltage-operated calcium channels
 α -SMA – alpha-smooth muscle actin

Bibliography

- Alcoléa, S., Théveniau-Ruissy, M., Jarry-Guichard, T., Marics, I., Tzouanacou, E., Chauvin, J.-P., . . . Gros Daniel, B. (1999). Downregulation of Connexin 45 Gene Products During Mouse Heart Development. *Circulation Research*, 84(12), 1365-1379. doi:10.1161/01.RES.84.12.1365
- Ali, H., Braga, L., & Giacca, M. (2020). Cardiac regeneration and remodelling of the cardiomyocyte cytoarchitecture. *The FEBS Journal*, 287(3), 417-438. doi:https://doi.org/10.1111/febs.15146
- Archer, C. R., Sargeant, R., Basak, J., Pilling, J., Barnes, J. R., & Pointon, A. (2018). Characterization and Validation of a Human 3D Cardiac Microtissue for the Assessment of Changes in Cardiac Pathology. *Scientific Reports*, 8(1), 10160. doi:10.1038/s41598-018-28393-y
- Ariyasinghe, N. R., Lyra-Leite, D. M., & McCain, M. L. (2018). Engineering cardiac microphysiological systems to model pathological extracellular matrix remodeling *Am J Physiol Heart Circ Physiol* (Vol. 315, pp. H771-789).
- Arrigo, M., Parissis, J. T., Akiyama, E., & Mebazaa, A. (2016). Understanding acute heart failure: pathophysiology and diagnosis. *European Heart Journal Supplements*, 18(suppl_G), G11-G18. doi:10.1093/eurheartj/suw044
- Bagur, R., & Hajnóczky, G. (2017). Intracellular Ca(2+) Sensing: Its Role in Calcium Homeostasis and Signaling. *Molecular cell*, 66(6), 780-788. doi:10.1016/j.molcel.2017.05.028
- Banerjee, I., Fuseler, J. W., Price, R. L., Borg, T. K., & Baudino, T. A. (2007). Determination of cell types and numbers during cardiac development in the neonatal and adult rat and mouse. *Am J Physiol Heart Circ Physiol*, 293(3), H1883-1891. doi:10.1152/ajpheart.00514.2007
- Baruscotti, M., Barbuti, A., & Bucchi, A. (2010). The cardiac pacemaker current. *J Mol Cell Cardiol*, 48(1), 55-64. doi:10.1016/j.yjmcc.2009.06.019
- Baruscotti, M., Bucchi, A., & DiFrancesco, D. (2005). Physiology and pharmacology of the cardiac pacemaker (“funny”) current. *Pharmacology & Therapeutics*, 107(1), 59-79. doi:https://doi.org/10.1016/j.pharmthera.2005.01.005
- Baskin, K. K., Makarewich, C. A., DeLeon, S. M., Ye, W., Chen, B., Beetz, N., . . . Olson, E. N. (2017). MED12 regulates a transcriptional network of calcium-handling genes in the heart. *JCI Insight*, 2(14). doi:10.1172/jci.insight.91920
- Baum, J., & Duffy, H. S. (2011). Fibroblasts and myofibroblasts: what are we talking about? *J Cardiovasc Pharmacol*, 57(4), 376-379. doi:10.1097/FJC.0b013e3182116e39
- Bergmann, O. (2019). Clearing up the mist: cardiomyocyte renewal in human hearts. *European Heart Journal*, 40(13), 1037-1038. doi:10.1093/eurheartj/ehz097

-
- Bergmann, O., Bhardwaj, R. D., Bernard, S., Zdunek, S., Barnabé-Heider, F., Walsh, S., . . . Frisé, J. (2009). Evidence for cardiomyocyte renewal in humans. *Science*, *324*(5923), 98-102. doi:10.1126/science.1164680
- Bergmann, O., & Jovinge, S. (2014). Cardiac regeneration in vivo: Mending the heart from within? *Stem Cell Research*, *13*(3, Part B), 523-531. doi:https://doi.org/10.1016/j.scr.2014.07.002
- Bergmann, O., Zdunek, S., Felker, A., Salehpour, M., Alkass, K., Bernard, S., . . . Frisé, J. (2015). Dynamics of Cell Generation and Turnover in the Human Heart. *Cell*, *161*(7), 1566-1575. doi:10.1016/j.cell.2015.05.026
- Berridge, B. R., Van Vleet, J. F., & Herman, E. (2013). Chapter 46 - Cardiac, Vascular, and Skeletal Muscle Systems. In W. M. Haschek, C. G. Rousseaux, & M. A. Wallig (Eds.), *Haschek and Rousseaux's Handbook of Toxicologic Pathology (Third Edition)* (pp. 1567-1665). Boston: Academic Press.
- Berry, M. F., Engler, A. J., Woo, Y. J., Pirolli, T. J., Bish, L. T., Jayasankar, V., . . . Sweeney, H. L. (2006). Mesenchymal stem cell injection after myocardial infarction improves myocardial compliance. *American Journal of Physiology-Heart and Circulatory Physiology*, *290*(6), H2196-H2203. doi:10.1152/ajpheart.01017.2005
- Bers, D. M. (2000). Calcium fluxes involved in control of cardiac myocyte contraction. *Circ Res*, *87*(4), 275-281. doi:10.1161/01.res.87.4.275
- Bers, D. M. (2002). Cardiac excitation-contraction coupling. *Nature*, *415*(6868), 198-205. doi:10.1038/415198a
- Bers, D. M. (2008). Calcium cycling and signaling in cardiac myocytes. *Annu Rev Physiol*, *70*, 23-49. doi:10.1146/annurev.physiol.70.113006.100455
- Bers, D. M., & Guo, T. (2005). Calcium signaling in cardiac ventricular myocytes. *Ann N Y Acad Sci*, *1047*, 86-98. doi:10.1196/annals.1341.008
- Boelens, H. F. M., Eilers, P. H. C., & Hankemeier, T. (2005). Sign Constraints Improve the Detection of Differences between Complex Spectral Data Sets: LC-IR As an Example. *Analytical Chemistry*, *77*(24), 7998-8007. doi:10.1021/ac051370e
- Böner, F., Borg, N., Burghoff, S., & Schrader, J. (2012). Resident cardiac immune cells and expression of the ectonucleotidase enzymes CD39 and CD73 after ischemic injury. *PLoS One*, *7*(4), e34730-e34730. doi:10.1371/journal.pone.0034730
- Buetow, B. S., & Laflamme, M. A. (2018). 10 - Cardiovascular. In P. M. Treuting, S. M. Dintzis, & K. S. Montine (Eds.), *Comparative Anatomy and Histology (Second Edition)* (pp. 163-189). San Diego: Academic Press.
- Camelliti, P., Borg, T. K., & Kohl, P. (2005). Structural and functional characterisation of cardiac fibroblasts. *Cardiovasc Res*, *65*(1), 40-51. doi:10.1016/j.cardiores.2004.08.020
- Carafoli, E. (2002). Calcium signaling: A tale for all seasons. *Proceedings of the National Academy of Sciences of the United States of America*, *99*(3), 1115-1122. doi:DOI 10.1073/pnas.032427999

- Cavallini, F., & Tarantola, M. (2019). ECIS based wounding and reorganization of cardiomyocytes and fibroblasts in co-cultures. *Prog Biophys Mol Biol*, *144*, 116-127. doi:10.1016/j.pbiomolbio.2018.06.010
- Cesa, C. M., Kirchgessner, N., Mayer, D., Schwarz, U. S., Hoffmann, B., & Merkel, R. (2007). Micropatterned silicone elastomer substrates for high resolution analysis of cellular force patterns. *Rev Sci Instrum*, *78*(3), 034301. doi:10.1063/1.2712870
- Chen, J. B., Tao, R., Sun, H. Y., Tse, H. F., Lau, C. P., & Li, G. R. (2010). Multiple Ca²⁺ signaling pathways regulate intracellular Ca²⁺ activity in human cardiac fibroblasts. *J Cell Physiol*, *223*(1), 68-75. doi:10.1002/jcp.22010
- Chen, W., & Frangogiannis, N. G. (2013). Fibroblasts in post-infarction inflammation and cardiac repair. *Biochim Biophys Acta*, *1833*(4), 945-953. doi:10.1016/j.bbamcr.2012.08.023
- Chiong, M., Wang, Z. V., Pedrozo, Z., Cao, D. J., Troncoso, R., Ibacache, M., . . . Lavandero, S. (2011). Cardiomyocyte death: mechanisms and translational implications. *Cell Death & Disease*, *2*(12), e244-e244. doi:10.1038/cddis.2011.130
- Clapham, D. E. (2003). TRP channels as cellular sensors. *Nature*, *426*(6966), 517-524. doi:10.1038/nature02196
- Colombelli, J., Grill, S. W., & Stelzer, E. H. K. (2004). Ultraviolet diffraction limited nanosurgery of live biological tissues. *Review of Scientific Instruments*, *75*(2), 472-478. doi:10.1063/1.1641163
- Davis, J. P., & Tikunova, S. B. (2008). Ca²⁺ exchange with troponin C and cardiac muscle dynamics. *Cardiovascular Research*, *77*(4), 619-626. doi:10.1093/cvr/cvm098
- de Tombe, P. P. (2003). Cardiac myofilaments: mechanics and regulation. *Journal of Biomechanics*, *36*(5), 721-730. doi:10.1016/s0021-9290(02)00450-5
- Dell'Aglio, M., Gaudioso, R., De Pascale, O., & De Giacomo, A. (2015). Mechanisms and processes of pulsed laser ablation in liquids during nanoparticle production. *Applied Surface Science*, *348*, 4-9. doi:https://doi.org/10.1016/j.apsusc.2015.01.082
- Desplantez, T. (2017). Cardiac Cx43, Cx40 and Cx45 co-assembling: involvement of connexins epitopes in formation of hemichannels and Gap junction channels. *BMC Cell Biol*, *18*(Suppl 1), 3. doi:10.1186/s12860-016-0118-4
- Dewenter, M., Lieth, A. v. d., Katus, H. A., & Backs, J. (2017). Calcium Signaling and Transcriptional Regulation in Cardiomyocytes. *Circulation Research*, *121*(8), 1000-1020. doi:doi:10.1161/CIRCRESAHA.117.310355
- Dhein, S. (2004). Pharmacology of gap junctions in the cardiovascular system. *Cardiovascular Research*, *62*(2), 287-298. doi:10.1016/j.cardiores.2004.01.019
- Dispersyn, G. D., Mesotten, L., Meuris, B., Maes, A., Mortelmans, L., Flameng, W., . . . Borgers, M. (2002). Dissociation of cardiomyocyte apoptosis and dedifferentiation in infarct border zones. *European Heart Journal*, *23*(11), 849-857. doi:10.1053/euhj.2001.2963

-
- Dostal, D. E., Feng, H., Nizamuddinov, D., Golden, H. B., Afroze, S. H., Dostal, J. D., . . . Gerilechaogetu, F. (2014). Mechanosensing and Regulation of Cardiac Function. *Journal of clinical & experimental cardiology*, 5(6), 314-314. doi:10.4172/2155-9880.1000314
- Du, J., Xie, J., Zhang, Z., Tsujikawa, H., Fusco, D., Silverman, D., . . . Yue, L. (2010). TRPM7-mediated Ca²⁺ signals confer fibrogenesis in human atrial fibrillation. *Circulation Research*, 106(5), 992-1003. doi:10.1161/CIRCRESAHA.109.206771
- Eilers, P. H., & Boelens, H. F. (2005). Baseline correction with asymmetric least squares smoothing. *Leiden University Medical Centre Report*, 1(1), 5.
- Eilers, P. H. C. (2003). A Perfect Smoother. *Analytical Chemistry*, 75(14), 3631-3636. doi:10.1021/ac034173t
- Eisner, D. A., Caldwell, J. L., Kistamas, K., & Trafford, A. W. (2017). Calcium and Excitation-Contraction Coupling in the Heart. *Circ Res*, 121(2), 181-195. doi:10.1161/CIRCRESAHA.117.310230
- Elmore, S. (2007). Apoptosis: a review of programmed cell death. *Toxicologic pathology*, 35(4), 495-516. doi:10.1080/01926230701320337
- England, J., & Loughna, S. (2013). Heavy and light roles: myosin in the morphogenesis of the heart. *Cellular and molecular life sciences : CMLS*, 70(7), 1221-1239. doi:10.1007/s00018-012-1131-1
- Fabio Da Silva. The role of R-spondin3 in coronary artery formation and novel roles for retinoic acid signaling in cardiac development and repair. Agricultural sciences. Université Côte d'Azur, 2017. English.
- Falcón, D., Galeano-Otero, I., Calderón-Sánchez, E., Del Toro, R., Martín-Bórnez, M., Rosado, J. A., . . . Smani, T. (2019). TRP Channels: Current Perspectives in the Adverse Cardiac Remodeling. *Front Physiol*, 10. doi:10.3389/fphys.2019.00159
- Fearnley, C. J., Roderick, H. L., & Bootman, M. D. (2011). Calcium signaling in cardiac myocytes. *Cold Spring Harb Perspect Biol*, 3(11), a004242. doi:10.1101/cshperspect.a004242
- Feng, J., Armillei, M. K., Yu, A. S., Liang, B. T., Runnels, L. W., & Yue, L. (2019). Ca²⁺ Signaling in Cardiac Fibroblasts and Fibrosis-Associated Heart Diseases. *Journal of cardiovascular development and disease*, 6(4), 34. doi:10.3390/jcdd6040034
- Foglia, M. J., & Poss, K. D. (2016). Building and re-building the heart by cardiomyocyte proliferation. *Development*, 143(5), 729-740. doi:10.1242/dev.132910
- Frangogiannis, N. G. (2012). Regulation of the inflammatory response in cardiac repair. *Circ Res*, 110(1), 159-173. doi:10.1161/circresaha.111.243162.
- Frangogiannis, N. G. (2014). The inflammatory response in myocardial injury, repair, and remodelling. *Nat Rev Cardiol*, 11(5), 255-265. doi:10.1038/nrcardio.2014.28
- Frangogiannis, N. G. (2015). Inflammation in cardiac injury, repair and regeneration. *Current opinion in cardiology*, 30(3), 240-245. doi:10.1097/HCO.0000000000000158

- Garcia-Dorado, D., & Ruiz-Meana, M. (2000). Propagation of Cell Death During Myocardial Reperfusion. *Physiology*, *15*(6), 326-330. doi:10.1152/physiologyonline.2000.15.6.326
- Gaudesius, G., Miragoli, M., Thomas, S. P., & Rohr, S. (2003). Coupling of cardiac electrical activity over extended distances by fibroblasts of cardiac origin. *Circ Res*, *93*(5), 421-428. doi:10.1161/01.RES.0000089258.40661.0C
- Gee, K. R., Brown, K. A., Chen, W. N. U., Bishop-Stewart, J., Gray, D., & Johnson, I. (2000). Chemical and physiological characterization of fluo-4 Ca²⁺-indicator dyes. *Cell Calcium*, *27*(2), 97-106. doi:https://doi.org/10.1054/ceca.1999.0095
- Geiger, B., Bershadsky, A., Pankov, R., & Yamada, K. M. (2001). Transmembrane crosstalk between the extracellular matrix and the cytoskeleton. *Nature Reviews Molecular Cell Biology*, *2*(11), 793-805. doi:10.1038/35099066
- Geiger, B., Spatz, J. P., & Bershadsky, A. D. (2009). Environmental sensing through focal adhesions. *Nature Reviews Molecular Cell Biology*, *10*(1), 21-33. doi:10.1038/nrm2593
- Gros, D. B., & Jongsma, H. J. (1996). Connexins in mammalian heart function. *Bioessays*, *18*(9), 719-730. doi:10.1002/bies.950180907
- Gross, P., Honnorat, N., Varol, E., Wallner, M., Trapanese, D. M., Sharp, T. E., . . . Houser, S. R. (2016). Nuquantus: Machine learning software for the characterization and quantification of cell nuclei in complex immunofluorescent tissue images. *Scientific Reports*, *6*(1), 23431. doi:10.1038/srep23431
- Gupta, K. B., Ratcliffe, M. B., Fallert, M. A., Edmunds, L. H., & Bogen, D. K. (1994). Changes in passive mechanical stiffness of myocardial tissue with aneurysm formation. *Circulation*, *89*(5), 2315-2326. doi:10.1161/01.CIR.89.5.2315
- Gutierrez, E., & Groisman, A. (2011). Measurements of Elastic Moduli of Silicone Gel Substrates with a Microfluidic Device. *PLoS One*, *6*(9), e25534. doi:10.1371/journal.pone.0025534
- Gutstein, D. E., Liu, F.-y., Meyers, M. B., Choo, A., & Fishman, G. I. (2003). The organization of adherens junctions and desmosomes at the cardiac intercalated disc is independent of gap junctions. *Journal of Cell Science*, *116*(5), 875-885. doi:10.1242/jcs.00258
- Harris, A. K., Wild, P., & Stopak, D. (1980). Silicone rubber substrata: a new wrinkle in the study of cell locomotion. *Science*, *208*(4440), 177. doi:10.1126/science.6987736
- Harris, I. S., & Black, B. L. (2010). Development of the endocardium. *Pediatric cardiology*, *31*(3), 391-399. doi:10.1007/s00246-010-9642-8
- Hersch, N., Wolters, B., Dreissen, G., Springer, R., Kirchgessner, N., Merkel, R., & Hoffmann, B. (2013). The constant beat: cardiomyocytes adapt their forces by equal contraction upon environmental stiffening. *Biol Open*, *2*(3), 351-361. doi:10.1242/bio.20133830
- Hersch, N., Wolters, B., Ungvari, Z., Gautam, T., Deshpande, D., Merkel, R., . . . Csiszar, A. (2016). Biotin-conjugated fusogenic liposomes for high-quality cell purification. *J Biomater Appl*, *30*(6), 846-856. doi:10.1177/0885328215603026

-
- Herum, K. M., Choppe, J., Kumar, A., Engler, A. J., & McCulloch, A. D. (2017). Mechanical regulation of cardiac fibroblast profibrotic phenotypes. *Molecular biology of the cell*, 28(14), 1871-1882. doi:10.1091/mbc.E17-01-0014
- Hobai Ion, A., & O'Rourke, B. (2000). Enhanced Ca²⁺-Activated Na⁺-Ca²⁺ Exchange Activity in Canine Pacing-Induced Heart Failure. *Circulation Research*, 87(8), 690-698. doi:10.1161/01.RES.87.8.690
- Houben, S., Kirchgeßner, N., & Merkel, R. (2010, 2010//). *Estimating Force Fields of Living Cells – Comparison of Several Regularization Schemes Combined with Automatic Parameter Choice*. Paper presented at the Pattern Recognition, Berlin, Heidelberg.
- Jacot, J. G., McCulloch, A. D., & Omens, J. H. (2008). Substrate Stiffness Affects the Functional Maturation of Neonatal Rat Ventricular Myocytes. *Biophysical journal*, 95(7), 3479-3487. doi:https://doi.org/10.1529/biophysj.107.124545
- Jeyaraman, M. M., Srisakuldee, W., Nickel, B. E., & Kardami, E. (2012). Connexin43 phosphorylation and cytoprotection in the heart. *Biochimica et Biophysica Acta (BBA) - Biomembranes*, 1818(8), 2009-2013. doi:https://doi.org/10.1016/j.bbamem.2011.06.023
- Johnson, R. D., & Camelliti, P. (2018). Role of Non-Myocyte Gap Junctions and Connexin Hemichannels in Cardiovascular Health and Disease: Novel Therapeutic Targets? *Int J Mol Sci*, 19(3). doi:10.3390/ijms19030866
- Ju, H., & Dixon, I. M. C. (1995). Cardiac Extracellular Matrix and its Role in the Development of Heart Failure. In P. K. Singal, I. M. C. Dixon, R. E. Beamish, & N. S. Dhalla (Eds.), *Mechanisms of Heart Failure* (pp. 75-90). Boston, MA: Springer US.
- Kakkar, R., & Lee, R. T. (2010). Intramyocardial fibroblast myocyte communication. *Circulation Research*, 106(1), 47-57. doi:10.1161/CIRCRESAHA.109.207456
- Kanitz, A., Kalus, M. R., Gurevich, E. L., Ostendorf, A., Barcikowski, S., & Amans, D. (2019). Review on experimental and theoretical investigations of the early stage, femtoseconds to microseconds processes during laser ablation in liquid-phase for the synthesis of colloidal nanoparticles. *Plasma Sources Science and Technology*, 28(10), 103001. doi:10.1088/1361-6595/ab3dbe
- Kanno, S., & Saffitz, J. E. (2001). The role of myocardial gap junctions in electrical conduction and arrhythmogenesis. *Cardiovascular Pathology*, 10(4), 169-177. doi:https://doi.org/10.1016/S1054-8807(01)00078-3
- Kohl, P., & Gourdie, R. G. (2014). Fibroblast-myocyte electrotonic coupling: does it occur in native cardiac tissue? *J Mol Cell Cardiol*, 70, 37-46. doi:10.1016/j.yjmcc.2013.12.024
- Kohl, P., & Noble, D. (1996). Mechanosensitive connective tissue: potential influence on heart rhythm. *Cardiovasc Res*, 32(1), 62-68.
- Konstantinidis, K., Whelan, R. S., & Kitsis, R. N. (2012). Mechanisms of cell death in heart disease. *Arterioscler Thromb Vasc Biol*, 32(7), 1552-1562. doi:10.1161/ATVBAHA.111.224915

- Kowalczyk, A. P., & Green, K. J. (2013). Structure, function, and regulation of desmosomes. *Progress in molecular biology and translational science*, 116, 95-118. doi:10.1016/B978-0-12-394311-8.00005-4
- Kubalová, Z. (2003). Inactivation of L-type calcium channels in cardiomyocytes. Experimental and theoretical approaches. *Gen Physiol Biophys*, 22(4), 441-454.
- Kumar, N. M., & Gilula, N. B. (1996). The gap junction communication channel. *Cell*, 84(3), 381-388. doi:10.1016/s0092-8674(00)81282-9
- Kwak, H. B. (2013). Aging, exercise, and extracellular matrix in the heart *Journal of exercise rehabilitation* (Vol. 9, pp. 338-347).
- Laver, D. R. (2018). Regulation of the RyR channel gating by Ca(2+) and Mg(2). *Biophysical reviews*, 10(4), 1087-1095. doi:10.1007/s12551-018-0433-4
- Lázár, E., Sadek, H. A., & Bergmann, O. (2017). Cardiomyocyte renewal in the human heart: insights from the fall-out. *European Heart Journal*, 38(30), 2333-2342. doi:10.1093/eurheartj/ehx343
- Lebeche, D., & Kang, S. (2013). Myocardial calcium signaling in physiology and disease. *Journal of Receptor, Ligand and Channel Research*. doi:10.2147/jrlcr.S36375
- Lehnart, S. E., Maier, L. S., & Hasenfuss, G. (2009). Abnormalities of calcium metabolism and myocardial contractility depression in the failing heart. *Heart failure reviews*, 14(4), 213-224. doi:10.1007/s10741-009-9146-x
- Leithe, E., Kjenseth, A., Bruun, J., Sirnes, S., & Rivedal, E. (2010). Inhibition of connexin 43 gap junction channels by the endocrine disruptor ioxynil. *Toxicol Appl Pharmacol*, 247(1), 10-17. doi:10.1016/j.taap.2010.05.006
- Li, C., Meng, Q., Yu, X., Jing, X., Xu, P., & Luo, D. (2012). Regulatory effect of connexin 43 on basal Ca²⁺ signaling in rat ventricular myocytes. *PLoS One*, 7(4), e36165. doi:10.1371/journal.pone.0036165
- Li, F., Wang, X., Capasso, J. M., & Gerdes, A. M. (1996). Rapid Transition of Cardiac Myocytes from Hyperplasia to Hypertrophy During Postnatal Development. *Journal of Molecular and Cellular Cardiology*, 28(8), 1737-1746. doi:https://doi.org/10.1006/jmcc.1996.0163
- Li, G.-R., Sun, H.-Y., Chen, J.-B., Zhou, Y., Tse, H.-F., & Lau, C.-P. (2009). Characterization of Multiple Ion Channels in Cultured Human Cardiac Fibroblasts. *PLoS One*, 4(10), e7307. doi:10.1371/journal.pone.0007307
- Litviňuková, M., Talavera-López, C., Maatz, H., Reichart, D., Worth, C. L., Lindberg, E. L., . . . Teichmann, S. A. (2020). Cells of the adult human heart. *Nature*. doi:10.1038/s41586-020-2797-4
- Louch, W. E., Sheehan, K. A., & Wolska, B. M. (2011). Methods in cardiomyocyte isolation, culture, and gene transfer. *J Mol Cell Cardiol*, 51(3), 288-298. doi:10.1016/j.yjmcc.2011.06.012
- Luo, M., & Anderson Mark, E. (2013). Mechanisms of Altered Ca²⁺ Handling in Heart Failure. *Circulation Research*, 113(6), 690-708. doi:10.1161/CIRCRESAHA.113.301651

-
- Ma, Y., de Castro Bras, L. E., Toba, H., Iyer, R. P., Hall, M. E., Winniford, M. D., . . . Lindsey, M. L. (2014). Myofibroblasts and the extracellular matrix network in post-myocardial infarction cardiac remodeling. *Pflugers Arch*, 466(6), 1113-1127. doi:10.1007/s00424-014-1463-9
- Manjarrez-Marmolejo, J., & Franco-Pérez, J. (2016). Gap Junction Blockers: An Overview of their Effects on Induced Seizures in Animal Models *Curr Neuropharmacol* (Vol. 14, pp. 759-771).
- Marcela, S. G., Cristina, R. M. M., Angel, P. G. M., Manuel, A. M., Sofía, D.-C., Patricia, D. L. R.-S., . . . Concepción, S. G. (2012). Chronological and Morphological Study of Heart Development in the Rat. *The Anatomical Record*, 295(8), 1267-1290. doi:10.1002/ar.22508
- Matsushita, T., Oyamada, M., Fujimoto, K., Yasuda, Y., Masuda, S., Wada, Y., . . . Takamatsu, T. (1999). Remodeling of Cell-Cell and Cell-Extracellular Matrix Interactions at the Border Zone of Rat Myocardial Infarcts. *Circulation Research*, 85(11), 1046-1055. doi:10.1161/01.RES.85.11.1046
- Merkel, R., Kirchgessner, N., Cesa, C. M., & Hoffmann, B. (2007). Cell force microscopy on elastic layers of finite thickness. *Biophysical journal*, 93(9), 3314-3323. doi:10.1529/biophysj.107.111328
- Miller, L. M., & Gal, A. (2017). Chapter 10 - Cardiovascular System and Lymphatic Vessels1. In J. F. Zachary (Ed.), *Pathologic Basis of Veterinary Disease (Sixth Edition)* (pp. 561-616.e561): Mosby.
- Miragoli, M., Gaudesius, G., & Rohr, S. (2006). Electrotonic modulation of cardiac impulse conduction by myofibroblasts. *Circ Res*, 98(6), 801-810. doi:10.1161/01.RES.0000214537.44195.a3
- Mohamed, T. M., Abou-Leisa, R., Stafford, N., Maqsood, A., Zi, M., Prehar, S., . . . Oceandy, D. (2016). The plasma membrane calcium ATPase 4 signalling in cardiac fibroblasts mediates cardiomyocyte hypertrophy. *Nat Commun*, 7, 11074. doi:10.1038/ncomms11074
- Moran, M. M., McAlexander, M. A., Bíró, T., & Szallasi, A. (2011). Transient receptor potential channels as therapeutic targets. *Nature Reviews Drug Discovery*, 10(8), 601-620. doi:10.1038/nrd3456
- Morsch, M., Radford, R. A., Don, E. K., Lee, A., Hortle, E., Cole, N. J., & Chung, R. S. (2017). Triggering Cell Stress and Death Using Conventional UV Laser Confocal Microscopy. *J Vis Exp*(120). doi:10.3791/54983
- Nakou, E. S., Parthenakis, F. I., Kallergis, E. M., Marketou, M. E., Nakos, K. S., & Vardas, P. E. (2016). Healthy aging and myocardium: A complicated process with various effects in cardiac structure and physiology. *Int J Cardiol*, 209, 167-175. doi:10.1016/j.ijcard.2016.02.039

- Narciso, C., Wu, Q., Brodskiy, P., Garston, G., Baker, R., Fletcher, A., & Zartman, J. (2015). Patterning of wound-induced intercellular Ca(2+) flashes in a developing epithelium. *Phys Biol*, *12*(5), 056005. doi:10.1088/1478-3975/12/5/056005
- Natarajan, A., Stancescu, M., Dhir, V., Armstrong, C., Sommerhage, F., Hickman, J. J., & Molnar, P. (2011). Patterned cardiomyocytes on microelectrode arrays as a functional, high information content drug screening platform. *Biomaterials*, *32*(18), 4267-4274. doi:10.1016/j.biomaterials.2010.12.022
- Nguyen, N. T., Han, W., Cao, W. M., Wang, Y., Wen, S., Huang, Y., . . . Zhou, Y. (2018). Store-Operated Calcium Entry Mediated by ORAI and STIM. *Compr Physiol*, *8*(3), 981-1002. doi:10.1002/cphy.c170031
- Nielsen, N., Lindemann, O., & Schwab, A. (2014). TRP channels and STIM/ORAI proteins: sensors and effectors of cancer and stroma cell migration. *British journal of pharmacology*, *171*(24), 5524-5540. doi:10.1111/bph.12721
- Nielsen, S. H., Mygind, N. D., Michelsen, M. M., Bechsgaard, D. F., Suhrs, H. E., Genovese, F., . . . Kastrup, J. (2018). Accelerated collagen turnover in women with angina pectoris without obstructive coronary artery disease: An iPOWER substudy. *European Journal of Preventive Cardiology*, *25*(7), 719-727. doi:10.1177/2047487318758750
- Nishida, K., Kyoji, S., Yamaguchi, O., Sadoshima, J., & Otsu, K. (2009). The role of autophagy in the heart. *Cell Death & Differentiation*, *16*(1), 31-38. doi:10.1038/cdd.2008.163
- Nishida, M., Carley, W. W., Gerritsen, M. E., Ellingsen, O., Kelly, R. A., & Smith, T. W. (1993). Isolation and characterization of human and rat cardiac microvascular endothelial cells. *American Journal of Physiology-Heart and Circulatory Physiology*, *264*(2), H639-H652. doi:10.1152/ajpheart.1993.264.2.H639
- O'Neal, W. T., Griffin, W. F., Kent, S. D., & Virag, J. A. (2013). Cellular Pathways of Death and Survival in Acute Myocardial Infarction. *Journal of Clinical and Experimental Cardiology*, *2013*, 1-9.
- Oddershede, L. B. (2012). Force probing of individual molecules inside the living cell is now a reality. *Nature Chemical Biology*, *8*(11), 879-886. doi:10.1038/nchembio.1082
- Pellegrin, S., & Mellor, H. (2007). Actin stress fibres. *Journal of Cell Science*, *120*(20), 3491. doi:10.1242/jcs.018473
- Pellman, J., Zhang, J., & Sheikh, F. (2016). Myocyte-fibroblast communication in cardiac fibrosis and arrhythmias: Mechanisms and model systems. *J Mol Cell Cardiol*, *94*, 22-31. doi:10.1016/j.yjmcc.2016.03.005
- Peracchia, C. (2004). Chemical gating of gap junction channels; roles of calcium, pH and calmodulin. *Biochim Biophys Acta*, *1662*(1-2), 61-80. doi:10.1016/j.bbamem.2003.10.020
- Pinto, A. R., Ilinykh, A., Ivey, M. J., Kuwabara, J. T., D'Antoni, M. L., Debuque, R., . . . Tallquist, M. D. (2016). Revisiting Cardiac Cellular Composition. *Circ Res*, *118*(3), 400-409. doi:10.1161/circresaha.115.307778

-
- Piquereau, J., Caffin, F., Novotova, M., Lemaire, C., Veksler, V., Garnier, A., . . . Joubert, F. (2013). Mitochondrial dynamics in the adult cardiomyocytes: which roles for a highly specialized cell? *Frontiers in physiology*, *4*, 102-102. doi:10.3389/fphys.2013.00102
- Plotnikov, S. V., Sabass, B., Schwarz, U. S., & Waterman, C. M. (2014). High-resolution traction force microscopy. *Methods Cell Biol*, *123*, 367-394. doi:10.1016/B978-0-12-420138-5.00020-3
- Polontchouk, L. O., Valiunas, V., Haefliger, J.-A., Eppenberger, H. M., & Weingart, R. (2002). Expression and regulation of connexins in cultured ventricular myocytes isolated from adult rat hearts. *Pflügers Archiv*, *443*(5), 676-689. doi:10.1007/s00424-001-0747-z
- Putney, J. W., & Tomita, T. (2012). Phospholipase C signaling and calcium influx. *Advances in biological regulation*, *52*(1), 152-164. doi:10.1016/j.advenzreg.2011.09.005
- Quinn, T. A., Camelliti, P., Rog-Zielinska, E. A., Siedlecka, U., Poggioli, T., Toole, E. T., . . . Kohl, P. (2016). Electrotonic coupling of excitable and nonexcitable cells in the heart revealed by optogenetics. *Proceedings of the National Academy of Sciences*, *113*(51), 14852. doi:10.1073/pnas.1611184114
- Rienks, M., Papageorgiou, A. P., Frangogiannis, N. G., & Heymans, S. (2014). Myocardial extracellular matrix: an ever-changing and diverse entity. *Circ Res*, *114*(5), 872-888. doi:10.1161/CIRCRESAHA.114.302533
- Roh, J. S., & Sohn, D. H. (2018). Damage-Associated Molecular Patterns in Inflammatory Diseases. *Immune network*, *18*(4), e27-e27. doi:10.4110/in.2018.18.e27
- Rohr, S. (2004). Role of gap junctions in the propagation of the cardiac action potential. *Cardiovascular Research*, *62*(2), 309-322. doi:10.1016/j.cardiores.2003.11.035
- Rother, J., Richter, C., Turco, L., Knoch, F., Mey, I., Luther, S., . . . Tarantola, M. (2015). Crosstalk of cardiomyocytes and fibroblasts in co-cultures. *Open Biol*, *5*(6), 150038. doi:10.1098/rsob.150038
- Samarel, A. M. (2005). Costameres, focal adhesions, and cardiomyocyte mechanotransduction. *American Journal of Physiology-Heart and Circulatory Physiology*, *289*(6), H2291-H2301. doi:10.1152/ajpheart.00749.2005
- Santulli, G., Xie, W., Reiken, S. R., & Marks, A. R. (2015). Mitochondrial calcium overload is a key determinant in heart failure. *Proc Natl Acad Sci U S A*, *112*(36), 11389-11394. doi:10.1073/pnas.1513047112
- Sarantitis, I., Papanastasopoulos, P., Manousi, M., Baikoussis, N. G., & Apostolakis, E. (2012). The cytoskeleton of the cardiac muscle cell. *Hellenic J Cardiol*, *53*(5), 367-379.
- Schindelin, J., Arganda-Carreras, I., Frise, E., Kaynig, V., Longair, M., Pietzsch, T., . . . Cardona, A. (2012). Fiji: an open-source platform for biological-image analysis. *Nature Methods*, *9*(7), 676-682. doi:10.1038/nmeth.2019
- Schirone, L., Forte, M., Palmerio, S., Yee, D., Nocella, C., Angelini, F., . . . Frati, G. (2017). A Review of the Molecular Mechanisms Underlying the Development and Progression of Cardiac Remodeling. *Oxid Med Cell Longev*, *2017*. doi:10.1155/2017/3920195

- Schlipp, A., Schinner, C., Spindler, V., Vielmuth, F., Gehmlich, K., Syrris, P., . . . Waschke, J. (2014). Desmoglein-2 interaction is crucial for cardiomyocyte cohesion and function. *Cardiovasc Res*, *104*(2), 245-257. doi:10.1093/cvr/cvu206
- Segretain, D., & Falk, M. M. (2004). Regulation of connexin biosynthesis, assembly, gap junction formation, and removal. *Biochim Biophys Acta*, *1662*(1-2), 3-21. doi:10.1016/j.bbamem.2004.01.007
- Sequeira, V., Nijenkamp, L. L., Regan, J. A., & van der Velden, J. (2014). The physiological role of cardiac cytoskeleton and its alterations in heart failure. *Biochim Biophys Acta*, *1838*(2), 700-722. doi:10.1016/j.bbamem.2013.07.011
- Severs, N. J. (2000). The cardiac muscle cell. *Bioessays*, *22*(2), 188-199. doi:10.1002/(sici)1521-1878(200002)22:2<188::Aid-bies10>3.0.Co;2-t
- Severs, N. J., Bruce, A. F., Dupont, E., & Rothery, S. (2008). Remodelling of gap junctions and connexin expression in diseased myocardium. *Cardiovasc Res*, *80*(1), 9-19. doi:10.1093/cvr/cvn133
- Shah, S., Gnanasegaran, G., Sundberg-Cohon, J., & Buscombe, J. R. (2009). The Heart: Anatomy, Physiology and Exercise Physiology. In A. Movahed, G. Gnanasegaran, J. Buscombe, & M. Hall (Eds.), *Integrating Cardiology for Nuclear Medicine Physicians: A Guide to Nuclear Medicine Physicians* (pp. 3-22). Berlin, Heidelberg: Springer Berlin Heidelberg.
- Shaheen, M., Cheema, Y., Shahbaz, A. U., Bhattacharya, S. K., & Weber, K. T. (2011). Intracellular calcium overloading and oxidative stress in cardiomyocyte necrosis via a mitochondriocentric signal-transducer-effector pathway. *Experimental and clinical cardiology*, *16*(4), 109-115.
- Sham, J. S., Song, L. S., Chen, Y., Deng, L. H., Stern, M. D., Lakatta, E. G., & Cheng, H. (1998). Termination of Ca²⁺ release by a local inactivation of ryanodine receptors in cardiac myocytes. *Proc Natl Acad Sci U S A*, *95*(25), 15096-15101. doi:10.1073/pnas.95.25.15096
- Sheikh, F., Ross, R. S., & Chen, J. (2009). Cell-Cell Connection to Cardiac Disease. *Trends Cardiovasc Med*, *19*(6), 182-190. doi:10.1016/j.tcm.2009.12.001
- Sheydina, A., Riordon, D. R., & Boheler, K. R. (2011). Molecular mechanisms of cardiomyocyte aging. *Clinical science (London, England : 1979)*, *121*(8), 315-329. doi:10.1042/CS20110115
- Smith, G. L., & Eisner, D. A. (2019). Calcium Buffering in the Heart in Health and Disease. *Circulation*, *139*(20), 2358-2371. doi:10.1161/CIRCULATIONAHA.118.039329
- Smutny, M., Behrndt, M., Campinho, P., Ruprecht, V., & Heisenberg, C. P. (2015). UV laser ablation to measure cell and tissue-generated forces in the zebrafish embryo in vivo and ex vivo. *Methods Mol Biol*, *1189*, 219-235. doi:10.1007/978-1-4939-1164-6_15
- Soloperto, A., Palazzolo, G., Tsushima, H., Chierigatti, E., Vassalli, M., & Difato, F. (2016). Laser Nano-Neurosurgery from Gentle Manipulation to Nano-Incision of Neuronal

-
- Cells and Scaffolds: An Advanced Neurotechnology Tool. *Frontiers in Neuroscience*, 10(101). doi:10.3389/fnins.2016.00101
- Soonpaa, M. H., Kim, K. K., Pajak, L., Franklin, M., & Field, L. J. (1996). Cardiomyocyte DNA synthesis and binucleation during murine development. *Am J Physiol*, 271(5 Pt 2), H2183-2189. doi:10.1152/ajpheart.1996.271.5.H2183
- Souders, C. A., Bowers, S. L., & Baudino, T. A. (2009). Cardiac fibroblast: the renaissance cell. *Circ Res*, 105(12), 1164-1176. doi:10.1161/CIRCRESAHA.109.209809
- Sridhar, K. C., Hersch, N., Dreissen, G., Merkel, R., & Hoffmann, B. (2020). Calcium mediated functional interplay between myocardial cells upon laser-induced single-cell injury: an in vitro study of cardiac cell death signaling mechanisms. *Cell communication and signaling : CCS*, 18(1), 191. <https://doi.org/10.1186/s12964-020-00689-5>
- Surprenant, A., & North, R. A. (2009). Signaling at Purinergic P2X Receptors. *Annual Review of Physiology*, 71(1), 333-359. doi:10.1146/annurev.physiol.70.113006.100630
- Talman, V., & Kivelä, R. (2018). Cardiomyocyte-Endothelial Cell Interactions in Cardiac Remodeling and Regeneration. *Frontiers in cardiovascular medicine*, 5, 101-101. doi:10.3389/fcvm.2018.00101
- Thompson, S. A., Blazeski, A., Copeland, C. R., Cohen, D. M., Chen, C. S., Reich, D. M., & Tung, L. (2014). Acute slowing of cardiac conduction in response to myofibroblast coupling to cardiomyocytes through N-cadherin. *Journal of Molecular and Cellular Cardiology*, 68, 29-37. doi:10.1016/j.yjmcc.2013.12.025
- Thygesen, K., Alpert, J. S., Jaffe, A. S., Chaitman, B. R., Bax, J. J., Morrow, D. A., . . . Group, E. S. C. S. D. (2019). Fourth universal definition of myocardial infarction (2018). *Eur Heart J*, 40(3), 237-269. doi:10.1093/eurheartj/ehy462
- Tomko, J., Naddeo, J. J., Jimenez, R., Tan, Y., Steiner, M., Fitz-Gerald, J. M., . . . O'Malley, S. M. (2015). Size and polydispersity trends found in gold nanoparticles synthesized by laser ablation in liquids. *Physical Chemistry Chemical Physics*, 17(25), 16327-16333. doi:10.1039/C5CP01965F
- Tracy, R. E., & Sander, G. E. (2011). Histologically Measured Cardiomyocyte Hypertrophy Correlates with Body Height as Strongly as with Body Mass Index. *Cardiology Research and Practice*, 2011, 658958. doi:10.4061/2011/658958
- Tsuji, T., Tsuboi, Y., Kitamura, N., & Tsuji, M. (2004). Microsecond-resolved imaging of laser ablation at solid-liquid interface: investigation of formation process of nano-size metal colloids. *Applied Surface Science*, 229(1), 365-371. doi:<https://doi.org/10.1016/j.apsusc.2004.02.013>
- Valen, G. (2003). Cellular signalling mechanisms in adaptation to ischemia-induced myocardial damage. *Annals of Medicine*, 35(5), 300-307. doi:10.1080/07853890310001348
- van Dijk, S. J., Hamdani, N., Stienen, G. J. M., & van der Velden, J. (2008). Myocardial adaptations in the failing heart: cause or consequence? *Journal of Muscle Research and Cell Motility*, 29(6), 159-162. doi:10.1007/s10974-009-9169-x

- Vasquez, C., Benamer, N., & Morley, G. E. (2011). The Cardiac Fibroblast: Functional and Electrophysiological Considerations in Healthy and Diseased Hearts. *J Cardiovasc Pharmacol*, 57(4), 380-388. doi:10.1097/FJC.0b013e31820cda19
- Vassalle, M., & Lin, C. I. (2004). Calcium overload and cardiac function. *J Biomed Sci*, 11(5), 542-565. doi:10.1159/000079666
- Venkatachalam, K., & Montell, C. (2007). TRP Channels. *Annu Rev Biochem*, 76, 387-417. doi:10.1146/annurev.biochem.75.103004.142819
- Verheijen, M., Lienhard, M., Schrooders, Y., Clayton, O., Nudischer, R., Boerno, S., . . . Caiment, F. (2019). DMSO induces drastic changes in human cellular processes and epigenetic landscape in vitro. *Scientific Reports*, 9(1), 4641. doi:10.1038/s41598-019-40660-0
- Vermij, S. H., Abriel, H., & van Veen, T. A. B. (2017). Refining the molecular organization of the cardiac intercalated disc. *Cardiovascular Research*, 113(3), 259-275. doi:10.1093/cvr/cvw259
- Vogel, A., Noack, J., Hüttman, G., & Paltauf, G. (2005). Mechanisms of femtosecond laser nanosurgery of cells and tissues. *Applied Physics B*, 81(8), 1015-1047. doi:10.1007/s00340-005-2036-6
- Vogel, A., & Venugopalan, V. (2003). Mechanisms of Pulsed Laser Ablation of Biological Tissues. *Chemical Reviews*, 103(2), 577-644. doi:10.1021/cr010379n
- Walsh, K. B., & Zhang, J. (2008). Neonatal rat cardiac fibroblasts express three types of voltage-gated K⁺ channels: regulation of a transient outward current by protein kinase C. *Am J Physiol Heart Circ Physiol*, 294(2), H1010-1017. doi:10.1152/ajpheart.01195.2007
- Wang, J. H. C., & Lin, J.-S. (2007). Cell traction force and measurement methods. *Biomechanics and Modeling in Mechanobiology*, 6(6), 361. doi:10.1007/s10237-006-0068-4
- Wang, R., Wang, M., He, S., Sun, G., & Sun, X. (2020). Targeting Calcium Homeostasis in Myocardial Ischemia/Reperfusion Injury: An Overview of Regulatory Mechanisms and Therapeutic Reagents. *Frontiers in Pharmacology*, 11(872). doi:10.3389/fphar.2020.00872
- Weber, K. T., Sun, Y., Bhattacharya, S. K., Ahokas, R. A., & Gerling, I. C. (2013). Myofibroblast-mediated mechanisms of pathological remodelling of the heart. *Nat Rev Cardiol*, 10(1), 15-26. doi:10.1038/nrcardio.2012.158
- Wei, S., Cassara, C., Lin, X., & Veenstra, R. D. (2019). Calcium–calmodulin gating of a pH-insensitive isoform of connexin43 gap junctions. *Biochemical Journal*, 476(7), 1137-1148. doi:10.1042/BCJ20180912
- Weinhaus, A. J., & Roberts, K. P. (2005). Anatomy of the Human Heart. In P. A. Iaizzo (Ed.), *Handbook of Cardiac Anatomy, Physiology, and Devices* (pp. 51-79). Totowa, NJ: Humana Press.

-
- Weis Sara, M., Emery Jeffrey, L., Becker, K. D., McBride Daniel, J., Omens Jeffrey, H., & McCulloch Andrew, D. (2000). Myocardial Mechanics and Collagen Structure in the Osteogenesis Imperfecta Murine (oim). *Circulation Research*, 87(8), 663-669. doi:10.1161/01.RES.87.8.663
- Whelan, R. S., Kaplinskiy, V., & Kitsis, R. N. (2010). Cell death in the pathogenesis of heart disease: mechanisms and significance. *Annu Rev Physiol*, 72, 19-44. doi:10.1146/annurev.physiol.010908.163111
- Williams, G. S. B., Boyman, L., & Lederer, W. J. (2015). Mitochondrial calcium and the regulation of metabolism in the heart. *Journal of Molecular and Cellular Cardiology*, 78, 35-45. doi:10.1016/j.yjmcc.2014.10.019
- Wu, J.-I., & Wang, L.-H. (2019). Emerging roles of gap junction proteins connexins in cancer metastasis, chemoresistance and clinical application. *Journal of Biomedical Science*, 26(1), 8. doi:10.1186/s12929-019-0497-x
- Wu, J., Dickinson, R. B., & Lele, T. P. (2012). Investigation of in vivo microtubule and stress fiber mechanics with laser ablation. *Integr Biol (Camb)*, 4(5), 471-479. doi:10.1039/c2ib20015e
- Yang, H., Borg, T. K., Wang, Z., Ma, Z., & Gao, B. Z. (2014). Role of the basement membrane in regulation of cardiac electrical properties. *Annals of biomedical engineering*, 42(6), 1148-1157. doi:10.1007/s10439-014-0992-x
- Yue, L., Xie, J., & Nattel, S. (2011). Molecular determinants of cardiac fibroblast electrical function and therapeutic implications for atrial fibrillation *Cardiovasc Res* (Vol. 89, pp. 744-753).
- Zheng, J. (2013). Molecular mechanism of TRP channels. *Comprehensive Physiology*, 3(1), 221-242. doi:10.1002/cphy.c120001
- Zhou, P., & Pu, W. T. (2016). Recounting Cardiac Cellular Composition. *Circulation Research*, 118(3), 368-370. doi:10.1161/CIRCRESAHA.116.308139
- Zimmer, T., Haufe, V., & Blechschmidt, S. (2014). Voltage-gated sodium channels in the mammalian heart. *Global cardiology science & practice*, 2014(4), 449-463. doi:10.5339/gcsp.2014.58

Acknowledgements

I would like to express my sincere gratitude to everyone who had supported me during my doctoral research work.

Firstly, I would like to thank my Doktorvater, Prof. Dr. Rudolf Merkel for providing the opportunity to work in this research project at the IBI-2 research group. His guidance, feedback and insights have helped me a lot during the progress of this research work. His scientific inputs and questions were very important and provided direction to the research.

I would like to thank the other members of my PhD committee, Prof. Dr. Ulrich Kubitscheck (Institut für Physikalische und Theoretische Chemie), Prof. Dr. Arne Lützen (Institut für Organische Chemie und Biochemie) and Prof. Dr. Jörg Hoehfeld (Institut für Zellbiologie) for their valuable time to evaluate this thesis work.

I would like to thank PD Dr. Bernd Hoffmann at IBI-2: Mechanobiology at Forschungszentrum Jülich for his support and encouragement throughout this research work. He has provided his valuable suggestions and guidance at the time of difficulty during my research.

I thank Georg Dreissen and Dr. Ronald Springer for providing programs for data evaluation and for their useful discussions. Analysis of complex data was challenging during the research and I pay my sincere gratitude to them for their support.

I thank Nils Hersch for his inputs and support troubleshooting problems with cell culture. I also thank Nico Hampe for helping with setting up of laser ablation experiments in the initial stages.

I thank my friend and colleague Dr. Jella Abraham, who had been very helpful during the years of research. I also thank Dr. Dave Ahrens, Tabea Wiedenhof, Laura Schmit, Maithreyan Kuppusamy for their help and useful discussions during the thesis work.

I thank all my colleagues at IBI-2 for providing with a lot of useful ideas and helping me at various points during my working time at Forschungszentrum Jülich.

Finally, I would like to thank my dear Vaideki Thayumanvan for her encouragement and support during the years of research. I thank my friend Madhan kumar for his encouragement during these years. I thank my mother, father and my dear brother, Giridhar for their faith in me and continuous support all these years. I dedicate this work to them.

Publications

Parts of the dissertation have been published in:

- Sridhar, K. C., Hersch, N., Dreissen, G., Merkel, R., & Hoffmann, B. (2020). Calcium mediated functional interplay between myocardial cells upon laser-induced single-cell injury: an in vitro study of cardiac cell death signaling mechanisms. *Cell communication and signaling : CCS*, 18(1), 191. <https://doi.org/10.1186/s12964-020-00689-5>.

Other publications:

- Kleusch, C., Monzel, C., Sridhar, K. C., Hoffmann, B., Csiszár, A., & Merkel, R. (2020). Fluorescence Correlation Spectroscopy Reveals Interaction of Some Microdomain-Associated Lipids with Cellular Focal Adhesion Sites. *International journal of molecular sciences*, 21(21), 8149. <https://doi.org/10.3390/ijms21218149>.